253200-7-F

Unconventional Imaging Field Experiment Plan

Final Report
DECEMBER 1994

J.R. Fienup, J.N. Cederquist, J.C. Marron, and R.G. Paxman

Electro-Optics Laboratory
Environmental Research Institute of Michigan
P.O. Box 134001
Ann Arbor, MI 48113-4001

Prepared for:

Office of Naval Research
800 North Quincy Street
Arlington, Virginia 22217-5000
Attn.: Dr. William Stachnik

Contract No. N00014-93-C-0093

Approved for public release;
distribution unlimited

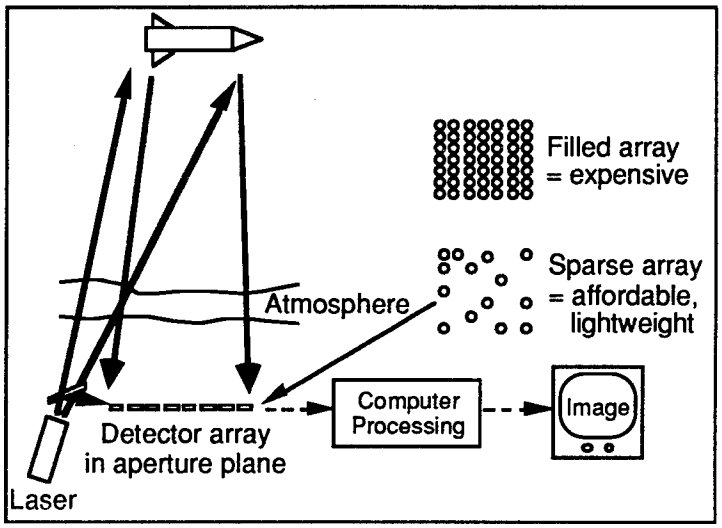

ERIM
P.O. Box 134001
Ann Arbor, MI 48113-4001

ERIM-320

REPORT DOCUMENTATION PAGE

Form Approved
OMB No. 0704-0188

1. AGENCY USE ONLY (*Leave Blank*)	2. REPORT DATE	3. REPORT TYPE AND DATES COVERED
	December 1994	Final Report 6/93 to 5/94

4. TITLE AND SUBTITLE
Unconventional Imaging Field Experiment Plan

5. FUNDING NUMBERS

6. AUTHOR(S)
J.R. Fienup, J.N. Cederquist, J.C. Marron and R.G. Paxman

7. PERFORMING ORGANIZATION NAME(S) AND ADDRESS(ES)
Electro-Optics Laboratory
Environmental Research Institute of Michigan
PO Box 134001
Ann Arbor, Michigan 48113-4001

8. PERFORMING ORGANIZATION REPORT NUMBER
253200-7-F
N00014-93-C-0093

9. SPONSORING/MONITORING AGENCY NAME(S) AND ADDRESS(ES)
Office of Naval Research
800 N. Quincy Street
Arlington, Virginia 22217-5000

10. SPONSORING/MONITORING AGENCY REPORT NUMBER

11. SUPPLEMENTARY NOTES

12a. DISTRIBUTION/AVAILABILITY STATEMENT
Approved for public release; distribution unlimited.

12b. DISTRIBUTION CODE

13. ABSTRACT (*Maximum 200 words*)

We investigated the feasibility of conducting experiments at the Innovative Science and Technology Experimental Facility (ISTEF). The experiments are to test unconventional imaging concepts that use laser illumination and pupil-plane detection. We show the trade-off between the sparsity of the number of sub-apertures and the number of speckle realizations collected. We invented and demonstrated two new algorithms for phasing heterodyne arrays that work for sparse arrays of detectors. We performed analysis showing that near-ground turbulence makes the isoplanatic patch size for a 10 km horizontal path impractically small, but for a 1 km path it can be accommodated by using a small target. We invented a new imaging modality involving collection of intensity data at multiple wavelengths from which we can reconstruct a 3-D image using an opacity constraint. We invented a new sparse-array pattern design in the shape of an arrow that fills a square OTF with a smaller number of sub-aperture than computer-optimized patterns. We showed that we can trade off background suppression for the ability to measure multiple speckles over a sub-aperture by placing the detector array in a plane beyond the focal plane.

14. SUBJECT TERMS	15. NUMBER OF PAGES
Laser unconventional imaging, atmospheric turbulence, sparse arrays, heterodyne detection, phase-error correction, phase retrieval	144
	16. PRICE CODE

17. SECURITY CLASSIFICATION OF REPORT	18. SECURITY CLASSIFICATION OF THIS PAGE	19. SECURITY CLASSIFICATION OF ABSTRACT	20. LIMITATION OF ABSTRACT
Unclassified	Unclassified	Unclassified	Same as report

(blank page)

PREFACE

The work reported here was performed in the Optical and IR Science Laboratory of the Advanced Concepts Division (which is now the Electro-Optics Laboratory), the Environmental Research Institute of Michigan (ERIM). The work was sponsored by the Office of Naval Research (ONR), Boston, Contract No. N00014-93-C-0093, funded from the Innovative Science and Technology Office of the Strategic Defense Initiative Office (SDIO/IST). The project monitors at ONR were Dr. Robert Mongeon, Mr. William Miceli, and Dr. William Stachnik.

This final report covers work performed from June 1993 to July 1994. The principal investigator was Dr. James R. Fienup. Additional contributors to this work also included Dr. Jack N. Cederquist, Ms. Ann M. Kowalczyk, Dr. Joseph C. Marron, Dr. Richard G. Paxman, Mr. Kirk S. Schroeder, and Ms. Joy E. VanBuhler.

(blank page)

TABLE OF CONTENTS

LIST OF FIGURES

LIST OF TABLES

1 INTRODUCTION AND OVERVIEW

This report describes an effort to examine a variety of unconventional imaging experiments that could be carried out at the Innovative Science and Technology Experimental Facility (ISTEF) at Cape Canaveral, FL. These unconventional imaging modalities all share the following attributes: they are based on illuminating a target by a laser and detecting the reflected light in a non-imaged (pupil or aperture) plane, as illustrated in Figure 1-1. This allows for a very light-weight, rapidly steerable, inexpensive receiver capable of very fine resolution. Such imaging approaches could have a large impact for such applications as theater missile defense, interceptor updates, surveillance, and medical imaging. The imaging approaches we studied include heterodyne array imaging, quasi-heterodyne imaging, laser correlography, and a new imaging modality: 3-D imaging by phase retrieval using an opacity constraint.

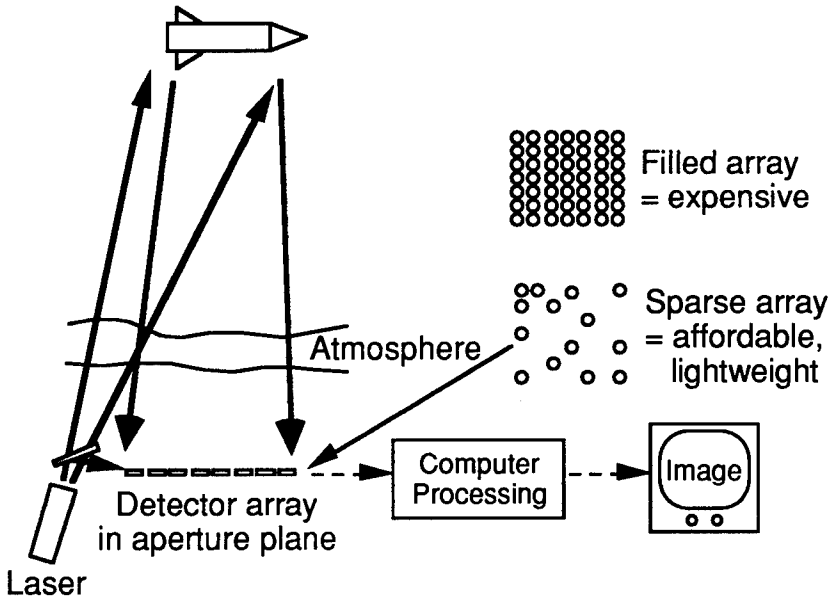

Figure 1-1. Unconventional Aperture-Plane Imaging with Lasers.

Under this effort we accomplished the following.

We planned sparse-array unconventional imaging experiments for ISTEF. We outlined experimental considerations for experiments to demonstrate imaging with sparse arrays of heterodyne receivers. Our plans are described in Section 2.

Through computer simulations we demonstrated the trade-off between the number of sparse-array subapertures and the number of speckle realizations for heterodyne array imaging and imaging correlography. We showed that when imaging a low-contrast, extended target with sparse arrays, many dozens or hundreds of speckle realizations are required for good-quality imagery, whereas for a target consisting of only a few bright points, only a few speckle realizations are required. This is described in Section 3.

We developed two new algorithms for phasing sparse arrays of heterodyne receivers, which no previous algorithms could do without additional information. These algorithms would correct for phase errors due to both heterodyne-receiver local-oscillator path-length errors and atmospheric turbulence. One of the algorithms is based on the iterative transform algorithm using a support constraint, and the other is an image sharpening algorithm. Section 4 gives derivations of the algorithms and shows successful phase-error correction results on computer-simulated data.

We performed analysis of near-ground atmospheric turbulence and derived limits of field-of-view and detector sizes for the 1 km and 10 km ranges at ISTEF. We found the most limiting factor to be anisoplanatism. This is described in Section 5.

We analyzed a multiple-wavelength data-collection system for use with 3-D phase retrieval with an opacity constraint. We performed computer simulations of 3-D (angle-angle-wavelength) laser intensity data, developed a phase retrieval algorithm using an opacity constraint, and demonstrated image reconstruction from the simulated data. This represents the first demonstration of this novel 3-D imaging concept. This is described in Section 6.

We set up a laboratory experiment and gathered quasi-heterodyne data with multiple speckle realizations and successfully processed the data into an image. This is described in Section 7.

We invented a new, efficient, deterministic sparse-array design, called the "arrow," which fills optical transfer function (OTF) space with a very small number of subapertures and is scalable to any arbitrary array size. It and a companion that gives double redundancy in OTF space are described in Section 8.

We analyzed a novel sensing method for gathering data with a CCD array that is in an intermediate plane that is in neither a focal plane nor in a plane conjugate to the pupil plane. This allows us to perform pupil-plane detection while simultaneously obtaining some background suppression by limiting the field-of-view, and optimally trading off these two aspects.

To make this report more self-contained and to avoid the need for extensive review material within the main body of the report, we have included, as Appendix A, a description the theory behind most of the imaging modalities analyzed in this report. It is from J.R. Fienup, "Unconventional Imaging Systems: Image Formation from Non-imaged Laser Speckle Patterns," in Emerging Systems and Technologies, S.R. Robinson, Ed., Vol. 8 of The Infrared & Electro-optical Systems Handbook, (ERIM, Ann Arbor, 1993), Chapter 1.5, pp.92-109. A reader unfamiliar with pupil-plane laser imaging modalities would benefit from reading Appendix A first.

References are at the end of each section.

Portions of this effort are described in the following presentations and publications. We have included as Appendices B, C, and D the first three, which have appeared as proceedings papers.

J.R. Fienup, A.M. Kowalczyk and J.E. Van Buhler, "Phasing Sparse Arrays of Heterodyne Receivers," presented in Orlando, Fla., and published in Proc. SPIE 2241-15, Inverse Optics III (April 1994), pp. 127-131.

R.G. Paxman, J.H. Seldin, J.R. Fienup, and J.C. Marron, "Use of an Opacity Constraint in Three-Dimensional Imaging," presented in Orlando, FL, and published in Proc. SPIE 2241-14, Inverse Optics III (April 1994), pp. 116-126.

J.C. Marron and R.G. Paxman, "Pulsed Heterodyne-Array Imaging," presented in Orlando, FL, and published in Proc. SPIE 2241-13, Inverse Optics III (April 1994), pp. 111-115.

J.R. Fienup, "Phasing Distributed Arrays of Heterodyne Receivers," presented to the Annual Meeting of the Optical Society of America, Dallas, TX, October 1994.

J.C. Marron, J.R. Fienup, and R.G. Paxman, "Unconventional 3-D Laser Imaging," submitted for presentation to Lasers '94, Quebec, Canada, December 1994.

2 PLAN FOR FIELD EXPERIMENTS

We envision a set of four major experimental thrusts to be performed at ISTEF: (1) direct-detection imaging, (2) short-range distributed heterodyne array imaging, (3) 3-D imaging, and (4) long-range imaging. Each major experiment would build on the infrastructure and knowledge resulting from the previous experiments. The relationships among these experiments are illustrated in Figure 2-1. They are described briefly in the Section 2.1 and in more detail in Section 2.3.

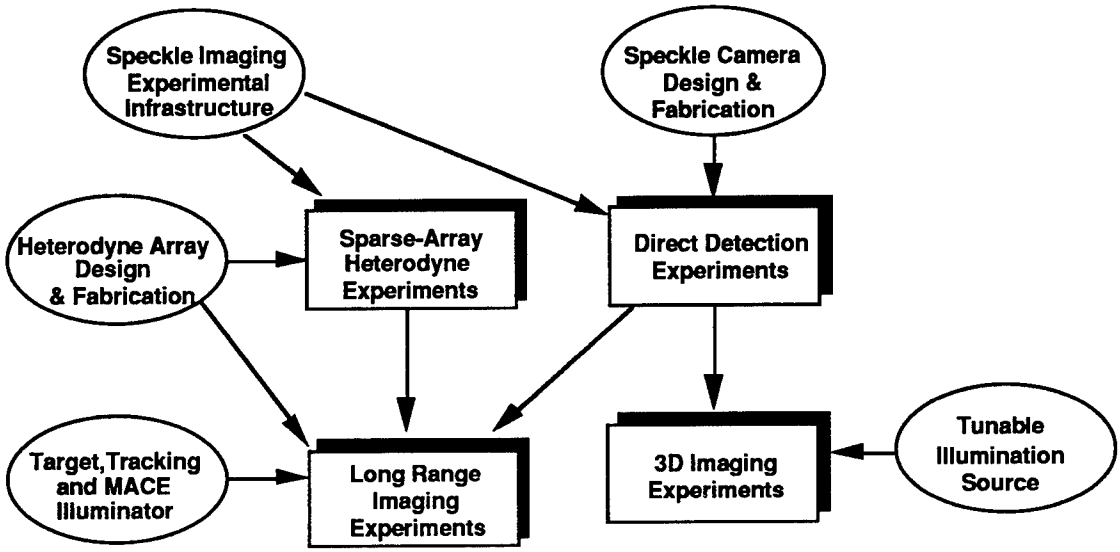

Figure 2-1. Illustration of the Relations Among the Major Sets of Experiments (boxes). The ovals show how infrastructure capabilities will be introduced to enable each new set of experiments in the experimental sequence.

2.1 FOUR PLANNED EXPERIMENTS

In our first major set of experiments, we would reconstruct high-quality images from speckle data collected at the 1 km range at ISTEF. These speckle data would be collected using a speckle camera – a high-quality detector array in the reimaged pupil plane of a telescope. This initial sensor, which would be constructed and demonstrated in Years 1 and 2 of the effort, would allow us to demonstrate image formation by modalities such as imaging correlography and coherent-imaging by phase retrieval. A

further goal of these experiments is to determine our ability to measure key target parameters such as size, rotation rate, and rotation axis, and to answer a variety of other science questions. The activities with the speckle camera would go on throughout the three years of the program.

The second major set of experiments would involve the demonstration of imaging with a distributed array of heterodyne receivers. These experiments would be performed in Years 1 and 2. The eight heterodyne receiver elements built by CREOL would be arranged in a sparse (quasi-non-redundant) 1-D array. Imaging experiments would be performed using target rotation to synthesize the second dimension of the receiver aperture. Experiments would also be conducted with the array elements in a non-redundant 2-D array. We would conduct these experiments at the 1 km and 3 km ranges at ISTEF in cooperation with other contractors. To obtain meaningful imagery in Year 2 experiments with non-synthetic apertures, a 32-element array of receiver elements would be built. In Year 1 of the program, contractors would produce a high-performance, cost-effective design that would be the key to an affordable array of this size. These experiments would make use of knowledge from the previous stages of the program.

A third set of experiments, conducted primarily during Years 2 and 3, would be designed to examine a technique for 3-D imaging. We refer to the 3-D imaging method as Phase Retrieval with an Opacity Constraint for LAser IMaging (PROCLAIM). This technique relies on measurement of the speckle patterns recorded at a series of wavelengths. A tunable illumination source would be added to the ISTEF experimental suite to perform these experiments. The speckle camera would be used to record speckle patterns at a series of wavelengths. An algorithm invented at ERIM that makes use of an opacity constraint would be tested for the reconstruction of 3-D images. These experiments would build upon the experience gained in the speckle camera experiments.

Long-range imaging experiments would comprise the final set of experiments in this program. These experiments would be begun during Year 1 and performed primarily during Years 2 and 3. They would use the imaging modalities developed earlier in the

program, with emphasis on the 32-element array of heterodyne receivers. Carefully controlled experiments would be designed to perform imaging at ranges of from 10 to 100 km. Potential targets include tethered balloons, manned or unmanned aircraft flying dedicated paths over the ISTEF range, and sounding rocket borne payloads, such as balloons. Each of the receivers developed during the previous phases of the program would be modified and used for these experiments.

At each stage, the imaging testbed would build upon the previous stages, both conceptually and using, to the extent possible, previously acquired hardware. Furthermore, at each stage we would be exploring science questions (described earlier), and so each year's effort would result in tangible accomplishments as well as building toward the further stages

The ultimate goal of the experiments is to image distant targets. However, for the less-mature direct-detection imaging modalities we would start with receiver characterization locally and then experiments indoors at ISTEF before moving to the outside range. Then as the imaging modalities mature, we would perform experiments on the ISTEF outdoor 1 km range and later employ longer up-looking paths using manned or unmanned aircraft, weather balloons, or sounding-rocket payloads as targets.

In parallel with the experimental effort, we would perform extensive analysis, computer simulations, and algorithm development. We would predict received light levels, calculate signal-to-noise-ratios, and derive information-theoretic Cramer-Rao lower bounds on performance. We would also analyze the advantages and disadvantages of sparse arrays over filled arrays. Simulations would include laser power and coherence properties, solid modeling of three-dimensional targets, modeling target surface scattering, polarization effects, atmospheric turbulence (including phase errors, scintillation, and anisoplanatism), receiver aperture configuration, background light, detector area and efficiency, and receiver noise. We would reconstruct images from simulated data and measure their quality (rms error, resolution) to predict the performance of any given imaging scenario. The analyses and simulations would define the expected performance of the candidate imaging modalities. The results of the

analysis and simulation efforts would be readily applicable to a wide range of imaging modalities and scenarios. The experiments would provide data points that would either confirm the analyses and simulations or cause us to refine them so that we can more accurately predict actual performance. Algorithm development would include optimizing sparse-array design algorithms, phasing-up algorithms, and phase retrieval algorithms, and investigating the use of new approaches such as genetic algorithms.

We also considered other possible sets of experiments, including sparse-array direct-detection experiments and quasi-heterodyne experiments. For both of these we decided that, given budgetary considerations, they had lower priority and would yield less significant results than the four experiments outlined above. Both of these experiments would be beneficial as precursors to the sparse heterodyne array experiments. However, since the sparse heterodyne array experiments could take place at an early date, there is less need for the sparse-array direct-detection experiments. The sparse array of heterodyne receivers can provide similar data as the sparse-array direct-detection experiments by simply discarding the phase information. Similarly, the speckle-camera experiments can provide similar data as the sparse-array direct-detection experiments by simply discarding the information from most of pixels in the CCD array. In that way the speckle camera can explore the effect of many different sparse array patterns from a single filled array of data. Many aspects of the quasi-heterodyne array experiments can also be covered by either the speckle camera experiments or the sparse heterodyne array experiments. However, the quasi-heterodyne experiments would have allowed for testing a variety of sparse array patterns in a much more efficient manner. From one set of filled-aperture quasi-heterodyne data we could, by processing selected groups of pixels from the array, try out many different sparse-array patterns.

Section 2.3 give additional details of the experimental plan.

2.2 SCIENCE QUESTIONS

Much of the effort in the planned experiments would entail the fabrication, assembly, and testing of the optical, mechanical, and electronic equipment, integrating

it at the ISTEF site, and performing imaging experiments. In addition, we would conduct experiments that would address numerous scientific questions. Some of them are as follows.

Imaging Performance The most important question is: what is the performance of a variety of active imaging modalities employing sparse, distributed arrays of detectors. We would determine the trade-off between array sparsity, number of speckle realizations, and laser power.

Target Effects What are the effects of the target on the received speckle pattern and on the image? In particular, what is the effect of target flexure and of multiple targets in the field of view rotating at different angular rates. What is the effect of target size, shape, and texture on its spatial power spectrum and on the quality of an image of it? What is the effect of the target geometry and surface microstructure on polarization?

Target Parameter Estimation Short of reconstructing an image, how well can we determine target diameter and other target characteristics from the aperture-plane speckles? How can we optimally estimate target motion from the motion of the detected speckles?

Atmospheric Effects How does imaging performance correlate with the degree of atmospheric turbulence (for both the illumination and the backscattered light)? What is the effect of anisoplanatism on imagery, and how can it be overcome? How much must we reduce the back-scattered light from aerosol scattering, and to what degree do various approaches (such as using a finite bistatic angle, range gating, spectral filtering and spatial filtering) or a combination of approaches reduce it? What laser pulse duration is needed to adequately freeze the atmosphere for different imaging paths?

Illuminator What is the effect of partial coherence of the laser? What wave forms are optimal for the different imaging modalities?

Array Pattern What is the effect of the configuration of a sparse array? In particular, how sparse can the receiver array be while still achieving good image quality? How

important is it that the autocorrelation of the array pattern fill Fourier ("u-v") space? What spatial frequencies are most critical to preserve? What geometric properties are desirable in the configuration of a sparse array?

Other For operation during daylight hours, how much suppression of sunlight reflected from the object, and scattered in the atmosphere, is needed? What is the value of a 3-D signature relative to a 2-D signature?

2.3 EXPERIMENTAL PLAN DETAILS

In what follows we give more detailed plans for the experiments at ISTEF that were outlined in Section 2.1.

2.3.1 Speckle Camera Direct Detection Experiments

We suggest a program that would begin with direct detection experiments. Direct detection in the aperture plane has two primary features that make it attractive for imaging experiments. First, it is several times less expensive to perform direct detection imaging than to use an array of heterodyne receivers and, second, direct detection imaging is not as sensitive to atmospheric phase errors because intensity detection is employed. In addition, direct detection offers flexibility for proving imaging concepts, evaluating performance versus parameters such as aperture fill, and analyzing science issues. To support the development of unconventional imaging, we would construct a speckle camera and conduct direct detection experiments with it. In the sections below we give a program approach for this activity.

2.3.1.1 Speckle Camera Experiments

The primary motivation for the speckle camera experiments is to produce a low-risk, low-cost sensor for early demonstration of unconventional imaging on the outdoor test range at ISTEF. To accomplish this, we would construct a speckle camera experiment as shown in Figure 2-2. The components of this experiment include a CW laser for illumination of targets, target rotation stage for generating multiple

realizations of speckle patterns, a high-speed CCD detector array, frame grabber, computer and transmit/receive optics. This camera would be able to sample speckle patterns from the object at frame rates up to the KHz range. Our approach is to use a class of low-cost, digital-output CCD cameras manufactured by Dalsa Inc. These cameras are available in several array formats (32 x 32, 64 x 64, 128 x 128, and 256 x 256) and operate at maximum pixel rates of 16 MHz. The output of the speckle camera is captured by a digital-input frame-grabber and then stored by a computer. Processing of the speckle data can be performed on either a local computer for initial processing or on other computers to which the data can be transferred. The equipment would be tested first on an indoor test range at ERIM and then on an outdoor test range at ISTEF where long horizontal paths are available.

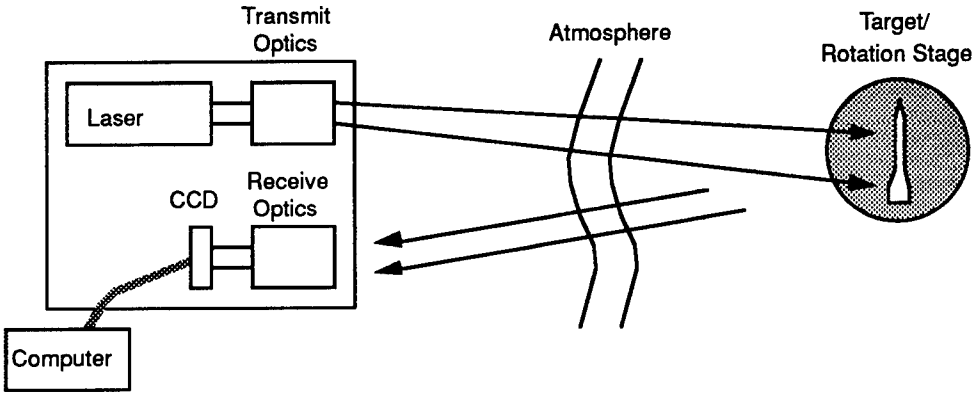

Figure 2-2. Speckle Camera for Direct Detection Imaging Experiments.

The main experiments to be conducted using the speckle camera include image formation experiments and supporting experiments to address various science questions. The two primary image formation methods that would be used for image recovery are imaging correlography [2.1], which yields an incoherent (non-speckled) image, and complex phase retrieval [2.2] which yields a coherent (speckled and complex-valued) image. These methods for image recovery are discussed in greater depth in Appendix A. The collected data would consist of a filled array of measurements; we can also simulate the effect of a sparse, distributed array by processing only a selected subset of the data. The science issues to be addressed are discussed in Section 2.2. They include image quality, the effects of target properties and motion on the speckle pattern, polarization effects, array-pattern trade-offs,

atmospheric effects, and so forth. The path at the outdoor test range at ISTEF can provide challenging atmospheric conditions due to its proximity to the ground and extended path lengths. While direct detection is much less sensitive to turbulence than heterodyne detection, direct detection is sensitive to anisoplanatism, beam wander, and break-up (scintillation) for both the outward and return paths. As part of these experiments, atmospheric conditions would be monitored, and modifications to the beam path, such as elevating it from the ground and adapting the length, would be considered.

Table 2-1 contains a discussion of various parameters and how they affect the speckle camera experiments. As an example we give parameters for a relatively benign value of the atmospheric structure function, C_n^2. More stressing turbulence would cause us to use smaller targets and larger speckle demagnifications. Measurements of C_n^2 at the site would be necessary for the final design of the experiment.

Table 2-1. Impact of Various Parameters on Speckle Camera Experiments

Experimental Parameter	Comment
Target Size	Object size must be smaller than isoplanatic patch size. Preliminary analysis gives object size of 10 cm at 1 km range.
Target Material	Variety of materials would be evaluated. Examples include: diffuse paints, depolarizing coatings, specular metal, or retro-paint for boosting signal.
Speckle Size	For target diameter D = 10 cm at range R = 1 km and $\lambda = 0.5\ \mu m$, speckle size ($\lambda R/D$) is 5 mm.
Target Rotation	Target rotation causes speckle patterns to translate. Generation of independent speckle realizations requires rotation of $N\lambda/D$ radians, where N is # of speckles across array. For N = 32, rotation of 0.16 mrad is required. Measurements of rotation rate can be made for rates up to roughly 1 rad/sec.
Path Geometry	Bistatic path is desirable for background rejection. Background rejection can also be achieved by locating laser near target and/or folding path. Path can also be elevated to reduce turbulence.
Signal Level	Signal levels for diffuse targets are marginal for highest frame rates. To boost signal level, retro-paint can be used, or detector-array master clock rate can be reduced.
Daytime Operation	MODTRAN calculations show that daytime operation is feasible with 10 nm spectral filter.
Optics Size/Magnification	Size of receiver fore-optic encompasses N x N speckles. For N = 32, fore-optic is 0.16 m in diameter. For 2 x 2 sampling of speckles onto 16 μ pixels, demagnification of pupil by 156x is required. Can be accomplished using a telescope/microscope objective pair.

2.3.1.2 Algorithm Development

The main aspect of algorithm development would be the application of previously demonstrated image recovery algorithms to the data generated by the speckle camera. For complex phase retrieval it would also be necessary to develop improved estimates of the support on the autocorrelation from the computed autocorrelation function [2.3]. This is made difficult because the autocorrelation function is speckled. For the case of

sparse arrays, the problem is compounded. Algorithms would be developed to format and calibrate data, then adapt image formation and speckle analysis software to the available computer platforms. The speckle analysis software includes features such as estimation of target rotation rates and rotation axis from translating speckles. In addition, control and diagnostic software would be required for (a) capturing multiple realizations of the speckle data as the target is rotated under computer control, and (b) assessing the quality of the speckle patterns for various atmospheric conditions and detection circumstances, such as noise level and sampling geometry.

2.3.1.3 Experiment Simulation

Assessment of the operation of image recovery algorithms developed for the speckle camera requires the ability to simulate speckle patterns that correspond to the type of targets being imaged under appropriate atmospheric and detection conditions. To accomplish this, we would generate reflectance models of the targets and then apply statistical processes associated with scattering and propagation through the atmosphere. We would then apply detector sampling and noise processes to generate versions of the detected speckle patterns. Resulting speckle patterns would then be used as input to image recovery and speckle analysis algorithms. Simulated recovered images and speckle parameters would then be compared to actual images and parameters reconstructed from the real data. This comparison is valuable for analyzing nonintuitive effects that may arise in either collected or simulated data.

2.3.1.4 Experiment Design and Analysis

Early in the program we would conduct an experiment design and analysis task. We have already performed feasibility calculations of atmospheric turbulence parameters and signal power levels. This analysis would be refined and used for detailed experimental design, which would allow us to determine experimental parameters such as maximum target size and maximum range, and specify optical components.

2.3.1.5 Hardware Fabrication/Acquisition

Upon completion of the design task, the speckle camera would be fabricated. This involves the acquisition of new hardware components and fabrication of some components such as mounting hardware for optics.

2.3.1.6 Hardware Integration/Lab Testing

Following completion of the hardware fabrication and acquisition, we would integrate and test the speckle camera at a 20-meter indoor test range at ERIM in Ann Arbor. At ERIM we have access to auxiliary equipment, including electronic test equipment, that would be required for integration and testing. For testing at ERIM we would use an existing argon laser for illuminating targets. This testing phase would include characterization of the recorded data by evaluating properties such as the speckle statistics and demonstration of image recovery.

2.3.1.7 Field Experiment Execution

Once lab testing is complete, we would transport the speckle camera to the ISTEF facility for experiment execution. The laser power required is 1 or 2 watts, preferably in the green. As mentioned above, we would use an existing argon laser as a source at ERIM. For this effort we require an appropriate laser at ISTEF, which could be either an argon laser or a frequency-doubled, CW, YAG laser. If no such lasers are available, an ERIM laser could be used. We would perform initial experiments at a relatively modest range, and then perform the main experiments at the 1-km range and longer ranges. An important consideration in the design of the experiments is the laser power level. The desirable received light from the target is significantly above the noise level of the detector. The energy received by each pixel of the array is given by

$$E = \frac{P_L \lambda^2 \Delta t \eta_{obj} \eta_T}{2\pi D^2} \qquad (2.1)$$

assuming that the target is perfectly diffuse and the detector size is equal to the speckle size. With the laser power P_L = 1.0 watt, λ = 0.5 μm, Δt = 1/12,000 second (which

is the fastest rate for the 32 x 32 CCD camera), object diameter D = 5 cm, object illumination efficiency $\eta_{obj} = 0.2$, and path-length transmittance of $\eta_T = 0.5$, it follows that $E = 5.3 \times 10^{-16}$ joules. This value should be compared to the CCD noise value of 4.48×10^{-16} joules/pixel. Note that for this worst case of short integrations and diffuse target the return is roughly equal to the CCD noise level. This relationship is improved by orders of magnitude by slowing the CCD frame rate to 100 frames per second (which gives two orders of magnitude) and using, if necessary, retro-reflective paint on the targets. Also note that, as long as the detector size scales with the speckle size, the receiver power is independent of target range.

2.3.1.8 Image Formation/Data Analysis

Following speckle camera installation and data collection, image-formation and speckle-analysis algorithms would be exercised.

2.3.2 Short-Range Distributed-Array Heterodyne Experiments

A significant goal of the suggested experiments is to demonstrate imaging with a distributed array of heterodyne receivers. To accomplish this, we would make use of infrastructure capabilities developed under the speckle camera task described in Section 2.3.1. In cooperation with other contractors, we would use heterodyne receiver elements built by CREOL to generate images of coherently illuminated targets. Challenging aspects of this task include designing sparse arrays that use aperture synthesis methods to generate discernible images with limited numbers of receiver elements and applying phase-error correction algorithms that are required to phase-up the receiver array and to correct for atmospheric turbulence. ERIM's approach for these distributed-array experiments makes use of significant expertise that we have gained through several years of research on unconventional imaging and is outlined below.

2.3.2.1 Experiment Specification

The distributed-array heterodyne experiments have three primary tasks. First, with other contractors, we would contribute to the design of the heterodyne receiver elements and array configurations. Our primary input would be to establish performance specifications required for robust image formation and to aid in the evaluation of designs to ensure that the performance specifications are met. For example, image formation with heterodyne receivers requires measurement of the complex-valued optical field and these measurements are subject to errors from sources such as detector noise and background light. To correct for array-phasing errors and atmospheric turbulence, the field measurements must be made with sufficient accuracy. Also, in order for the experiments to succeed, certain detector noise and signal level specifications must be met. Other aspects of receiver element design that are crucial for experiment success include the mechanical robustness of the receiver elements. The bandwidth of phase errors imparted by mechanical disturbances of the optical fiber network must be lower than the image formation bandwidth to ensure that the systematic phase errors are constant over the data collection time. To accomplish this task ERIM would establish performance specifications and evaluate design approaches for meeting them in cooperation with other contractors. In addition we would develop diagnostic software for the assessment of measurement quality.

The second task is to use a limited number of receiver elements (eight) along with aperture synthesis methods, to generate target images at the 1- and 3-km test ranges at ISTEF. These experiments would be conducted in cooperation with other contractors. ERIM would contribute to the areas of algorithm development, experimental design, simulation, and image formation. More specifically, we would develop experimental procedures for conducting aperture synthesis based on object rotation. In addition, ERIM would provide algorithms for data assessment, phase error correction, and image formation. The phase-error correction algorithms must remove phase errors caused by array misalignment and atmospheric turbulence. Because the atmospheric component of the phase errors is time-variant it is likely to be the most difficult to correct, particularly since aperture synthesis requires an extended time interval for data collection. Ideally, the atmospheric phase would be frozen (quasi-static) during the

aperture synthesis interval so the resulting phase error is one-dimensional; in this case the Digital Shearing Laser Interferometry phase-error correction algorithm can be used [2.4]. We would also explore ways to correct phase errors when they are changing within the data-collection time.

For the third task we would use an increased number of receiver elements (32) for image generation without aperture synthesis. Key elements of this task would include the development of algorithms for phase-error correction and, in cooperation with another contractor, the design of array formats that fill the largest area with a small number of elements. In previous work we have developed phase-up algorithms based on image sharpness that allow for correction of a constant phase error on each receiver element that is attributable to the array not being phase aligned [2.5]. These algorithms ideally require multiple realizations of the pupil-plane speckle field; however, we have also used sharpness to correct for similar phase errors encountered in Synthetic Aperture Radar (SAR) when only a single realization of the speckle pattern is available [2.6]. After phase correction, images are recovered by Fourier transformation. Image quality would then be assessed by comparison of reconstructed images to simulated images.

2.3.2.2 Algorithm Development

As discussed above, a key element of these experiments is algorithm development. The algorithms of primary importance apply to data diagnostics, phase error correction and image formation. Once these algorithms are developed they would be ported to the primary data collection and image formation computers at ISTEF for application. For algorithm development prior to the availability of field data, we require simulated data as discussed below.

2.3.2.3 Experiment Simulation

Simulated data sets are required for algorithm development and evaluation of experimental results by comparing them to ideal simulated images. ERIM has had several years of experience in generating simulated imagery including ideal target

models, the effects of atmospheric turbulence, imperfect data-collection hardware, and phenomenology modeling. Important aspects of the simulations required for this task include accurately modeling the various image-degrading processes (atmospheric turbulence, detector noise, etc.) to evaluate the entire image-formation process and diagnose unanticipated problems.

2.3.2.4 Experiment Design and Analysis

Our primary tasks are to ensure that the hardware meets the required performance levels for image formation and to help with the experimental design so that meaningful images are obtained with the limited number of receiver elements. To provide this support we would conduct analyses of the image formation processes to determine various hardware performance specifications and to design experiments. In addition, we would develop diagnostic software to use in the laboratory and field for assessment of data quality.

2.3.2.5 Field Experiments

Field experiments would be conducted on the test ranges at ISTEF. During these experiments we would provide support primarily to ensure that the data are of sufficient quality for image formation. For the first experiments, which use a small number (eight) of receivers, aperture synthesis is recommended. Experiments would require careful adjustment of object rotation rate and careful monitoring of atmospheric and alignment phase errors. Evaluation of these effects would require the use of the diagnostic software for data assessment. It is expected that this data assessment would occur as data are being collected so that adjustments can be promptly made. The second set of experiments would again require the careful assessment of the data collection process and evaluation of output data using diagnostic software.

2.3.2.6 Image Formation/Data Analysis

We would exercise our phase error correction algorithms and image formation software, and to assess the results relative to ideal simulated data. This work would

involve the two main experiment types (small number of receivers with aperture synthesis and larger number of receivers without aperture synthesis). It is also anticipated that several trials of each experiment type would be conducted to obtain improved performance, gain experience, and answer science questions.

2.3.3 Three-Dimensional Imaging Experiments

The PROCLAIM imaging modality is attractive because of the improved identification capability offered by three-dimensional imaging and because only the intensity data are directly detected. The advantages of direct detection, including robustness to atmospheric phase aberrations and savings in expense and complexity relative to heterodyne detection, apply to the PROCLAIM modality. Furthermore, the speckle camera that would be developed under the first set of experiments can be used for PROCLAIM experiments. The philosophy of this modality is to trade hardware complexity for increased computational load. In this section we describe the algorithm development, experiment design, simulations, hardware acquisition and integration, and testing, all leading to a field experiment in which the novel PROCLAIM three-dimensional imaging modality would be demonstrated on a 1-km horizontal test range.

2.3.3.1 Three-Dimensional Experiment Specification

There are many illumination strategies that can be considered for the PROCLAIM imaging modality. As discussed in Section 6, we performed analyses to show the preliminary feasibility of using a serial-illumination strategy to image a missile or some other long-range target from the ground with the PROCLAIM concept. For PROCLAIM to work, the target should be relatively stable over the illumination sequence. Using the rather restrictive criterion that the speckle pattern does not move more than half a speckle width during the entire collection sequence, we arrive at the following condition on the target's angular frequency of rotation,

$$\omega < \frac{\lambda c}{8 N D_{obj} Z_{obj}} , \qquad (2.2)$$

where ω is the object angular frequency, λ is the wavelength, c is the speed of light, N is the number of frequency samples or equivalently the number of range bins desired, D_{obj} is the cross-range diameter of the object, and Z_{obj} is the depth of the object in range. Let $D_{obj} = 5$, $Z_{obj} = 2$ m, $\lambda = 1$ μm, and suppose that we desire $N = 10$ range bins. The maximum angular velocity that can be tolerated for such an object is found to be $\omega < 0.375$ radians/second. This sample calculation suggests that the requirement on object angular frequency is not particularly restrictive and that there are likely to be many objects that can be imaged with serial-frequency illumination. Therefore our ground experiments would be designed to investigate this illumination modality.

The actual layout of the experiment would be closely related to the speckle camera experiments, discussed in Section 2.3.1. Consequently, the PROCLAIM experiments would greatly benefit from the experience gained and infrastructure developed in the speckle-camera experiments. We have performed a preliminary experiment design that suggests that a three-dimensional object, such as a cone painted with retro-reflective paint, can be imaged at a range of 1 km. Anisoplanatism is much more challenging in this horizontal-imaging scenario than in the envisioned application of PROCLAIM, namely looking up to identify missiles. As with the speckle camera experiments, the object would need to be no larger than the isoplanatic angle, on the order of 10 cm in clear conditions. The same re-imaging optics that would be used in the speckle camera experiments can be used here as well.

The PROCLAIM experiments differ from the speckle-camera experiments in one fundamental way: a frequency-tunable laser is needed for illumination. A coordinated illumination, frame-detection, and data-storage sequence would be controlled by a computer. In this way the required data set, consisting of far-field speckle (intensity) patterns for each of several illuminating frequencies, would be obtained.

2.3.3.2 Algorithm Development

Since the PROCLAIM concept trades hardware complexity for increased computational load, one might properly infer that the algorithms needed for three-

dimensional image reconstruction are somewhat complicated. A gradient-search algorithm has been developed by ERIM researchers and it has been demonstrated in a simple simulation [2.7]. This algorithm would have to be developed to accommodate noise and the effects of diffraction.

We believe that the opacity constraint can be used not only for phase retrieval, but also for estimating very tight bounds on the object support, given the object's three-dimensional autocorrelation function (or equivalently, the object's three-dimensional Fourier intensity). Such a bound on the support or extent of the object is called a locator set and ERIM researchers have previously developed locator set algorithms for two-dimensional data sets that can readily be generalized to accommodate three-dimensional data sets [2.3]. Preliminary analysis suggests that locator sets for opaque objects can be made very tight and would provide excellent initial estimates in a phase-retrieval algorithm. It may actually be possible to identify a specific target from a tight locator set that would give strong target profile information. We would develop both phase-retrieval and locator-set algorithms for coherent three-dimensional opaque objects.

2.3.3.3 Detailed Experiment Design

This design would follow from the detailed design performed for the speckle camera experiments. The object would be designed so that significant depth information can be retrieved and so that it can be rigidly mounted. The detailed design of the illumination, detection, and data-storage sequence would have to be performed separately for the PROCLAIM experiments, as it involves multiple wavelengths.

2.3.3.4 Experiment Simulation

Once the algorithms have been developed and the detailed experiment design has been performed, we would perform simulation experiments that conform to the intended field experiments. The same speckle simulation algorithms developed in the speckle-camera experiments would be used in this simulation but with wavelength diversity added. The simulation would provide confidence that we can succeed with the

field-experiment demonstration. In addition, the exercise would provide a means of isolating the source of non-intuitive effects that may arise in the collection of data or the reconstruction of three-dimensional objects.

2.3.3.5 Hardware Acquisition/Fabrication

Much of the hardware required for the PROCLAIM experiments would already have been acquired for the speckle-camera experiments. Of course the frequency-tunable laser would have to be acquired. ERIM has a frequency-tunable laser that can readily be used in the laboratory integration and testing phases. We would rely on government-furnished equipment (GFE) for this component of the outdoor experiment. The laser would need to have a gain curve that would provide the desired range resolution, which is given by

$$\rho_r = \frac{c}{2\Delta v} , \tag{2.3}$$

where Δv is the bandwidth over which the source is tuned. To get a range resolution of 1 cm, we require $\Delta v = 1.5 \times 10^{10}$ Hz or $\Delta\lambda = 0.25$ Angstroms. Therefore, it should be easy to achieve the desired range resolution. The laser would be tuned with a precisely rotatable etalon that is placed in the laser cavity and is electronically controlled with the data-acquisition computer.

2.3.3.6 Hardware Integration and Laboratory Testing

Before the equipment is transported to the ISTEF test range, we would integrate the experimental hardware in a laboratory test range so that the integrated imaging system can be tested and validated. Again, we would benefit from laboratory tests performed in the speckle-camera experiments. This integration task would give us additional experience and may suggest adjustments to the detailed experiment design.

2.3.3.7 Execution of Field Experiment

When the laboratory equipment testing and integration are completed, the equipment would be transported to the ISTEF facility to conduct the field experiment. The ultimate goal of the entire three-dimensional imaging task is to demonstrate the feasibility and utility of the PROCLAIM imaging modality on the ISTEF horizontal test range at a range of 1 km. This would help to establish the importance of the third dimension of information for target discrimination. This could motivate the extension of the heterodyne array imaging from two dimensions to three.

2.3.3.8 Image Formation and Data Analysis

The phase-retrieval algorithms would be installed on ISTEF computers and images would be formed after the data are collected. These images would be scored primarily with regard to how well the target profile is recovered. Experimental results would be compared with simulation results.

2.3.4 Long-Range Imaging Experiments

The final set of experiments to be conducted in the series concern imaging of distant targets. Emphasis would be on using the 32-element array of heterodyne receivers discussed in Section 2.3.2, but experiments with the speckle camera would be conducted as well. These experiments are to be conducted at ranges greater than 3 km and would make extensive use of hardware and software developed under previous tasks. Our approach for these experiments is discussed in greater depth below.

2.3.4.1 Experiment Specification

The purpose of these experiments is to demonstrate long-range imaging using primarily an array of heterodyne receivers. However, other sensors developed under the program would also be tested for long-range capability. Initial analysis of the long-range experiments indicates that the target should be elevated to avoid the extreme atmospheric conditions present for a long horizontal path. Two options for target

location exist: the target can be located on a distant tower, or an airborne target can be used. Certainly the airborne target can provide a path that is closer to vertical, and thus encompasses lower turbulence levels. However, tracking of an airborne target can be more challenging. Furthermore, the class of airborne targets is limited by characteristics of the heterodyne receiver array. Specifically, the receiver bandwidth and frequency offset are obtained using acousto-optic methods that have insufficient bandwidth to record the high frequencies inherent to high-speed targets such as rockets, unless they are traveling approximately perpendicular to the line of sight. (This would not be a limitation of an eventually deployed system.) This feature drives the experiments to use stationary or slowly moving targets. Of the several candidates for stationary airborne targets (tethered balloons, helicopters, remotely piloted vehicles (RPV), etc.), our preliminary analysis shows that a good candidate is an RPV in the form of a radio-controlled helicopter with the target tethered below it. These RPVs are capable of flying at altitudes limited to first order by the ability to see the RPV. We estimate that such an RPV can be piloted by using a telescope to an altitude of 3 km. The target, which can have a weight of roughly 3 lb, is tethered at a distance of up to 100 ft below the RPV. The tether would be designed to damp vibrations from the RPV engine. For greater altitudes, a manned helicopter can be used, however, the expense is considerably greater than for an RPV. Other options that we have considered include tethered and non-tethered balloons; however, these approaches are not as controllable. Sounding rockets may be used, but their cost limits the number of experiments that can be performed.

One desirable feature associated with using a vertical path (airborne target) is that the level of turbulence is significantly lower than for a horizontal path. Thus the atmospherics, the anisoplanatic patch size in particular, may be less of a problem for airborne experiments. It is anticipated, however, that tracking would be a significant complication for the airborne case.

Because of the long ranges involved, these experiments would be made difficult by the lower signal levels. These signal levels can, however, be offset by using larger receiver optics. If the receiver aperture is scaled with the speckle size, the signal level

is independent of range. Thus for long ranges we would anticipate replacement of the fore-optics for the various imaging sensors.

2.3.4.2 Experiment Execution

We anticipate that these long-range experiments would make significant use of hardware, software and capabilities developed for previous experiments. The effort would thus concentrate on customizing the hardware, such as mounting the sensors on tracking mounts and modifying collection optics, and planning and execution of the experiments.

2.4 SECTION 2 REFERENCES

[2.1] P.S. Idell, J.R. Fienup and R.S. Goodman, "Image Synthesis from Nonimaged Laser Speckle Patterns," Opt. Lett. 12, 858-860 (1987).

[2.2] J.R. Fienup, "Reconstruction of a Complex-Valued Object from the Modulus of Its Fourier Transform Using a Support Constraint," *J. Opt. Soc. Am. A* 4, 118-123 (1987).

[2.3] T.R. Crimmins, J.R. Fienup and B.J. Thelen, "Improved Bounds on Object Support from Autocorrelation Support and Application to Phase Retrieval," *J. Opt. Soc. Am. A* 7, 3-13 (1990).

[2.4] J.N. Cederquist, J.R. Fienup, J.C. Marron, T.J. Schulz and J.H. Seldin, "Digital Shearing Laser Interferometry for Heterodyne Array Phasing," in *Laser Radar VI*, R.J. Becherer, ed., Proc. SPIE 1416 -43 (1991).

[2.5] J.R. Fienup, A.M. Kowalczyk and J.E. Van Buhler, "Phasing Sparse Arrays of Heterodyne Receivers," presented in Orlando, Fla., and published in Proc. SPIE 2241-15, Inverse Optics III (April 1994), pp. 127-131.

[2.6] R.G. Paxman and J.C. Marron, "Aberration Correction of Speckled Imagery with an Image-Sharpness Criterion," in *Statistical Optics*, Proc. SPIE 976 -05, San Diego, CA, August 1988.

[2.7] R.G. Paxman, J.H. Seldin, J.R. Fienup, and J.C. Marron, "Use of an Opacity Constraint in Three-Dimensional Imaging," presented in Orlando, FL, and published in Proc. SPIE 2241-14, Inverse Optics III (April 1994), pp. 116-126.

3 TRADE-OFF BETWEEN ARRAY SPARSITY AND NUMBER OF REALIZATIONS

The quality of a reconstructed image depends on numerous factors, including signal-to-noise ratio (SNR), aperture diameter, aperture fill, distance to target, target structure, wavelength, phase errors, scattered light, etc. In this section we show digital simulations demonstrating the trade-offs for (a) different amounts of aperture fill, (b) different numbers of speckle realizations, and (c) different types of objects. We do this both for noise-free diffraction-limited coherent imaging and for noise-free imaging correlography.

For a review of coherent imaging and imaging correlography, see Appendix A.

3.1 DIFFRACTION-LIMITED COHERENT IMAGING

Images from coherent systems also suffer from a mottled appearance that we call speckle, which decreases image intelligibility. We can decrease the image speckle by collecting several frames of data, each with the object having translated or rotated slightly, which would result in different realizations of the speckle pattern. By averaging the intensities of these speckled images we arrive at an image with reduced speckle. Averaging over a large number of speckle realizations results in an image that is equivalent to a speckle-free image of the target.

For the case of imaging with sparse, distributed arrays of detectors, the details of the shape of the impulse response play a major role in image quality. The impulse response from a filled array typically has a bright, narrow mainlobe that contains most of the energy and small sidelobes. For a sparse array having a length comparable to the length of a given filled array, the impulse response would be similarly narrow, but it would contain only a small fraction of the energy, and most of the energy would be in the sidelobes. The result is typically an image having similar resolution as that from a filled array, but having much poorer contrast and many artifacts. Equivalently, the optical transfer function (OTF), or its magnitude, the modulation transfer function (MTF) drops off quickly at the lower spatial frequencies as compared with the MTF

for a filled array, which typically has approximately a triangular shape. For reducing speckle artifacts, for distributed arrays we need a greater number of realizations than for a filled array from the simple point of view that we are measuring fewer speckles at any given time. Similarly, we are measuring a proportionally smaller number of photons.

The theoretical signal-to-noise ratio for an average of K speckle images is, in the regime of low sensor and photon noise (i.e., dominated by coherent speckle effects) [3.1]

$$SNR(u) = |\mu(u)| \sqrt{K\ SBP\ |OTF(u)|} \tag{3.1}$$

where u is a 2-D spatial-frequency coordinate, $|\mu(u)|$ is the magnitude of the Fourier transform of the incoherent object normalized to be unity at the origin, SBP is the space-bandwidth product of the data and OTF(u) is the optical transfer function (the autocorrelation of the aperture when normalized to unity at the origin). SBP equals N_s, the number of subapertures, if the system does not oversample the speckle pattern. Suppose we have a square filled array with L subapertures on a side, or a total of L^2 subapertures. Then SBP = L^2, and at the middle spatial frequencies OTF = (1/2), so SBP OTF = $L^2/2$. For an efficient sparse array, however, we might have $N_s = 3(L - 1)$ subapertures (see the section on array design). For a nonredundant sparse array, OTF(u) = $1/N_s$. For a typical array pattern we would have OTF(u) = $1/N_s$ at many of the middle spatial frequencies. Then for the sparse array SBP OTF = $N_s/N_s = 1$. Hence the factor $\sqrt{SBP\ OTF}$ in the expression for SNR is $L/\sqrt{2}$ times greater for a filled array than for a minimally-filled sparse array. Hence to make up for this we would need the number, K, of speckle realizations to be $L/\sqrt{2}$ times greater for the sparse array. We could also argue that, at the spatial frequency components outside the DC component, the OTF of an efficient sparse array has an average value of the OTF of about $2/N_s$. Hence we may need only $L/(2\sqrt{2}) \approx L/2.8$ times as many speckle realizations for the sparse array. Alternatively, we can build sparse array patterns that are not minimally redundant but purposely have some redundancy. For example, with $4L - 2$ subapertures we can guarantee that each spatial frequency has an OTF of at least 2. Then the factor SBP OTF = $N_s 2/N_s = 2$, and we would need only half as many realizations as with the minimally redundant pattern of $3L - 3$ subapertures.

After averaging image intensities to form a speckle-reduced image, we may apply a Fourier-domain filter that boosts the higher spatial frequencies so that, in the case of high signal-to-noise ratio (SNR) it can regain the character of an incoherent image through a filled aperture. This factor makes sparse arrays particularly appealing: with enough averaging and with filtering we can overcome both the speckle effects and reduce the large sidelobes to retrieve a speckle-free image that is as good as one that would have come from a filled aperture costing several times as much.

By computer simulations we demonstrated the trade-off of aperture fill versus number of speckle realizations for different classes of objects. The top row of Figure 3-1 shows coherent images as seen through a filled aperture in the shape of a circle. The bottom row shows images of the same object as seen through a sparse array consisting of 21 small circles, arranged in an annulus with outer diameter equal to the diameter of the filled-aperture circle. The object consists of a rectangle of size 2x3 pixels plus four additional points, each 1x1 pixel in size. This could represent a resolved post-boost vehicle with nearby unresolved re-entrant vehicles or decoys. We consider this "four-points" object to be a fairly simple object. An ideal (diffraction-limited and noise-free) incoherent image of the object is shown in the upper right of Figure 3-1. The slight fuzziness is due to the impulse response of the circular aperture. A single coherent image of the object is shown in the second column of the first row. The image is complex valued, and the figure shows the intensity of the image. Note that the relative brightnesses of the points is distorted and the 2x3-pixel block at the top is broken up. The coherent nature of the imaging process produces laser speckles in the image that cause these effects. Each speckle realization would break up and distort the image intensity in a different way. By noncoherently averaging (i.e., averaging the intensities of) images with several different speckle realizations, we can reduce the speckle artifacts to arrive at an image that more closely resembles the incoherent image. The third and fourth columns show the effect of averaging ten and one hundred speckle realizations, respectively. Even with as few as ten speckle realizations the image looks like a somewhat noisy version of the ideal incoherent image for this simple object through the filled aperture. The average of one hundred realizations is visually nearly perfect.

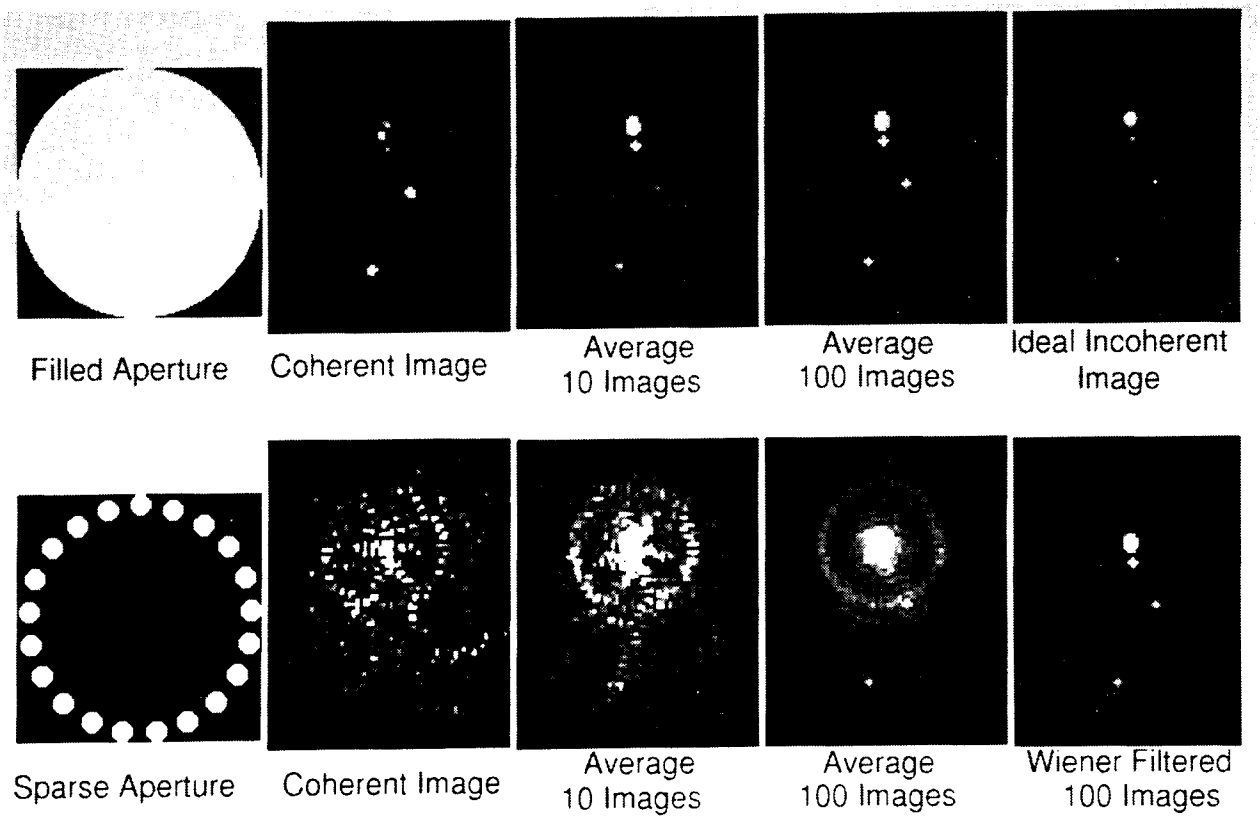

Figure 3-1. Imaging Four-Points Object Through a Sparse Aperture of 21 Circles.

The first four columns of the second row of Figure 3-1 show the same thing as the first row, but for the case of the sparse aperture consisting of 21 small circles. The single coherent image is almost indecipherable. The average of ten realizations starts to bring out some of the features. All four parts to the object finally become discernible after averaging 100 realizations. The ring-like artifact that is especially evident around the 2x3 block part of the image is a sidelobe due to the sparse aperture. This artifact can be greatly reduced by Wiener filtering [3.2], the result of which is shown in the rightmost column of the second row. In the process of filtering the sidelobes are greatly reduced, but at the cost of slightly coarser resolution and a slight enhancement of the background noise. The quality of the Wiener-filtered average of 100 images through the sparse aperture is slightly better than the average of only ten realizations from the filled aperture. This is consistent with the fact that there is about five times as much area covered by the filled aperture as by the sparse aperture.

We can appreciate the effect of the sparse aperture better by looking at Figure 3-2. The first column shows the original object without the effects of speckle or low-pass filtering by the aperture. The second column shows the speckle pattern in the aperture plane caused by a coherent realization of the object. This and the next two columns are shown demagnified by a factor of two compared with the aperture functions shown in Figure 3-1. The 21-subaperture sparse array collects the speckles shown in the third column. The aperture pattern itself constitutes the coherent transfer function that defines the impulse response for coherent imaging. Note that the patterns evident in the speckle pattern that would have been evident in a filled-aperture collection are less evident in the sparse array collection. The right-most column shows the optical transfer function (OTF) of the sparse array pattern. This is the transfer function for the noncoherently averaged image. The central part was overexposed lest the surrounding parts be too dark to see clearly. This demonstrates the property of sparse aperture that the high spatial frequencies have little energy compared with the low spatial frequencies. Furthermore, the detailed structure of the OTF causes distortions of the objects Fourier transform that cause a distortion in the image. The Wiener filtering step is essentially dividing by the OTF in order to compensate for its distortion. The Wiener filter also includes a noise term that prevents us from unduly enhancing the

noise by dividing by too small a number where the OTF is small. This is described further at the end of this section.

Figure 3-3 shows similar images for a second object, consisting of a cylinder (post-boost vehicle) with five cones (re-entrant vehicles) attached plus a sixth cone detached from the cylinder. This object, which we call "bus+rv" can be thought of as a much finer-resolution image of the central portion of the four-points object, for which the cylinder is now well resolved, allowing us to count the number of cones attached and to discern their shape. Note that, from a single coherent image (top row, second column) from a filled aperture, the speckle artifacts make it impossible to identify the attached cones. Only the overall shape can be easily discerned. The noncoherent average of one hundred image realizations, shown in the third column, yields a good-quality image that is a somewhat noisy version of the ideal incoherent image. Recall, however, that for the four-points object the average of 100 realizations yielded an almost perfect image. The bottom row shows the results through the same sparse aperture as before. The single coherent image shown in the second column is almost totally useless—the existence of the detached cone is not even evident. The noncoherent average of one hundred images, shown in the third column, contains some information, and it is improved considerably by Wiener filtering, as shown in the fourth column. We can clearly see the separated cone (although it may be difficult to tell that it is a cone), and the cones attached to the cylinder can be seen, but counting them is difficult. Hence we see that, for the same aperture and the same number of image realizations, the image of the four-points object has considerably higher quality than the image of the bus+rv. We can understand this from the spatial power spectra of the two objects, which are shown in Figure 3-4. The spatial power spectrum (and its square root, which is the magnitude of the Fourier transform of the underlying incoherent object) of the bus+rv, which is an extended object, falls off much more rapidly than that of the four-points; hence the signal-to-noise ratio (SNR) at the higher spatial frequencies is much lower for the bus+rv object since there is just less signal there.

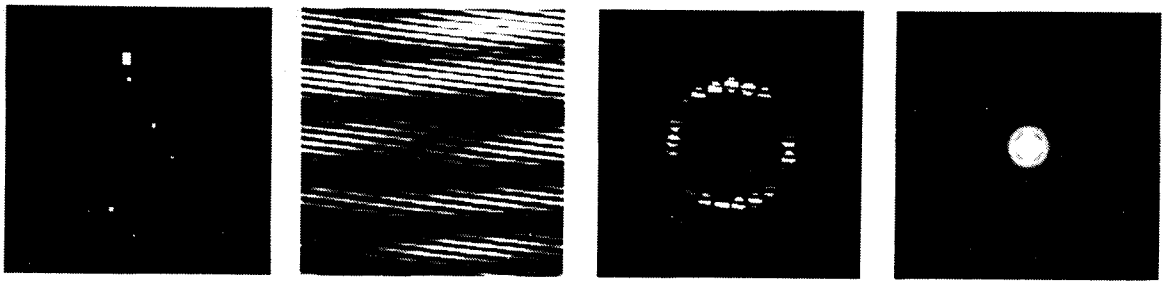

Figure 3-2. Transfer Functions for Imaging Through a Sparse Aperture of 21 Circles.

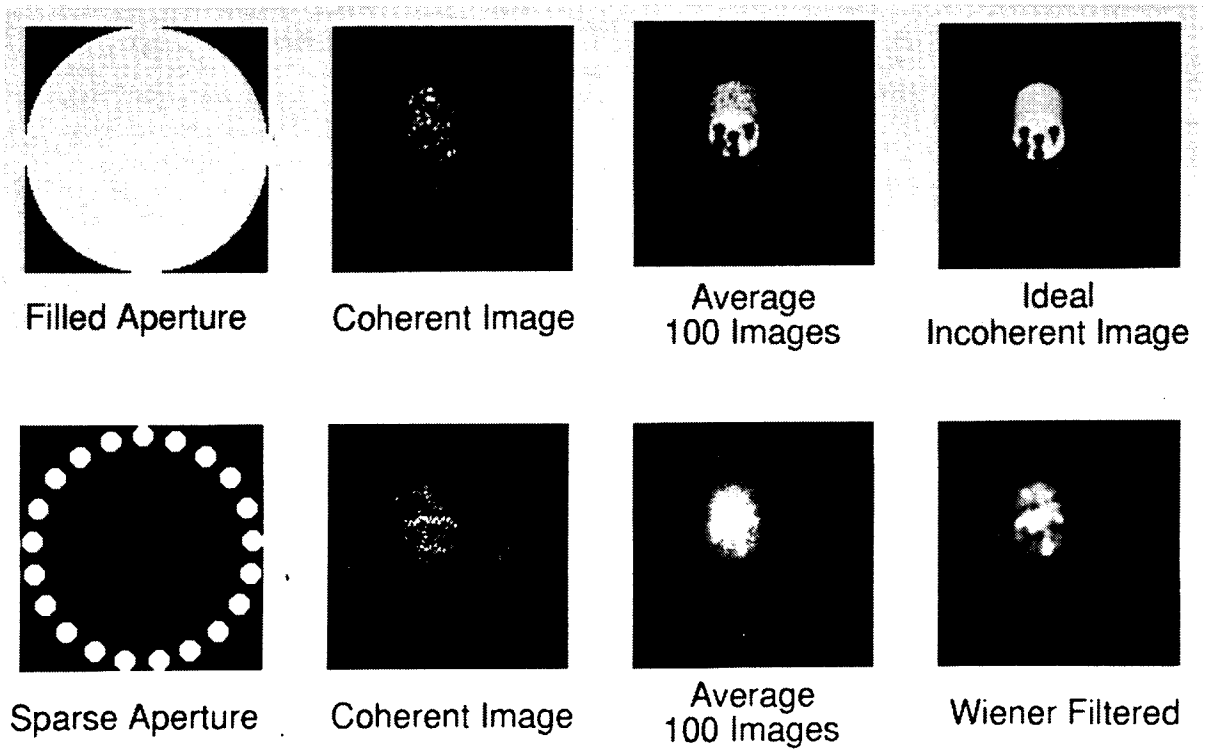

Figure 3-3. Imaging Bus+Rv Object Through a Sparse Aperture of 21 Circles.

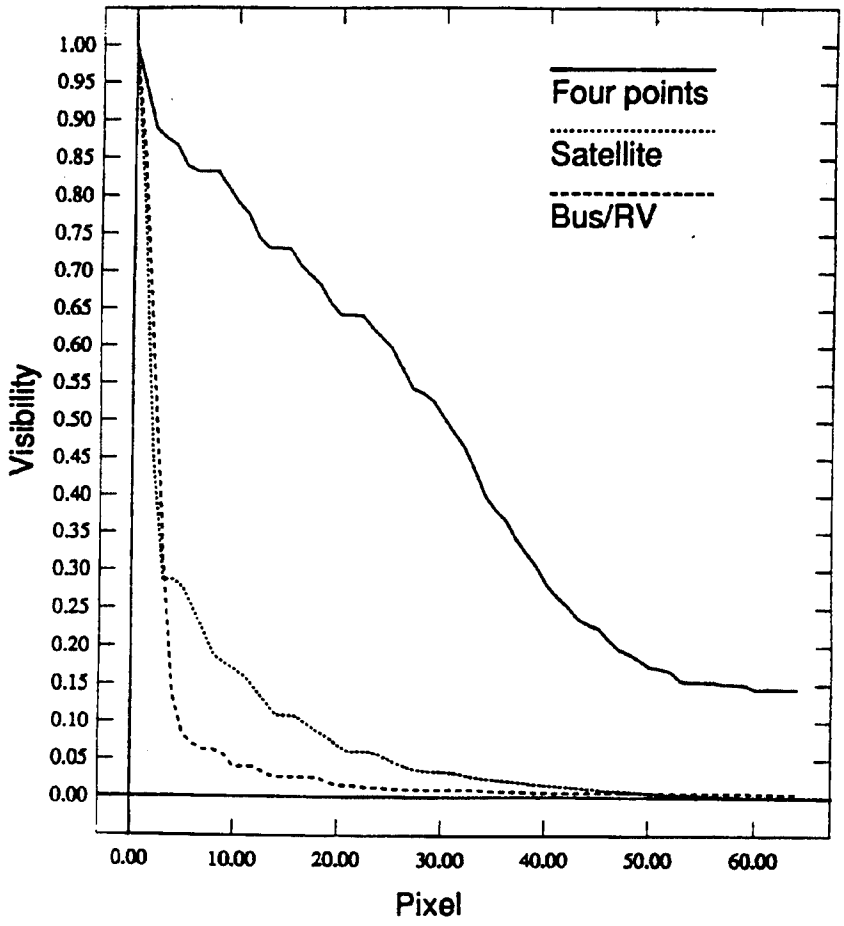

Figure 3-4. Spatial Power Spectra of Three Objects.

The examples above with the aperture consisting of 21 small circles are for the case of each small circle having several detectors across it. Hence the total number of detectors is several times 21. Suppose, on the other hand, that the total number of detectors is a similar small number, only 22. Figure 3-5 shows the result for a small quasi-random array consisting of just 22 detectors. Henshaw [3.3] designed this array configuration using a genetic algorithm (see Section 8). Note that the apparent resolution is many times coarser than for the 21-circles aperture because of the great difference in numbers of detectors. Figure 3-5 shows the bus+rv and 4-points images, at a lower resolution, as seen through the small-array aperture. Note that the noncoherent average of 100 realizations of the bus+rv image, even after Wiener filtering, shows no evidence of the detached cone. Even for the incoherent image (which is equivalent to averaging an infinite number of speckle realizations), shown in the right-most column, there is no evidence of the cones on the cylinder. These examples demonstrate a fundamental principal: to gather an image with a fixed array of detectors, we need a large number of detectors to arrive at an image with a large number of resolution elements across it. Hence with, say, 32 or even 64 detectors in a fixed pattern we can hope to reconstruct only fairly simple images. The bottom half of Figure 3-5 shows the 4-point object through the same small aperture; in this case we can discern the shape of this simple object with a reasonable number of speckle realizations.

If we allow the detectors to move and/or use aperture synthesis by observing the speckles as they flow past the detectors, then extended objects can be successfully imaged with fewer detectors, but with a much higher detector read-out rate.

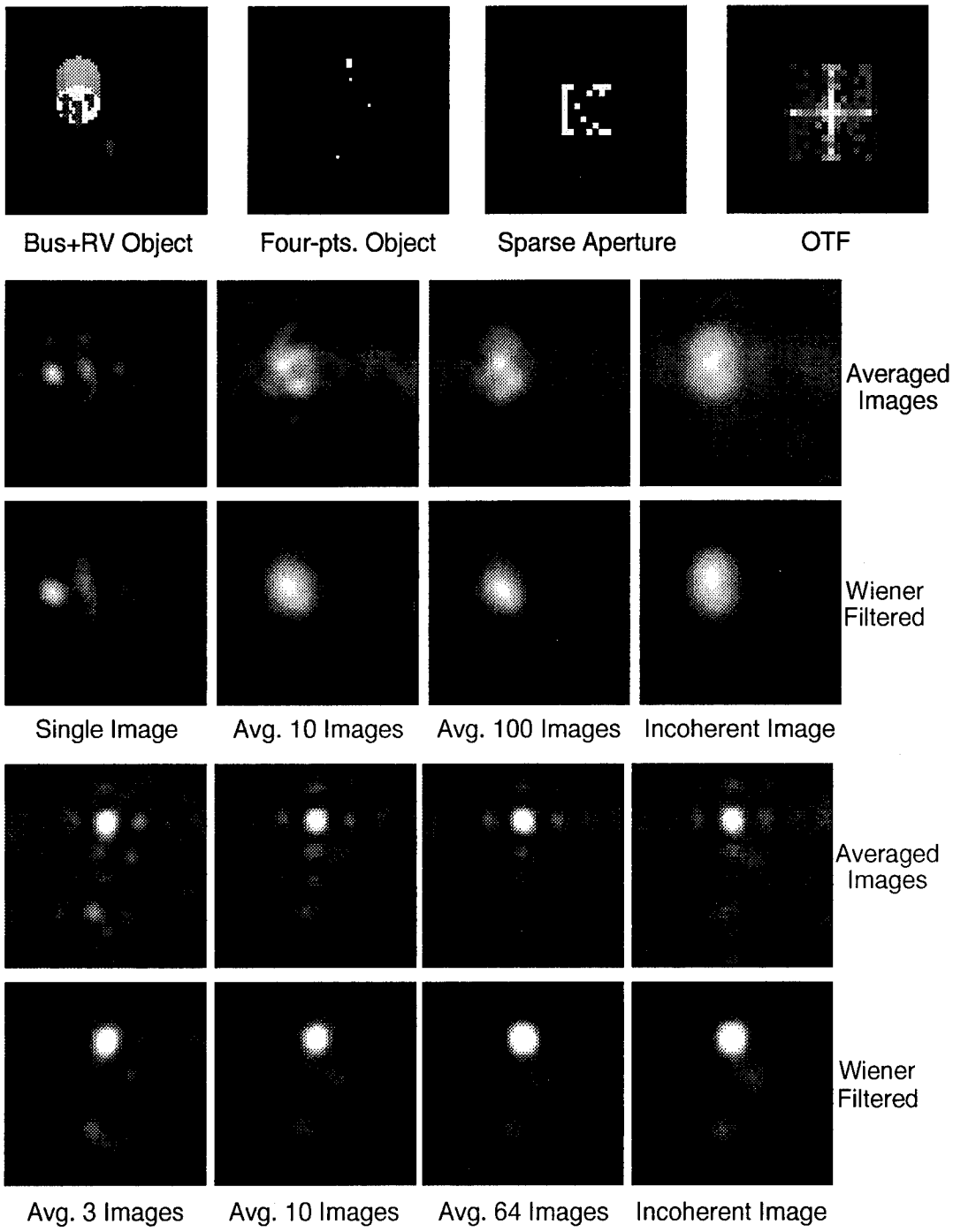

Figure 3-5. Imaging Through a 22-Element Detector Array;
Top row: Extended object ("Bus/RV"), simple object ("four points"), sparse aperture, OTF. Second row: noncoherent average of coherent images of Bus/RV object. Third row: Wiener filtered images of Bus/RV. Fourth row: average of images of four-points object. Fifth row: Wiener filtered images of four-points object.

3.2 IMAGING CORRELOGRAPHY

Some of the advantages of imaging correlography are that it allows the reconstruction of a fine-resolution image (a) despite atmospheric turbulence, misaligned array elements, and other sources of phase errors, and (b) with relatively inexpensive optical hardware and detectors. It computes the average autocovariance of multiple aperture-plane speckle intensity realizations to estimate the magnitude of the Fourier transform of the incoherent image and employs a phase retrieval algorithm to reconstruct the image. See Appendix A for more details. In this section we show the effect of a sparse aperture on imaging correlography.

An estimate of the Fourier magnitude of the 4-points object, determined from correlography using 100 speckle realizations through the 21-circle aperture (shown earlier), is shown on the left in Figure 3-6. The higher spatial frequencies are suppressed because of the fall-off in the OTF as seen in Figure 3-2. A Wiener-filtered version of that estimate, in which the suppressed spatial frequencies are enhanced, is shown in the second column of Figure 3-6. For comparison, the third column shows the true Fourier magnitude of the object. From this we can see that the Wiener-filtered estimate is somewhat depressed at the lower spatial frequencies, an effect we have not fully explained. The right-most column of the Figure shows an image reconstructed from the Fourier magnitude estimate (see Appendix A for an explanation). This reconstruction is a faithful representation of the ideal image, demonstrating that imaging correlography can work with sparse arrays of detectors.

Figure 3-7 shows the effect of the number of realizations on the quality of the reconstructed image. The top row shows the Fourier magnitudes (left-to-right): of the true object, estimated from one hundred speckle realizations, from twenty speckle realizations, and from five speckle realizations. The bottom row shows the corresponding images reconstructed by phase retrieval. For twenty or more speckle realizations the basic structure of the object is preserved whereas for five realizations the image is badly distorted.

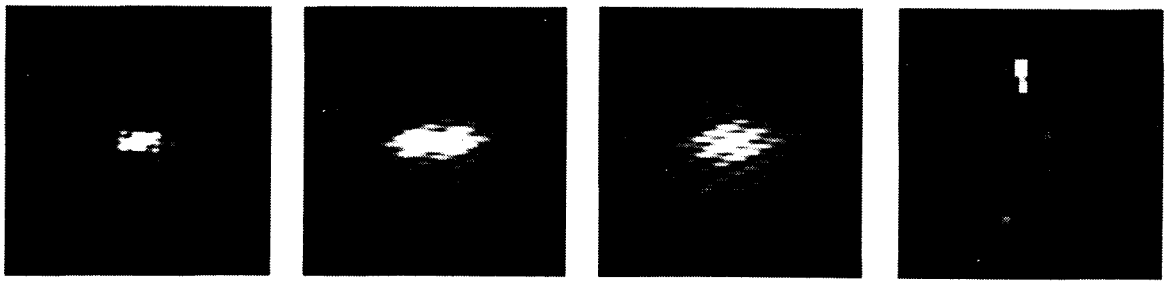

Fourier Magnitude from Correlography (100 speckle patt.)

Wiener Filtered Fourier Magnitude

Fourier Magnitude of Object

Reconstructed Image

Figure 3-6. Fourier Magnitude and Reconstructed Image from Correlography.

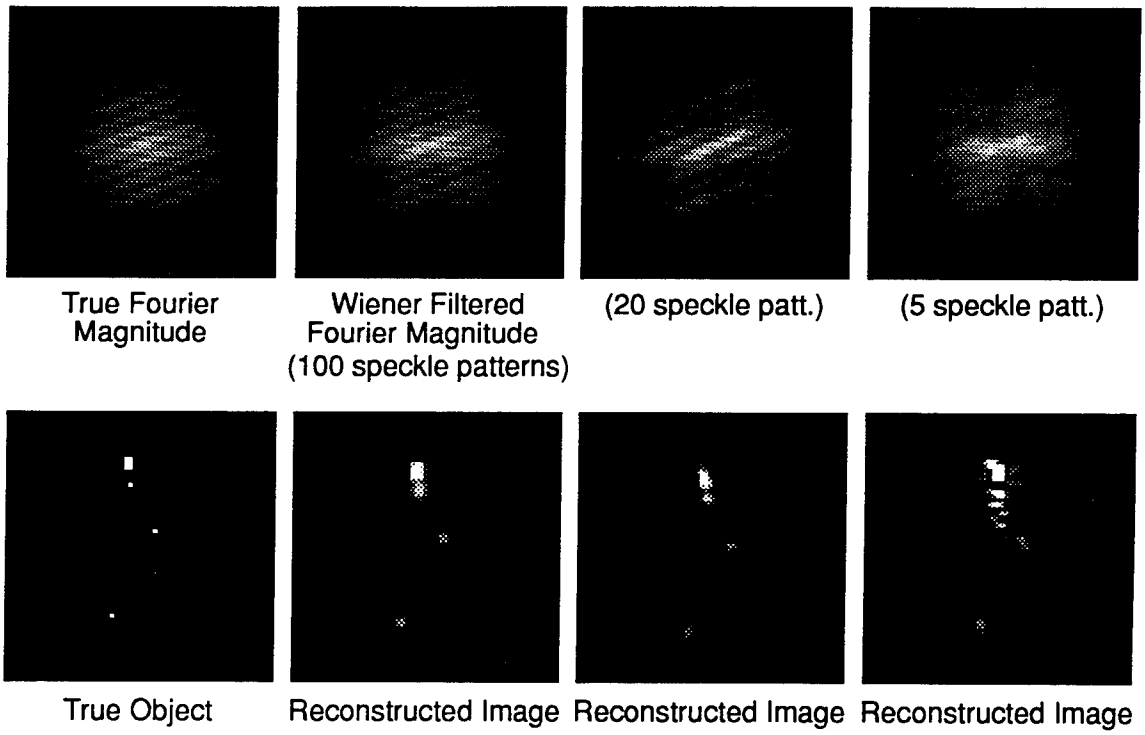

Figure 3-7. Image from Correlography for Different Numbers of Realizations.

As discussed in Appendix A, the signal-to-noise ratio for correlography is given by

$$\mathrm{SNR}(u,\ v) = \frac{\sqrt{N\ n_s\ S(u,\ v)}\ |\mu|^2}{\sqrt{3 + 14\ |\mu|^2 + 3\ |\mu|^4 + \frac{4(1 + 2\ |\mu|^2)}{M\ n_d} + \frac{1 + |\mu|^2}{M\ n_d^2}}} \qquad (3.2)$$

where n_d = the average number of photons per detector

M = the number of detectors (pixels) per aperture-plane speckle area

$M\ n_d$ = the average number of photons per speckle

N = the number of speckle realizations

n_s = the number of speckles within the area of the aperture

$\mu(u,\ v) = F_I(u,\ v)/F_I(0,\ 0)$, and

$F_I(u,\ v)$ = the Fourier transform of the underlying incoherent object

For the higher spatial frequencies where $|\mu|^2$ is small, the SNR of $|\mu|^2$ is proportional to N, to $|\mu|^2$, and to the square root of the area of the aperture (which is proportional to n_s). However, we have an additional proportionality factor of S(u, v), the OTF, which also depends on the aperture area and on the shape of the aperture pattern. For example, for a sparse nonredundant aperture in which each detector sees a different speckle, $n_s S(u,\ v) = 1$ for $(u,\ v) \neq (0,\ 0)$. However, for a sparse redundant aperture $n_s S(u,\ v)$ can be very large. In general, the number of independent Fourier components sampled, including their redundancy but ignoring the zero-frequency component, is $N_d(N_d - 1)/2$, where N_d is the number of detectors. Hence by adding just one more detector to a given number, N_d, we add $(N_d + 1)(N_d)/2 - N_d(N_d - 1)/2 = N_d$ additional measurements. The quadratic dependence of the number of Fourier measurements on the number of detectors strongly suggests using as many detectors as possible.

3.3 SIMULATION DETAILS

Some details of the simulation are as follows. We use the following notation.

$f_I(x)$ = incoherent object

$F_I(u)$ = FT of incoherent object

$|F_I(u)|^2$ = power spectrum of incoherent object

$c(x)$ = coherent impulse response (IPR)

$s(x)$ = point-spread function (PSF) = $|c(x)|^2$

$A(u)$ = aperture function = coherent transfer function (a binary mask)

$OTF(u)$ = optical transfer function = autocorrelation of $A(u)$

1. **Calculate c(x), s(x), OTF(u).**

   1.0 Make sure $A(u)$ is of width $\leq N/2$ embedded in an $N \times N$ array

   1.1 $c(x) = FT[A(u)]$

   [if you want to use $c(x)$ itself later, first shift $A(u)$ so its DC is in u.l. corner]

   1.2 $s(x) = |c(x)|^2$ [imaginary part = 0]

   1.3 $OTF_{unnormalized}(u) = FT^{-1}[s(x)]$ [Note: FT^{-1} includes $\times N^{-2}$ factor]

   1.4 $OTF(u) = OTF_{unnormalized}(u)/OTF_{unnormalized}(0)$

2. **Create an incoherent image, $g_I(x) = s(x) * f_I(x)$,** from $f_I(x)$.

   2.1 $f_{Ic}(x) = f_I(x)$, [imaginary part = 0]

   2.2 $F_I(u) = FT[f_{Ic}(x)]$

   2.3 $G_I(u) = F_I(u)\ OTF(u)$

   2.4 $s(x) * f_I(x) = FT^{-1}[G_I(u)]$

   2.5 Take real part of $s(x) * f_I(x)$ [imaginary part should << real part]

3. **Create a coherent image, $g_k(x)$,** from $f_I(x)$.

   3.1 The real and imaginary parts of $g_k(x)$ are chosen from a zero-mean Gaussian random variable with variance $(1/2)\ f_I(x)$. To do this,

      3.1.1 Form a uniform array of complex Gaussian random numbers (independent Gaussian r.n. for both real and imaginary parts) each having unity variance

      3.1.2 Multiply that array by $\sqrt{f_I(x)/2}$.

      (Note: then $E[|g_k(x)|^2] = 2f_I(x)/2 = f_I(x)$.)

   3.2 $FT[\bullet]$ [$\bullet$ = result from previous step]

   3.3 $\bullet \times A(u)$ [having DC of $A(u)$ in u.l. corner]

   3.4 $g_k(x) = FT^{-1}[\bullet]$

Get multiple realizations by changing the value of the seed in the random number generator that produced the Gaussian r.n.'s. To be able to reproduce results, always use a user-specified seed.

4. Wiener filter the averaged image.

Filtering an image g(x) by the filter function H(u) is accomplished by

4.1 $G(u) = FT[g(x)]$

4.2 $G_{filt}(u) = G(u)\, H(u)$

4.3 $g_{filt}(x) = FT^{-1}[G(u)]$

The Wiener-Helstrom filter is given by

$$H_{W\text{-}H}(u) = \frac{OTF_s^*(u)\, W_F(u)\, OTF_f(u)}{|OTF_s(u)|^2\, W_F(u) + W_N(u)} = \frac{OTF_s^*(u)\, OTF_f(u)}{|OTF_s(u)|^2 + W_N(u)/W_F(u)}$$
$$= \frac{OTF_s^*(u)\, OTF_f(u)}{|OTF_s(u)|^2 + \beta_n\, NSR(u)} \qquad (3.3)$$

where $OTF_s(u)$ is the OTF of the sparse aperture, $OTF_f(u)$ is the OTF of the filled aperture, $W_F(u) = |F_I(u)|^2$ is the power (or energy) spectrum of the object, $W_N(u)$ is the power spectrum of the noise, and $NSR(u) = W_N(u)/W_F(u)$ is the noise-to-signal ratio [1/SNR(u)], and β_n is a constant. We include the factor $OTF_f(u)$ to give the final image an aperture weighting closer to that of a normal filled aperture. Unfortunately, we do not usually know $W_F(u)$ and sometimes do not know $W_N(u)$. One approach is to replace NSR(u) with a constant, and adjust the constant to give the most pleasing image (trading off image smoothing with noise suppression for image sharpening with noise enhancement). Using a constant for NSR(u) usually enhances the noise at the highest spatial frequencies too much. Since many images have power spectra that can be approximated by a power law, and since noise power spectra are often a constant, a logical choice for NSR(u) would be $\alpha|u|^\gamma$, where α and γ are constants, γ controlling how fast the $W_F(u)$ falls off with u. Values of γ in the range of 0.5 to 4 are appropriate, with the smaller values appropriate for objects consisting of a very small number of points and larger values appropriate for very extended, low-contrast objects. This expression for NSR(u) must be modified so that it does not blow up near u = 0. We accomplished this by choosing

$$NSR(u) = \begin{cases} 1\ , \text{ for } |u| \le u_L \\ \alpha|u|^\gamma\ , \text{ for } |u| > u_L \end{cases}$$

where $\alpha|u_L|^\gamma = 1$, or $\alpha = 1/|u_L|^\gamma$. Here $|u|$ is the distance in pixels from the DC (i.e., if its coordinate relative to DC is (u_x, u_y), then $|u| = \sqrt{u_x^2 + u_y^2}$. Therefore by specifying u_L and γ, NSR(u) is specified. Examples of SNR(u) and NSR(u) are given in Figures 3-8 to 3-11.

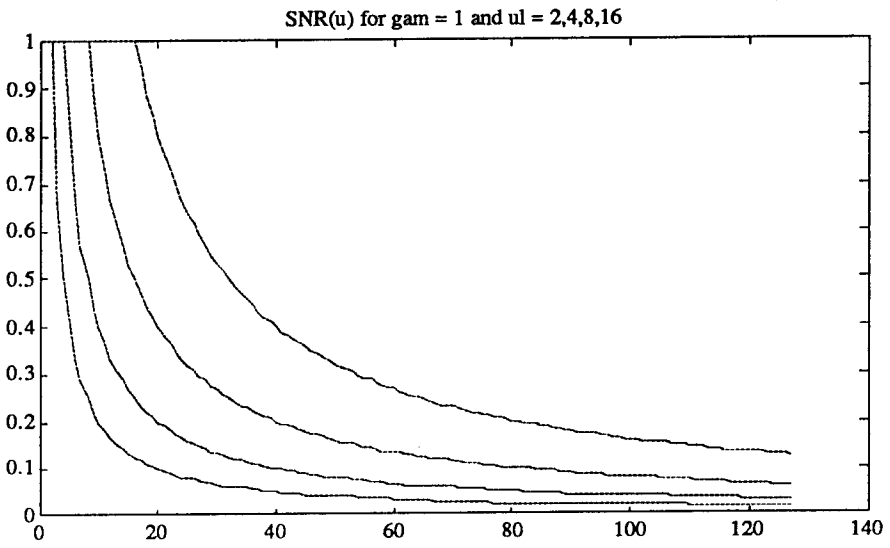

Figure 3-8. Model of Signal-to-Noise Ratio Versus Spatial Frequency. For 1/(frequency) spectrum and model parameter u_L = 2, 4, 8, and 16 pixels (left to right).

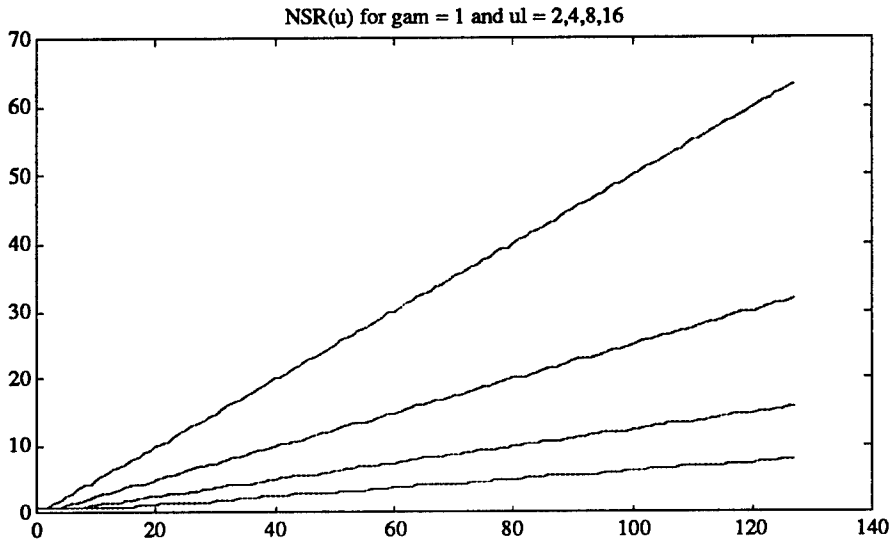

Figure 3-9. Model of Noise-to-Signal Ratio Versus Spatial Frequency. For 1/(frequency) spectrum and model parameter u_L = 2, 4, 8, and 16 pixels (left to right).

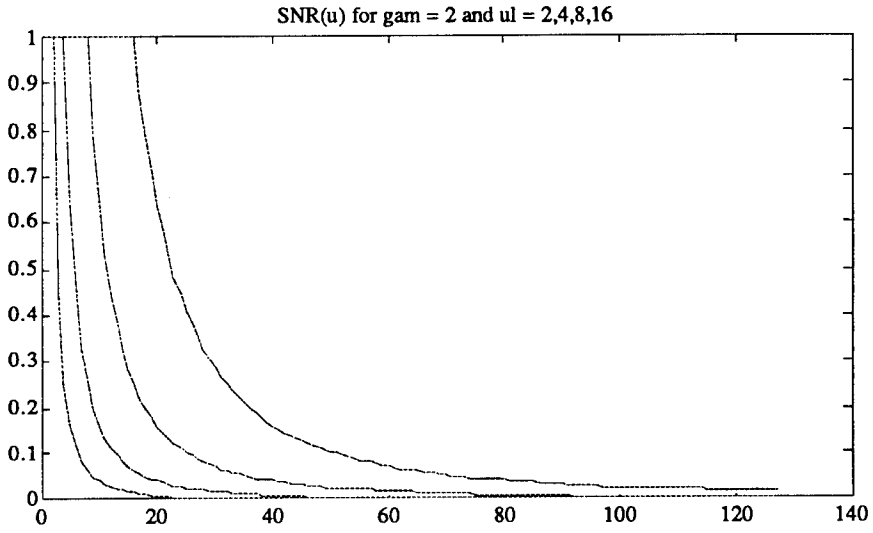

Figure 3-10. Model of Signal-to-Noise Ratio Versus Spatial Frequency. For 1/(frequency)^2 spectrum and model parameter u_L = 2, 4, 8, and 16 pixels (left to right).

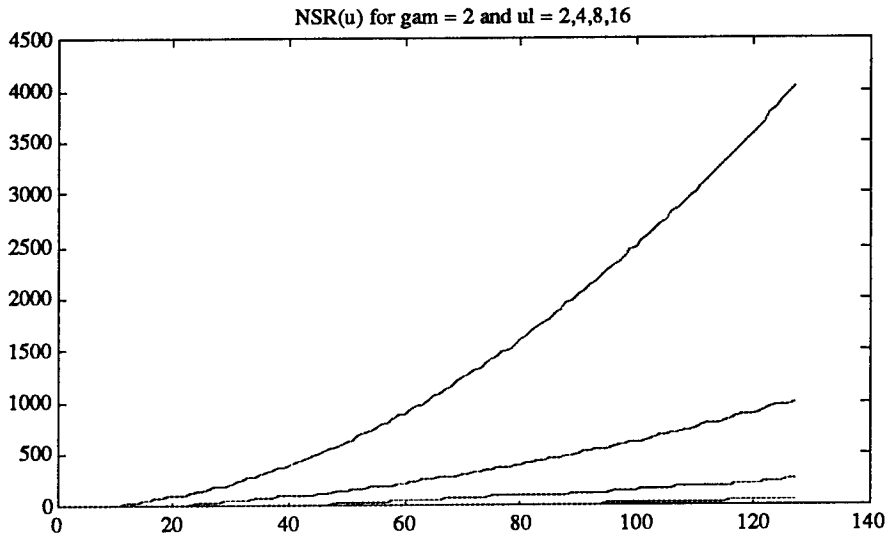

Figure 3-11. Model of Noise-to-Signal Ratio Versus Spatial Frequency. For 1/(frequency)^2 spectrum and model parameter u_L = 2, 4, 8, and 16 pixels (left to right).

As long as the OTF does not include aberrations, then OTF = OTF* is real-valued and nonnegative.

3.4 SECTION 3 REFERENCES

[3.1] P.S. Idell and A. Webster, "Resolution Limits for Coherent Optical Imaging: Signal-to-Noise Analysis in the Spatial-Frequency Domain," J. Opt. Soc. Am. A 9, 43-56 (1992).

[3.2] C.W. Helstrom, "Image Restoration by the Method of Least Squares," J. Opt. Soc. Am. 57, 297-303 (1967).

[3.3] P.D. Henshaw and N.R. Guivens, Jr., "Genetic Algorithms for Unconventional Imaging," in Inverse Optics III, Proc. SPIE 2241, 257-265 (April 1994).

4 PHASING OF SPARSE ARRAYS OF HETERODYNE RECEIVERS

4.1 INTRODUCTION

If we measure an optical field, scattered from a laser-illuminated object, with an array of heterodyne receivers [4.1], then we can reconstruct an image of the object by performing a suitable propagation transformation (typically a Fresnel or Fourier transform) in the computer [4.2]. However, if phase errors are present in the measurements, then a blurred image will result. Phase errors can be induced by many things, including atmospheric turbulence and path-length errors between the field from the object and the local oscillator within the receiver. Approaches to phasing the array without a beacon either require the array of heterodyne receivers to be on a filled regular grid [4.3, 4.4], or to have a special pattern or alternatively require a low-resolution image be available [4.5].

In this section we describe two new algorithms for phasing heterodyne arrays that work well for sparse distributed arrays (and should work for filled arrays as well), require no low-resolution image, and are relatively insensitive to noise. One is based on the iterative transform algorithm using a support constraint [4.6, 4.7] and the other on maximizing image sharpness [4.8, 4.9].

4.2 IMAGING MODEL

With the heterodyne receivers we measure the optical fields (ignoring measurement noise)

$$G_{dk}(u) = F_k(u)\ \exp[i\phi_e(u)]\ , \qquad (4.1)$$

for k = 1, ... , K, where F_k is the ideal complex field (without phase errors) for speckle realization k, ϕ_e is the phase error, and u is a 2-D coordinate (the pixel index) in the measurement plane. Note that we assume the phase error is the same for all K realizations. Different speckle realizations are obtained if the object rotates slightly or translates. If we estimate the phase error as $\phi(u)$, then our estimates of the optical fields are

$$G_k(u) = G_{dk}(u)\ \exp[-i\phi(u)] \tag{4.2}$$

our coherent images are

$$g_k(x) = \mathcal{F}^{-1}[G_k(u)] = N^{-2}\sum_u G_k(u)\ \exp(i2\pi u\cdot x/N)\ , \tag{4.3}$$

where u·x is a vector dot (inner) product, and our speckle-reduced averaged image is

$$g_I(x) = K^{-1}\sum_k |g_k(x)|^2\ , \tag{4.4}$$

where summation over k is for k = 1, ..., K.

Our goal is to estimate the image [and, equivalently $\phi_e(u)$ and the set of $F_k(u)$] from the set of $G_{dk}(u)$.

4.3 GENERALIZED ITERATIVE TRANSFORM ALGORITHM

Our first method to estimate the phase error is a generalization of the iterative transform algorithm [4.6]. It iterates back and forth between the image and Fourier domains, applying applicable constraints in each domain. Only here we are performing the iterations simultaneously on all K image realizations.

Our image-domain constraint is a support constraint. We have several ways to arrive at a support constraint.

We can compute the averaged autocorrelation function, and use our methods for estimating image supports from autocorrelation supports [4.10, 4.11]. Let

$$r_k(x) = \mathcal{F}^{-1}[|G_{dk}(u)|^2] \tag{4.5}$$

be the autocorrelation function of $g_{dk}(x)$. It is identical to the unaberrated autocorrelation since it depends only on the magnitude of $G_{dk}(u)$ and not on its phase. The averaged autocorrelation function is

$$r_I(x) = K^{-1}\sum_k |r_k(x)|^2\ . \tag{4.6}$$

Except for an impulse-response-like term at the origin, $r_I(x)$ will approach the ideal incoherent autocorrelation for large values of K. Note that this computation is essentially the same one we use for imaging laser correlography [4.12], as we are using only the intensity of the measured optical fields. It is important to use the averaged autocorrelation rather than the autocorrelation from an individual realization since any individual autocorrelation is speckled and will have multiple drop-outs over its entire area, making its support difficult to estimate [4.13].

We may also estimate the object support by using a low-resolution image. For example, the averaged image $g_I(x)$ (the current blurred estimate) can be a basis for a support constraint. Since during the middle of the reconstruction sequence $g_I(x)$ will be a poor approximation to the true image, we can only use it loosely as a support constraint. We should therefore convolve $g_I(x)$ with a smoothing function, w(x), giving $s(x) = g_I(x) * w(x)$, which also has the advantage of being a relatively smooth function. We can use this as a gray-level support constraint that emphasizes the image where the probability of it being non-zero is highest and suppresses it where the probability of it being nonzero is lower. We can also threshold this function to form a binary mask representing the support.

However we arrive at the support constraint, we will denote it by the function s(x), which is zero outside the support of the object. To apply the support constraint, we multiply each of the images by s(x):

$$g_{sk}(x) = s(x)\ g_k(x)\ . \tag{4.7}$$

After transforming these support-constrained images back to the Fourier domain we have the new Fourier estimates $G_{sk}(u) = \mathcal{F}[g_{sk}(x)]$.

Our Fourier constraint is the collection of magnitudes of the measured optical fields, $|G_{dk}(u)|$. The phases of $G_{dk}(u)$ are assumed to be corrupted. Furthermore, in the Fourier domain we also have the constraint that the phase error is common to all K realizations. That is, any phase changes we make should be the same for all K realizations. This constraint may be especially strong since it amounts to having K sets of equations to solve, but only one set of phases for which to solve. That is, compared

to the usual phase retrieval problem, this one may be much more heavily overdetermined, which may make it more robust. On the other hand, if the array data is very sparse, then we may be at a disadvantage compared with the more usual filled-aperture phase retrieval problems, since sparse arrays imply large sidelobes that would work against the effectiveness of a support constraint. The step of subtracting a common phase error is, in effect, using a Fourier magnitude constraint since the Fourier magnitude is unchanged for each k.

The new Fourier domain estimates, $G_{sk}(u)$, will differ from the previous estimates $G_k(u)$ both in magnitude and in phase. In the usual manner for an iterative transform algorithm, we substitute for the magnitudes of $G_{sk}(u)$ the measured magnitudes $|G_{dk}(u)|$. For the phases, we want to find the phase functions to change all the $G_k(u)$ by such that their phases most closely match those of the $G_{sk}(u)$, in order to exploit our knowledge that the phase error is the same for all realizations. One way to do this is a follows. Estimate the phase error by taking the average of the difference in phase between $G_{dk}(u)$ and $G_{sk}(u)$. At a given point (u), for some of the realizations $G_{sk}(u)$ will be nearer to zero, and therefore the phases for those realizations will be less reliable than for other realizations. Therefore we would do well to compute a weighted average of the phase difference. Such a weighted average would be

$$\phi(u) = \arg\{\sum_k G_{dk}(u)\, G_{sk}^*(u)\}\ , \tag{4.8}$$

where arg{X} is the phase of X.

In summary, one iteration of the generalized algorithm consists of the following steps:

(1) Calculate the Fourier estimates: $G_k(u) = G_{dk}(u) \exp[-i\phi(u)]$ (for k = 1 ... K).

(2) Inverse FFT them to compute the images $g_k(x)$.

(3) Apply the support constraint: $g_{sk}(x) = s(x)\, g_k(x)$.

(4) FFT to compute the $G_{sk}(u)$.

(5) Compute a new phase-error estimate: $\phi(u) = \arg\{\sum_k G_{dk}(u)\, G_{sk}^*(u)\}$.

For the initial iteration the phase error estimate is zero.

Steps (2) to (4) can also be performed by a direct convolution in the measurement plane:

$$G_{sk}(u) = G_k(u) * S(u) = \sum_{u_1} S(u_1)\, G_k(u - u_1)\,, \tag{4.9}$$

where $S(u) = \mathcal{F}[s(x)]$, which would be faster to compute for the case of sparse arrays. For filled arrays it is ordinarily fastest to compute a convolution using two FFT's and a multiply. However, for sparse arrays, for which $G_k(u)$ is zero except at P locations, and we only care about $G_{sk}(u)$ at those same P locations, then the direct convolution to compute $G_{sk}(u)$ will take only KP^2 complex multiplications [P products for each of P values of $G_{sk}(u)$], which will be more efficient than the FFT's. The FFT method, on the other hand, is very straightforward to compute, whereas the direct convolution is trickier if we are to compute it efficiently.

If we were to choose for the support constraint $s(x) = g_I(x) * w(x)$, then $S(u) = G_I(u)\, W(u)$, and

$$G_{sk}(u) = G_k(u) * [G_I(u)\ W(u)] = \sum_{u_1} G_I(u_1) W(u_1)\, G_k(u - u_1)\,. \tag{4.10}$$

Since w(x) would ordinarily be a real-valued symmetric kernel of width a small number of pixels (depending on how close we think we are to a solution), W(u) would be a smooth real-valued symmetric function that would play the role of a weighting function in the Fourier domain.

4.4 MAXIMIZING SHARPNESS

The second approach is to find the phase-error estimate $\phi(u)$ which maximize the sharpness,

$$S_1 = \sum_x [g_I(x)]^2 = \sum_x [\sum_k |g_k(x)|^2]^2\,, \tag{4.11}$$

of the image estimate.

We will accomplish the maximization using a standard gradient search technique that employs an analytic expression for the gradient, which we derive as follows:

$$\frac{\partial S_1}{\partial \phi(u)} = 2 \sum_x g_I(x) \sum_k \frac{\partial |g_k(x)|^2}{\partial \phi(u)} . \tag{4.12}$$

Using

$$\frac{\partial |g_k(x)|^2}{\partial \phi(u)} = -iN^{-2} g_k^*(x) G_k(u) \exp(i2\pi u \cdot x/N) + \text{c.c.} , \tag{4.13}$$

where c.c. denotes the complex conjugate of the term that precedes it, and rearranging the order of summations yields

$$\begin{aligned} \frac{\partial S_1}{\partial \phi(u)} &= 4N^{-2} \operatorname{Im}\Big\{ \sum_k G_k(u) \Big(\sum_x g_k(x)\, g_I(x) \exp(-i2\pi u \cdot x/N)\Big)^* \Big\} \\ &= 4N^{-2} \operatorname{Im}\Big\{ \sum_k G_k(u) \big(\mathcal{F}[g_k(x)\, g_I(x)]\big)^* \Big\} . \end{aligned} \tag{4.14}$$

S_1 would be maximized by a gradient search algorithm employing the expressions above for S_1 and its gradient.

Note that the product $g_k(x)\, g_I(x)$ resembles constraining the support of $g_k(x)$ to fit within the support of $g_I(x)$. Hence this algorithm is somewhat related to the iterative transform algorithm and other phase-retrieval gradient-search algorithms we have employed. We give a more detailed analysis of this point later.

If we are dealing with sparse apertures, $g_I(x)$ will have large sidelobes, and we may wish to filter it first to undo the severe weighting due to the optical transfer function. Let a filtered version of $g_I(x)$ be

$$\begin{aligned} g_{IW}(x) &= \mathcal{F}^{-1}\{G_{IW}(u)\} = \mathcal{F}^{-1}\{W(u)\, \mathcal{F}[g_I(x)]\} \\ &= N^{-2} \sum_{u'} W(u') \exp(i2\pi u' \cdot x/N) \sum_{x'} g_I(x') \exp(-i2\pi u' \cdot x'/N) , \end{aligned} \tag{4.15}$$

where W(u) is a filter function, a good choice for which would be a Wiener-Helstrom filter. W(u) will be centro-symmetric, making $g_{IW}(u)$ real-valued, but not necessarily nonnegative. Then our new sharpness metric is

$$S_{1W} = \sum_x [g_{IW}(x)]^2 . \tag{4.16}$$

Similar to the approach above, we take the derivative of S_{1W} with respect to $\phi(u)$, reverse the order of the (four) summations, and, using the fact that W(u) is Hermitian, we obtain

$$\begin{aligned} \frac{\partial S_{1W}}{\partial \phi(u)} &= 4N^{-2}\ \mathrm{Im}\{ \sum_k G_k(u)\ (\mathcal{F}\{g_k(x)\ \mathcal{F}^{-1}[G_{IW}W]\})^* \} \\ &= 4N^{-2}\ \mathrm{Im}\{ \sum_k G_k(u)\ (G_k(u) * [G_I W^2])^* \} , \end{aligned} \tag{4.17}$$

where $G_{IW}(u) = W(u)\ \mathcal{F}\ [g_I(x)]$, making $G_{IW}(u)W(u) = W^2(u)\ \mathcal{F}\ [g_I(x)]$. This expression is the same as that for S_1 given above, except that $g_I(x)$ is replaced by $\mathcal{F}^{-1}[G_{IW}W] = g_{IW}(x) * \mathcal{F}^{-1}[W] = g_I(x) * \mathcal{F}^{-1}[W^2]$, where * denotes convolution. S_{1W} reduces to S_1 if W(u) = 1 everywhere.

The major burden of computing S_1 is the K FFT's needed to compute the $g_k(x)$'s. The major computational burden of computing the gradient of S_1 with respect to $\phi(u)$ is the 2K FFT's needed to compute $g_k(x)$ and $\mathcal{F}[g_I(x)\ g_k(x)]$.

The primary burden of computing S_{1W} is (2K + 2) FFT's, which is only slightly greater than that of computing S_1.

4.5 COMPARISON WITH MAXIMIZING SHARPNESS

In this section we show that the error-reduction [4.6] version of our generalized iterative transform algorithm is similar in effect to a steepest-descent gradient search to maximize sharpness with a fixed step size. (However, we in practice use a more powerful gradient search algorithm, such as conjugate-gradient, and we can use a more powerful version of the iterative transform algorithm as well, such as hybrid input-output [4.6]).

In the section above we derived a gradient of a sharpness merit function, given as

$$\frac{\partial S_{1W}}{\partial \phi(u)} = 4N^{-2}\ \mathrm{Im}\{\sum_k G_k(u)\ (\mathcal{F}\{g_k(x)\ \mathcal{F}^{-1}[G_I W^2]\})^*\}\ , \tag{4.18}$$

for the weighted-G_I case, where $G_I(u)$ is replaced by $G_{IW}(u) = G_I(u)W(u)$. The unweighted case would be the same with $W(u) = 1$ everywhere. This can be rewritten

$$\frac{\partial S_{1W}}{\partial \phi(u)} = 4N^{-2}\ \mathrm{Im}\{\sum_k G_k(u)\ (G_k(x) * [G_I W^2])^*\}\ . \tag{4.19}$$

Let

$$G_{tk}(u) = G_k(u) * [G_I W^2]\ . \tag{4.20}$$

Note that $G_{tk}(u)$ is very similar to $G_{sk}(u)$ — it is identical if $W(u)$ is a binary function. We have

$$\frac{\partial S_{1W}}{\partial \phi(u)} = 4N^{-2}\ \mathrm{Im}\{\sum_k G_k(u)\ G_{tk}^*(u)\}\ . \tag{4.21}$$

For small values δ, $\mathrm{Im}\{|A|\ \exp[i\delta(u)]\} \approx |A|\ \delta(u)$, and by definition $\arg\{|A|\ \exp[i\delta(u)]\} = \delta(u)$, or $\mathrm{Im}\{|A|\ \exp[i\delta(u)]\} \approx |A|\ \arg\{|A|\ \exp[i\delta(u)]\}$. Therefore in the equation above, the gradient with respect to the phase error estimate is proportional to the average phase difference between $G_k(u)$ and $G_{tk}(u)$. Since we want to maximize the sharpness (climb up the hill) we want the phase-error estimate, $\phi(u)$, to go in the direction of this gradient. So if the phase moves in that direction by a step size, b, then the new phase error estimate will be

$$\begin{aligned} \phi_{new}(u) &\approx \phi_{old}(u) + b\ \arg\{\sum_k G_k(u)\ G_{tk}^*(u)\} \\ &\approx \phi_{old}(u) + b\ \arg\{\sum_k G_{dk}(u)\ \exp[-i\phi_{old}(u)]\ G_{tk}^*(u)\}\ . \end{aligned} \tag{4.22}$$

where we have included the magnitude of the sum in the step size b. If we happen to choose a step size b=1, then we have, for maximizing sharpness,

$$\phi_{new}(u) \approx \arg\{\sum_k G_{dk}(u)\ G_{tk}^*(u)\}\ . \tag{4.23}$$

Comparing this with our new phase error estimate for the iterative transform algorithm (Step 5), we see that it is nearly the same, since $G_{tk}(u) \approx G_{sk}(u)$. That is, our iterative transform algorithm using a low-resolution image as a support constraint is approximately the same as a sharpness-maximization steepest-descent gradient search method with a particular fixed step size.

Which of the two algorithms is better is difficult to predict. We know from previous work that the error-reduction (ER) version of the iterative transform algorithm (ITA) is equivalent to a fixed-step steepest descent algorithm, and it is inferior to both the hybrid input-output (HIO) version of the ITA and to a conjugate-gradient algorithm. The algorithm we described above is an ER-like algorithm. Therefore the sharpness-maximizing gradient-search algorithm (which would employ a sophisticated gradient search) would be superior to the iterative algorithm given above both because the type of gradient search is superior and because it is not restricted to a specific step size. On the other hand, a HIO version of this algorithm might work well. An HIO version of the iterative algorithm would be to replace Step 3, $g_{sk}(x) = s(x)\ g_k(x)$, with

$$\begin{aligned} g_{sk}(x) &= s(x)\ g_k(x) + [1 - s(x)]\ [g_{skold}(x) - \beta\ g_k(x)] \\ &= s(x)\ [(1 + \beta)\ g_k(x) - g_{skold}(x)] + g_{skold}(x) - \beta\ g_k(x) \end{aligned} \qquad (4.24)$$

where $g_{skold}(x)$ is $g_{sk}(x)$ from the previous iteration and we assume that s(x) is binary (1 or 0), although this might also work for s(x) defined continuously between 0 and 1. A Fourier-domain convolution version of the HIO algorithm, which would speed the algorithm for sparse arrays, would be as follows (replacing Steps 2 to 4):

$$G_{sk}(u) = S(u) * [(1 + \beta)\ G_k(u) - G_{skold}(u)] + G_{skold}(u) - \beta\ G_k(u)\ . \qquad (4.25)$$

4.6 IMAGE RECONSTRUCTION EXAMPLE

Figure 4-1 shows a computer simulation example of phase-error correction using the generalized iterative-transform algorithm for a distributed array of heterodyne receivers. At the top is the 4-points object, consisting of a block of 2×3 pixels and three separated points, embedded in a 64×64 array. The sparse aperture we used for this experiment has 54 subapertures within a 16×16 area, which is shown in the upper left,

magnified by a factor of two (only the central 32×32 pixels in its 64×64 array are shown). This sub-aperture pattern was designed using a genetic-based algorithm by P. Henshaw [4.14]. The average of ten ideal diffraction-limited speckled images through this aperture has significant sidelobe artifacts making it difficult to discern the four points, as seen in the next part of the figure. The Wiener-Helstrom [4.15] filtered version of the averaged image (on the right) has few of these artifacts, and from it one can easily discern the major parts of the image. The bottom row in the figure shows the results when we added, to the Fourier transform, random phase errors that were uniformly distributed Gaussian random numbers with standard deviation 2π radians. The raw aberrated image (on the left) has no information content, whereas the image corrected by the iterative transform is almost identical to the ideal diffraction-limited image. The reconstructed image was shifted in position from the ideal, as is usually the case for phase-correction algorithms. (All images in this example are the average of ten speckled images.) We obtained comparable results using the image sharpness algorithm. The algorithms usually produced images with better quality as the number of realizations increases. It was unreliable when using only one to four realizations. Tests showed that the algorithm is not very sensitive to noise.

4.7 CONCLUSIONS

We have derived two new algorithms for phasing an array of heterodyne receivers, and have demonstrated that they can work well for sparse distributed arrays, require a modest number of speckle realizations, and are robust in the presence of measurement noise.

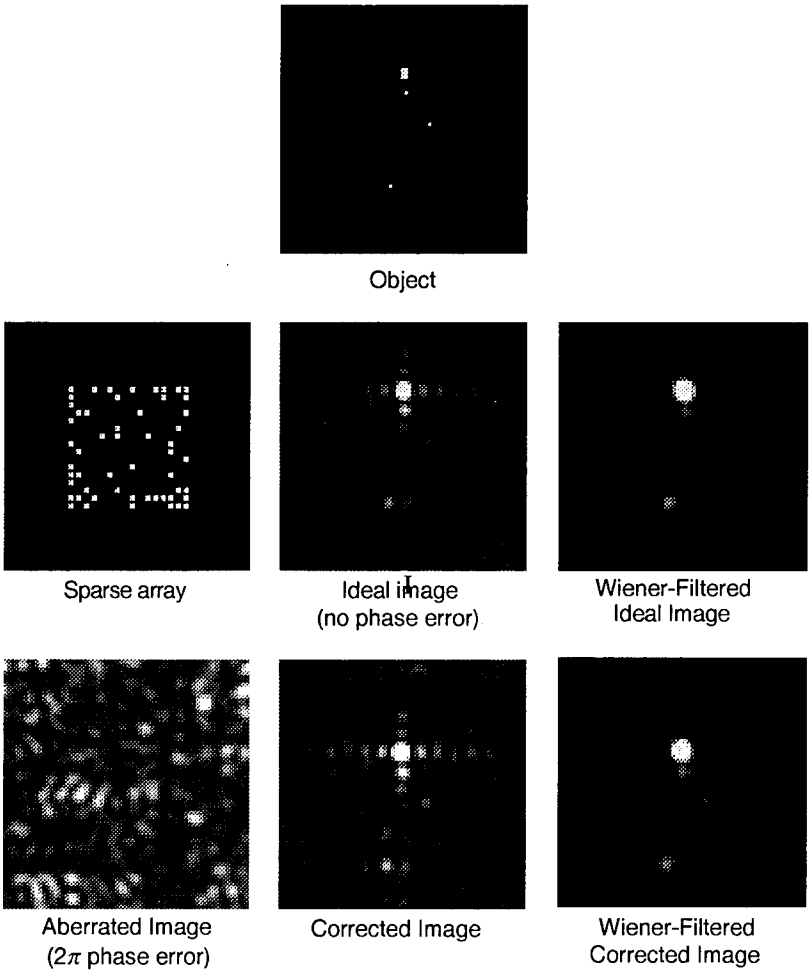

Figure 4-1. Computer Simulation of Sparse Heterodyne Array Phasing by the Iterative Transform Algorithm.

4.8 SECTION 4 REFERENCES

[4.1] G.W. Kamerman, "Laser Radar," in *Active Electro-Optical Systems*, C.S. Fox, Ed., Vol. 6 of *The Infrared & Electro-optical Systems Handbook*, (ERIM, Ann Arbor, 1993), Chapter 1.

[4.2] J.R. Fienup, "Unconventional Imaging Systems: Image Formation from Non-imaged Laser Speckle Patterns," in *Emerging Systems and Technologies*, S.R. Robinson, Ed., Vol. 8 of *The Infrared & Electro-optical Systems Handbook*, (ERIM, Ann Arbor, 1993), Chapter 1.5, pp.92-109.

[4.3] J.R. Fienup, J.N. Cederquist, J.C. Marron, T.J. Schulz and J.H. Seldin, "Heterodyne Array Phasing by Digital Shearing Laser Interferometry," in *IRIS Specialty Group on Active Systems Meeting Digest*, 16-18 October 1990.

[4.4] J.N. Cederquist, J.R. Fienup, J.C. Marron, T.J. Schulz and J.H. Seldin, "Digital Shearing Laser Interferometry for Heterodyne Array Phasing," in *Laser Radar VI*, R.J. Becherer, ed., Proc. SPIE 1416 -43 (1991).

[4.5] S.E. Clark and L.F. Desandre, "High Resolution Image Reconstruction from Sparse Random Arrays," in *Signal Recovery and Synthesis IV*, 1992 Technical Digest Series Vol. 11 (Optical Society of America), April 14-15, 1992, New Orleans. LA, pp. 75-77.

[4.6] J.R. Fienup, "Phase Retrieval Algorithms: A Comparison," *Appl. Opt.* 21, 2758-2769 (1982).

[4.7] J.R. Fienup, "Reconstruction of a Complex-Valued Object from the Modulus of Its Fourier Transform Using a Support Constraint," *J. Opt. Soc. Am. A* 4, 118-123 (1987).

[4.8] R.A. Muller and A. Buffington, "Real-Time Correction of Atmospherically Degraded Telescope Images through Image Sharpening," *J. Opt. Soc. Am.* 64, 1200-1210 (1974).

[4.9] R.G. Paxman and J.C. Marron, "Aberration Correction of Speckled Imagery with an Image-Sharpness Criterion," in *Statistical Optics*, Proc. SPIE 976 -05, San Diego, CA, August 1988.

[4.10] J.R. Fienup, T.R. Crimmins, and W. Holsztynski, "Reconstruction of the Support of an Object from the Support of Its Autocorrelation," *J. Opt. Soc. Am.* 72, 610-624 (1982).

[4.11] T.R. Crimmins, J.R. Fienup and B.J. Thelen, "Improved Bounds on Object Support from Autocorrelation Support and Application to Phase Retrieval," *J. Opt. Soc. Am. A* 7, 3-13 (1990).

[4.12] P.S. Idell, J.R. Fienup and R.S. Goodman, "Image Synthesis from Nonimaged Laser Speckle Patterns," Opt. Lett. 12, 858-860 (1987).

[4.13] J.R. Fienup, "Phase Retrieval Imaging Problems," Ch. 28 in J.W. Goodman, ed., International Trends in Optics (Academic Press, 1991), pp. 407-422.

[4.14] P.D. Henshaw, "Genetic Algorithms for Unconventional Imaging," in *Inverse Optics III*, M.A. Fiddy, ed., Proc. SPIE 2242-34 (April 1994).

[4.15] C.W. Helstrom, "Image Restoration by the Method of Least Squares," *J. Opt. Soc. Am.* 57, 297-303 (1967).

(blank page)

5 TURBULENCE ISSUES FOR LASER-IMAGING EXPERIMENTS

5.1 INTRODUCTION

Atmospheric turbulence plays an important role in the design of laser-imaging experiments. Such experiments could include the investigation of heterodyne methods, quasi-heterodyne methods, and direct-detection methods. Phase aberrations caused by atmospheric turbulence add to receiver misalignments in heterodyne detection to cause a total phase error that can cause severe blurring of the imagery. In addition, anisoplanatic effects (phase errors being different for different points in the object) are not accommodated by any of these methods, in their current formulation. It is natural to consider horizontal-path geometries in order to simplify the experimental design. However, induced phase aberrations, anisoplanatism, and scintillation are much more severe with horizontal geometries than with vertical geometries. A candidate experiment design might set the range at $R = 1\,\mathrm{km}$, the sparse aperture diameter at $D = 25\,\mathrm{cm}$ and the wavelength at $\lambda = 1.0\text{e-}6\,\mathrm{m}$ to get a target resolution of

$$\Delta x = R\lambda/D \tag{5.1}$$

$$= 3.9\,\mathrm{mm}. \tag{5.2}$$

Phase-aberration strength (quantified with a correlation diameter) and anisoplanatism (quantified with an isoplanatic patch diameter) should be evaluated with respect to the aperture diameter and extent of the target (Δx times number of resolution elements across target), respectively. In this Section we investigate the expected phase-aberration strength and anisoplanatism for a horizontal-path geometry at ranges of 1 and 10 km.

5.2 TURBULENCE STRENGTH

The index structure parameter, C_n^2, is a measure of turbulence strength that depends upon altitude, time of day, meteorological conditions, and season. Induced

Table 5-1. Correlation Diameter, r_o, as a Function of C_n^2 and Range, R.

C_n^2 \ R	r_o	
	1 km	10 km
10^{-15}	33.3 cm	8.36 cm
10^{-14}	8.36 cm	2.10 cm
10^{-13}	2.10 cm	0.53 cm
10^{-12}	0.53 cm	0.13 cm

phase aberrations, anisoplanatism, and scintillation derive from path integrals involving C_n^2, under the Kolmogorov turbulence model. Horizontal imaging implies that C_n^2 is independent of position on path, simplifying computation of these path integrals. Note however that C_n^2 is highly variable, so that several computations must be made. Figure 5-1 shows the variability in C_n^2 at an altitude of 9 m over the diurnal cycle under cloudless desert conditions. This figure suggests that C_n^2 could be expected to vary over 4 orders of magnitude at a given site. Fried has defined the correlation diameter (or seeing parameter) to be [5.1]

$$r_o \equiv \left\{ \left(\frac{2.91}{6.88}\right) \left(\frac{2\pi}{\lambda}\right)^2 \int_0^R C_n^2(z)[1-(z/R)]^{5/3}\, dz \right\}^{-3/5} . \qquad (5.3)$$

Using this expression we computed the correlation diameter as a function of C_n^2 and range. These values are given in Table 5-1. We see from Table 5-1 that only the 1 km range and the most favorable turbulence conditions yield a correlation diameter that is comparable to the hypothetical aperture diameter, $D = 25$ cm.

5.3 ANISOPLANATISM

Another important factor to consider in an experiment design is the amount of anisoplanatism induced by the long-path turbulence. The origin of the anisoplanatism is the fact that radiation emanating from differing points in the field of view encounter different volumes of turbulence in route to the aperture. Fried has derived an expression for anisoplanatism-induced mean-square phase error in an adaptively

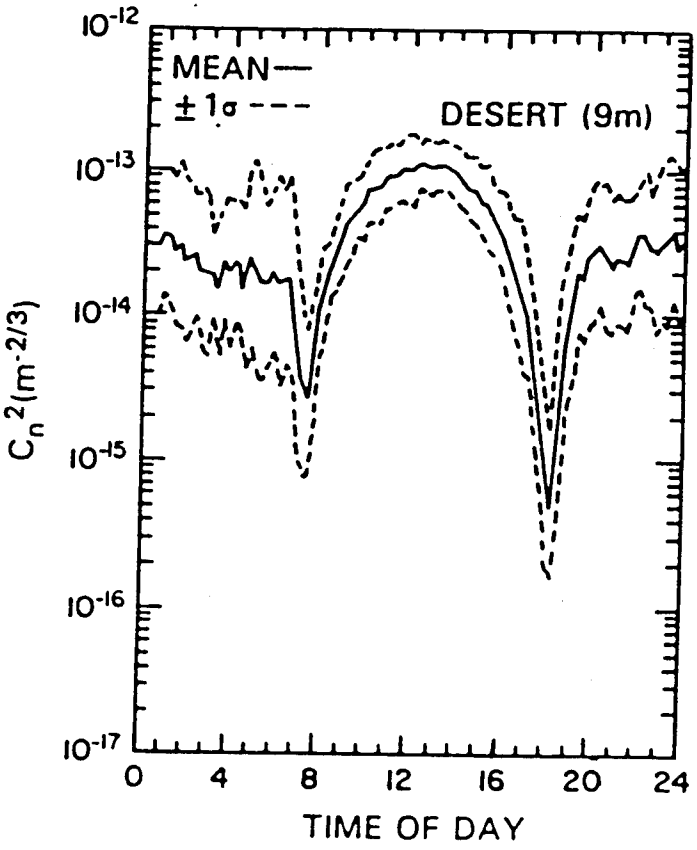

Figure 5-1. C_n^2 Measurements. Measurements are taken at an altitude of 9 m under cloudless desert conditions over the diurnal cycle. Statistical variability in the form of ± 1 standard deviation is also given (from Infrared and Electro-Optical Systems Handbook, SPIE Optical Engineering Press, Bellingham WA, Vol. 2, p. 202).

corrected system [5.2]:

$$S(\boldsymbol{r},\boldsymbol{\alpha}) = 2.905\left(\frac{2\pi}{\lambda}\right)^2\int_0^R C_n^2(z)\left(\{r[1-(z/R)]\}^{5/3}+(\alpha z)^{5/3}\right.$$
$$-\frac{1}{2}|\{r[1-(z/R)]\}^2+2r\alpha zc[1-(z/R)]+(\alpha z)^2|^{5/6}$$
$$\left.-\frac{1}{2}|\{r[1-(z/R)]\}^2-2r\alpha zc[1-(z/R)]+(\alpha z)^2|^{5/6}\right)dz \quad (5.4)$$

where $\boldsymbol{\alpha}$ is a field-angle vector relative to the beacon and

$$c \equiv \boldsymbol{r}\cdot\boldsymbol{\alpha}/(r\alpha)\,. \quad (5.5)$$

The function $S(\boldsymbol{r},\boldsymbol{\alpha})$ is interpreted as the mean-square phase error between points in the pupil separated by $\boldsymbol{r}$ for a point in the field-of-view at field-angle $\boldsymbol{\alpha}$. Equation (5.4) applies to a system with ideal phase correction for waves generated at the beacon. The RMS phase difference at a separation of 25 cm in the pupil as a function of field position and at a range $R = 1$ km with $c = 1$ is given in Figure 5-2.

The isoplanatic angle has been defined by Fried to be

$$\alpha_o \equiv \left[2.91\left(\frac{2\pi}{\lambda}\right)^2\int_0^R C_n^2(z)z^{5/3}\,dz\right]^{-3/5}. \quad (5.6)$$

Notice that this expression resembles the definition of r_o (Eq. (5.3)), although there is a different scale factor and the path integral emphasizes turbulence near the target. In order to interpret the meaning of the anisoplanatic angle it is useful to consider the anisoplanatism induced mean-square phase error in two important limiting cases.

$$\lim_{r/\alpha\to\infty} S(\boldsymbol{r},\boldsymbol{\alpha}) = \left(\frac{\alpha}{\alpha_o}\right)^{5/3} \quad (5.7)$$

$$\lim_{r/\alpha\to 0} S(\boldsymbol{r},\boldsymbol{\alpha}) = 6.88\left(\frac{r}{r_o}\right)^{5/3} \quad (5.8)$$

We define the isoplanatic patch diameter as

$$p_o \equiv R\alpha_o\,. \quad (5.9)$$

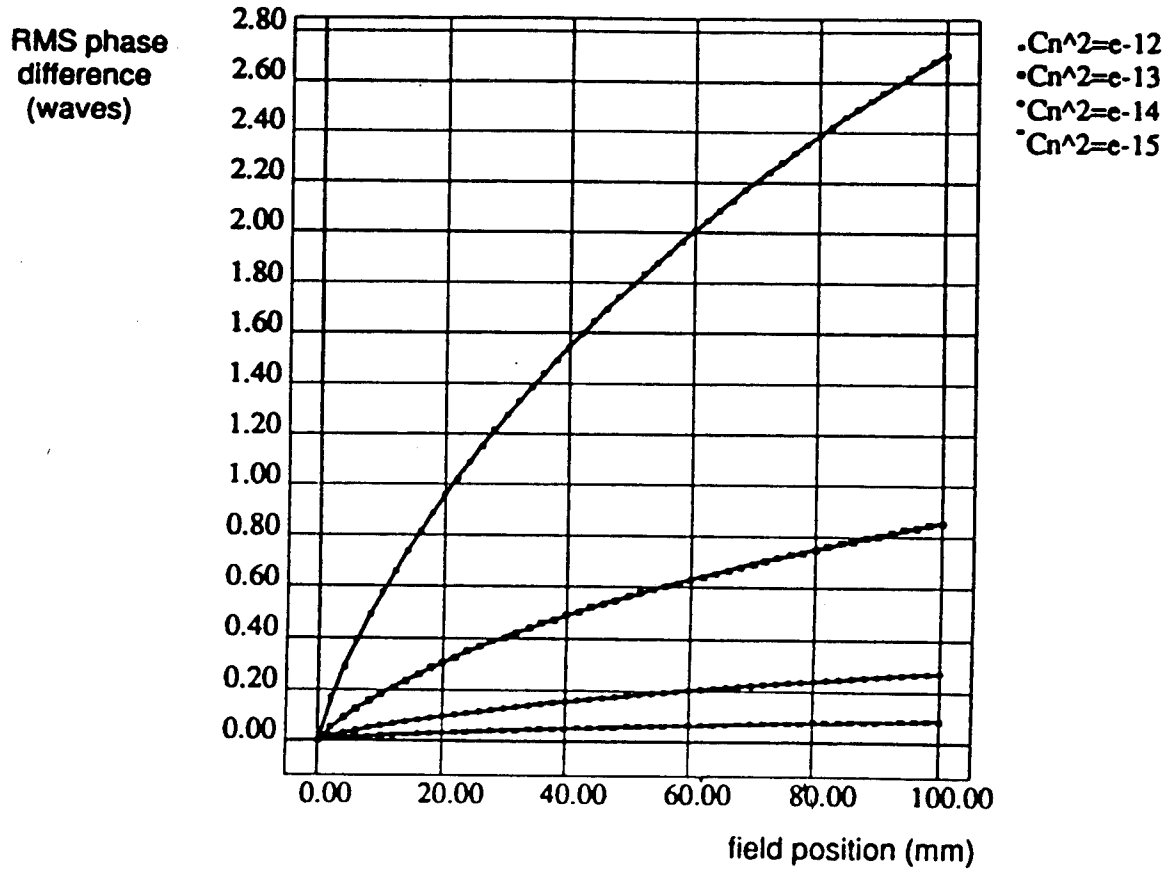

Figure 5-2. RMS Phase Difference as a Function of Field Position. The phase difference is measured at a separation of 25 cm in the pupil. The range is $R = 1\,\mathrm{km}$ and $c = 1$.

Table 5-2. Isoplanatic Patch Diameter as a Function of Turbulence Strength, C_n^2, and Range, R.

	ρ_o	
C_n^2 \ R	1 km	10 km
10^{-15}	105.0 mm	26.3 mm
10^{-14}	26.3 mm	6.6 mm
10^{-13}	6.6 mm	1.7 mm
10^{-12}	1.7 mm	0.4 mm

Table 5-2 gives the isoplanatic patch diameter as a function of turbulence strength, C_n^2, and range, R. Table 5-2 suggests that for an experiment design with $R = 1\,\text{km}$ and very good turbulence conditions, we might expect to have between 7 (for $C_n^2 = 10^{-14}$) and 27 (for $C_n^2 = 10^{-15}$) resolution elements across an isoplanatic patch when the resolution is $\Delta x = 3.9\,\text{mm}$.

Consider the case in which we are not troubled by phase aberrations in the pupil but are only constrained to have the field of view confined to an isoplanatic patch. This would be the case when we have an adaptive optics system or when we have full confidence in a phase-correction algorithm. In this case we have

$$N\Delta x = p_o \tag{5.10}$$

$$= R\alpha_o\,. \tag{5.11}$$

Using Eq. (5.1) to substitute for Δx and solving for D we get

$$D = \frac{NR\lambda}{(R\alpha_o)}\,. \tag{5.12}$$

Let $N = 31$, $R = 1\,\text{km}$, and $\lambda = 1.0\,\mu\text{m}$. Table 5-3 gives the required aperture diameter values as a function of turbulence strength, C_n^2.

Table 5-3. Aperture Diameter as a Function of Turbulence Strength, C_n^2. Fixed parameters include $N = 31$, $R = 1\,\text{km}$, and $\lambda = 1.0\,\mu\text{m}$.

C_n^2	$R\alpha_o$	D
10^{-15}	105.0 mm	0.32 m
10^{-14}	26.3 mm	1.22 m
10^{-13}	6.6 mm	4.85 m
10^{-12}	1.7 mm	18.82 m

5.4 RECOMMENDATIONS AND OUTSTANDING ISSUES

These calculations have been made using plausible values for C_n^2. We recommend that on-site measurements be made of C_n^2 to help guide the experiment design. We also recommend that the simulation experiments be performed to investigate the effects of anisoplanatism on phase correction algorithms. If necessary, these algorithms could be developed to explicitly accommodate anisoplanatic effects. It appears that a horizontal range of no more than 1 km should be used for initial experiments. Data may need to be collected at the diurnal minima for C_n^2 and a temperature structure constant, C_t^2, may need to be monitored to optimize data-collection times.

There are several outstanding issues needing further study. The effects of boundary-layer turbulence (due to proximity to the ground) have not been considered. On-site measurements should be designed to statistically characterize C_n^2 as a function of time of day and height off of the ground. In addition, effects of scintillation also need to be characterized for any experimental design. Finally, an extended-path experiment might be designed with a vertical geometry. Although such a geometry significantly reduces problematic atmospheric effects, target design becomes more challenging.

5.5 SECTION 5 REFERENCES

[5.1] D.L. Fried, "Optical Resolution Through a Randomly Inhomogeneous Medium for Very Long and Very Short Exposures," J. Opt. Soc. Am. 56, 1372-1379 (1966).

[5.2] D.L. Fried, "Anisoplanatism in Adaptive Optics," J. Opt. Soc. Am. 72, 52-61 (1982).

6 NEW 3-D IMAGING MODALITY USING AN OPACITY CONSTRAINT

6.1 INTRODUCTION

In this section we present a candidate three-dimensional imaging concept that we refer to as *Phase Retrieval with an Opacity Constraint for LAser IMaging* (*PROCLAIM*). Three-dimensional imaging significantly enhances target identification over two-dimensional imaging modes.

6.2 IMAGING CONCEPT

Marron has demonstrated that three-dimensional imaging can be accomplished by sequentially illuminating an object with different laser frequencies and measuring the far-field speckle pattern for each of the illuminating frequencies [6.1]. In-phase and quadrature measurements provide field quantities for the laser-speckle patterns. Properly formatted, these data form a three-dimensional Fourier-volume (or aperture) representation of the illuminated object. A simple three-dimensional DFT can be performed to get a three-dimensional image of the object. This three-dimensional lensless imaging concept is referred to as Holographic Laser Radar (HLR).

The collection of HLR data could be considerably simplified if, instead of collecting field measurements for the speckle images, we collect intensity measurements. Intensity measurements are straightforward and eliminate the need for interference with a reference beam with precision alignment, tracking, and phase stability. A speckle-intensity data set would provide three-dimensional Fourier-magnitude information or, equivalently, the three-dimensional object autocorrelation. In order to recover a literal three-dimensional image, a phase-retrieval algorithm is required. Therefore, this proposed imaging concept trades complexity and cost in hardware for increased computing.

Phase retrieval requires some type of *a priori* information about the object. Two-dimensional complex-valued objects have been recovered using phase retrieval with a

support constraint [6.2], although this is a challenging problem. It is well known that the uniqueness properties of two-dimensional phase retrieval are much better than for the one-dimensional problem [6.3]. We conjecture that three-dimensional phase retrieval with a support constraint is better conditioned than its two-dimensional counterpart.

An alternative constraint that has great promise in the three-dimensional imaging case is an *opacity* constraint. An opaque object is an object that exhibits only surface scattering and no volume scattering (over volumes that extend beyond the desired range resolution). The reflectivity function for an opaque object is confined to a two-dimensional manifold embedded in a three-dimensional space. An opacity constraint has been used to perform superresolution [6.4].

The opacity constraint is a special type of support constraint. It is a "quality of support" constraint – the actual location of the support is not given, although the object is known to be confined to a two-dimensional manifold. This constraint promises to be very powerful since it greatly reduces the class of feasible objects from which to choose an estimate. Moreover, there are many imaging applications in which the objects will be known with confidence to be opaque. For example, ballistic missiles certainly qualify as opaque objects. Most objects in our everyday experience satisfy the opaque condition. The constraint is invalid for objects with distributed volume scatterers such as translucent or fog-like objects.

The use of an opacity constraint in conjunction with frequency-diverse pupil-plane speckle measurements to reconstruct a three-dimensional object constitutes the unconventional imaging concept that we refer to as Phase Retrieval with an Opacity Constraint for LAser IMaging (PROCLAIM). In the following sections we consider various embodiments of this imaging concept.

6.3 SYNTHETIC-APERTURE DESIGN

Consider a missile or a space object that is moving with some trajectory overhead. When it is illuminated with a laser, the reflected light will form a speckle pattern on

the ground. The diameter of a speckle on the ground is given by

$$\rho = \frac{R\lambda}{D_{obj}}, \tag{6.1}$$

where R is the target range, λ is the wavelength, and D_{obj} is the object diameter in the cross-range direction. We wish to detect this speckle pattern. The spatial sampling interval required to satisfy the Nyquist criterion is

$$\Delta x \leq \rho/2 \tag{6.2}$$

$$\leq \frac{R\lambda}{2D_{obj}}. \tag{6.3}$$

For an object with $D_{obj} = 5\,\text{m}$ at $R = 100\,\text{km}$ and $\lambda = 1\,\mu\text{m}$ we have $\Delta x \leq 1\,\text{cm}$.

One way to collect an angle-angle speckle pattern at a particular frequency is to use a filled array, as depicted in Figure 6-1(a). Filled arrays can be expensive. An alternative is to recognize that the object will be rotating and the speckle will be translating on the ground, which suggests the use of a synthetic aperture. The speckle will translate on the ground at a speed given by

$$v_s = 2R\omega \tag{6.4}$$

where ω is the angular velocity of the target. If a linear array of detectors is oriented perpendicular to the direction of speckle motion, an angle-angle speckle pattern can be built up synthetically in time, as depicted in Figure 6-1(b). The hardware requirements for such a system are dramatically reduced over a filled array of comparable diameter.

6.4 SERIAL-FREQUENCY ILLUMINATION

The goal is to acquire a separate array of speckle measurements for each of several illuminating laser frequencies. This can be accomplished by modulating the illuminating laser output with an acousto-optic (AO) device to serially step through a sequence of desired frequencies. A time-frequency representation of a step-frequency

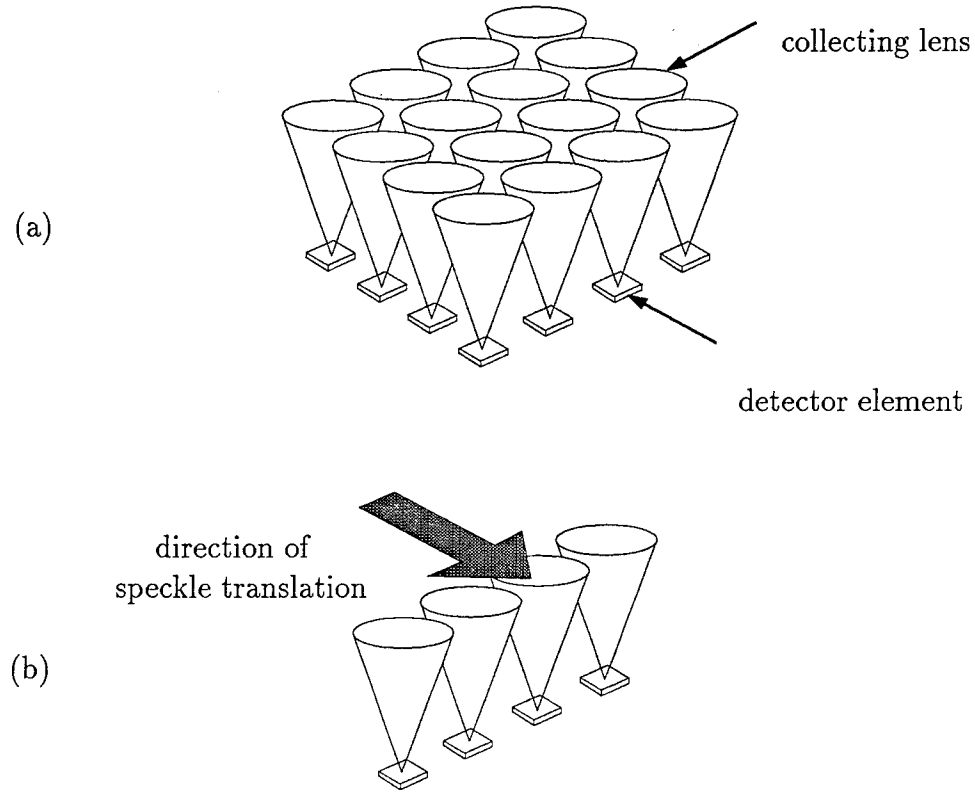

Figure 6-1. Detection Geometry. (a) Filled-aperture array, (b) synthetic-aperture array.

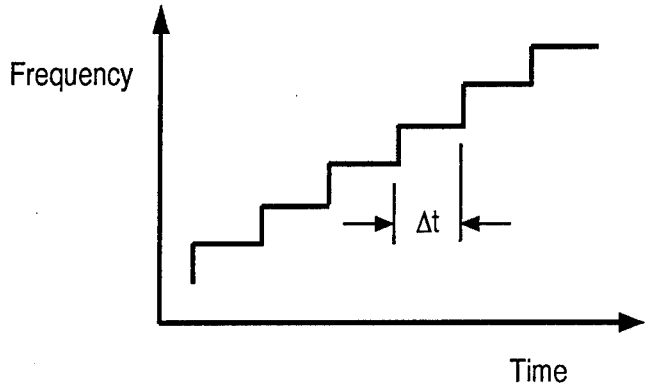

Figure 6-2: Time-Frequency Representation of Step-Frequency Illumination Pulse.

illumination is shown in Figure 6-2. We require that the duration of a frequency step, Δt, be long enough so that returns from near and far points in the target can simultaneously have the same frequency.

$$\Delta t > 2Z_{obj}/c \,, \tag{6.5}$$

where Z_{obj} is the depth of the object and c is the speed of light. The duration of a step-frequency sequence will be

$$T = N\Delta t \,, \tag{6.6}$$

where N is the number of individual illuminating frequencies or, equivalently, the number of range bins desired in the three-dimensional image.

There is also an upper limit on the speed of the speckle translating at the detector array that can be tolerated. We require that a speckle move no more than a half of a speckle diameter during an entire step-frequency sequence. This requirement insures that the angular sampling in the synthetic-aperture direction will meet the Nyquist criterion for each of the frequencies:

$$v_s < \frac{\rho}{2N\Delta t} \,. \tag{6.7}$$

Substituting in expressions for v_s, ρ, and Δt, we find that this criterion restricts the angular velocity of the target that can be tolerated:

$$\omega < \frac{\lambda c}{8ND_{obj}Z_{obj}} . \tag{6.8}$$

It is worth noting that this expression is independent of range. As a sample calculation, consider an object for which $D_{obj} = 5\,\mathrm{m}$ and $Z_{obj} = 2\,\mathrm{m}$. Suppose also that we desire $N = 10$ and that we are imaging at $\lambda = 1\,\mu\mathrm{m}$. The maximum angular velocity that can be tolerated for such an object is found to be $\omega < .375$ radians/second. This sample calculation suggests that the requirement on object angular frequency is not particularly restrictive and that there are likely to be many objects that can be imaged with serial-frequency illumination. Objects that rotate at a rate faster than the criterion prescribed by Eq. (6.8) will give data that is undersampled (aliased) in one angular dimension. It is possible that the opacity constraint could perform interpolation in addition to phase retrieval to accommodate such undersampled data. Of course this conjecture would need to be validated and quantified. Note that restrictions on target angular velocities are relaxed as the array is built up in the synthetic-aperture direction. In the case of a completely filled array, only a single step-frequency illumination sequence is needed to collect the entire data set and the three-dimensional Fourier volume will be mildly skewed in the illumination-frequency dimension for targets that rotate particularly fast.

6.5 PARALLEL-FREQUENCY ILLUMINATION

In serial-frequency illumination, speckle measurements for differing frequencies are differentiated by temporal multiplexing. An alternative is to illuminate the object with all frequencies simultaneously and use a dispersive element prior to detection to differentiate frequencies. This mode of operation is referred to as parallel-frequency illumination and is depicted in Figure 6-3.

Parallel-frequency illumination is attractive since an AO device is not required to produce a precisely timed illuminating waveform, as is true in the serial-frequency illumination mode. Multiple frequencies can be created by operating the laser at

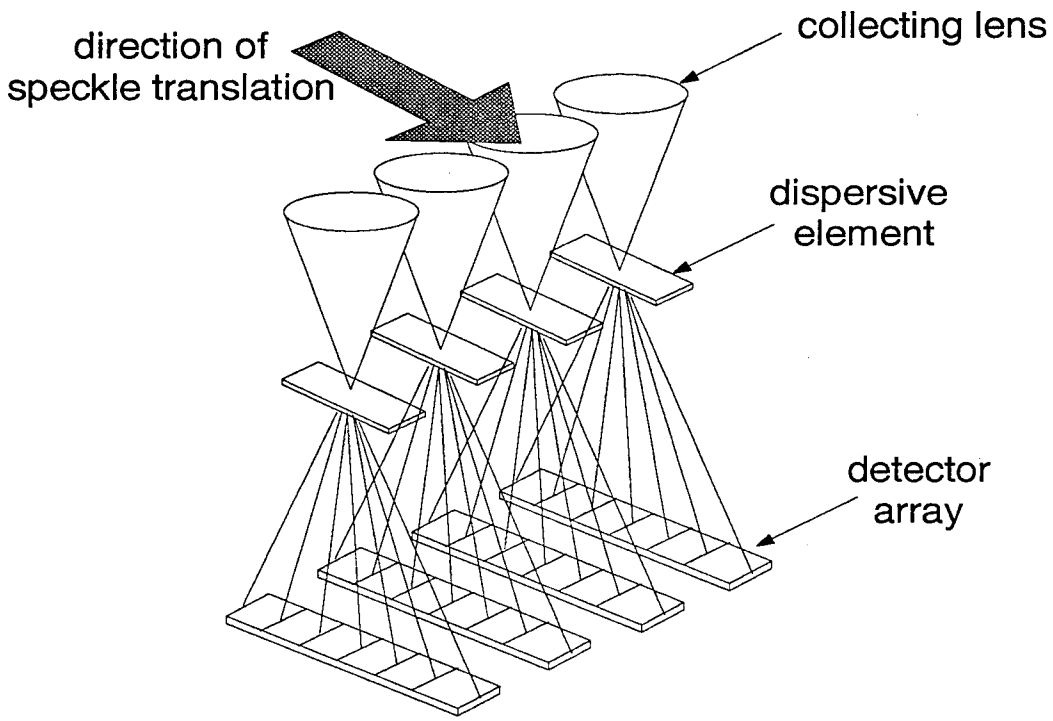

Figure 6-3. Parallel-Frequency Illumination Mode

multiple longitudinal modes simultaneously. On the other hand, the resolving power needed to differentiate frequencies with a dispersive element is demanding. The frequency interval required to meet the Nyquist criterion is given by [6.1]

$$\Delta\nu \leq \frac{c}{2Z_{obj}} . \tag{6.9}$$

The resolving power of a dispersive element is defined as

$$\mathcal{R} \equiv \frac{\bar{\lambda}}{\Delta\lambda} \tag{6.10}$$

$$\approx \frac{\bar{\nu}}{\Delta\nu} , \tag{6.11}$$

where $\bar{\lambda}$ and $\bar{\nu}$ represent the center wavelength and frequency, respectively. Substituting in the expression for the maximum frequency interval (Eq. (6.9)), we have

$$\mathcal{R} \geq \frac{2Z_{obj}\bar{\nu}}{c} \tag{6.12}$$

$$\geq \frac{2Z_{obj}}{\bar{\lambda}} . \tag{6.13}$$

For $Z_{obj} = 2\,\mathrm{m}$ and operating at $\lambda = 1\,\mu\mathrm{m}$ we have $\Delta\nu \leq 75\,\mathrm{MHz}$ and $\mathcal{R} \geq 4 \times 10^6$. The resolving power of a grating is given by [6.5]

$$\mathcal{R}_g = mM , \tag{6.14}$$

where m is the order and M is the number of grating lines. A blazed grating design could be used to direct the light to a higher order – – perhaps the 5th order. In order to achieve a resolving power of $\mathcal{R} = 4 \times 10^6$ we require $M = 8 \times 10^5$ in a diffraction-limited grating. With a grating-line separation of $1\,\mu\mathrm{m}$, such a grating would be 80 cm in length. Such an element would be impractical and motivates us to investigate other possibilities. Some spectrograph designs rely upon multiple passes through a single grating, which may make a grating design more feasible; but this would require additional study. For a proof-of-principal experiment using small objects on a 1 km test range, a grating would be feasible. For example, if we are making a target of depth 2 cm, then the grating would have to be just 8 mm in length.

A Fabry-Perot interferometer can be used to achieve resolving powers that are significantly larger than gratings. The expression for the resolving power for a Fabry-Perot interferometer is given by [6.6]

$$\mathcal{R}_{fp} = \frac{2\pi n d r}{\lambda(1-r^2)}, \tag{6.15}$$

where n is the index of refraction of the material between reflective surfaces, d is the separation between reflective surfaces, and r is the reflectivity. As an example, if we select $r = .95$, $n = 1$, and $d = .1\,\mathrm{m}$, the resolving power is found to be $\mathcal{R}_{fp} = 6.1 \times 10^6$, which is sufficient for the previous example. Unfortunately, the Fabry-Perot interferometer only passes one narrow spectral band at a time and rejects the remaining light. This inefficiency would not be acceptable for our imaging application in which photons are a highly valued commodity. One can imagine a scheme in which the rejected light is repeatedly recycled through the Fabry-Perot interferometer at slightly different angles on each pass to yield a high-efficiency system. Such a device would take further study.

The differentiation of frequencies can also be accomplished with heterodyne detection. In this mode of operation it is natural to try to detect both Fourier modulus and phase information. If the phase information is corrupted due to instabilities in the local oscillator or mechanical instabilities in the optical distribution of the local-oscillator signal to each detector in the array, then a phasing algorithm (see Section 4) will be needed. Opacity can also help the phasing algorithm.

6.6 CONCLUSIONS

Various embodiments of three-dimensional imaging with frequency-diverse speckle have been described. The serial-frequency illumination imaging mode offers a simple hardware design and appears to be valid for a significant range of objects of interest. This mode relies heavily upon an opacity constraint to accomplish phase retrieval. In the parallel-frequency illumination imaging mode, a practical dispersive element with sufficient resolving power and high efficiency has not been identified for the case of large objects. Opacity can also play a role with phasing algorithms when heterodyne

detection is employed. In any case, opacity promises to play a role in post-detection processing of the data for phase retrieval, bandwidth extrapolation, or interpolation.

Appendix C is a reprint of a publication showing the first successful reconstructions of a 3-D image from computer-simulated data using the PROCLAIM technique.

6.7 SECTION 6 REFERENCES

[6.1] J.C. Marron and K.S. Schroeder, "Three-Dimensional Lensless Imaging Using Laser Frequency Diversity," Appl. Opt. 31, 255-262 (1992).

[6.2] J.N. Cederquist, J.R. Fienup, J.C. Marron, and R.G. Paxman, "Phase Retrieval from Experimental Far-Field Speckle Data," Opt. Lett. 13, 619-621 (1988).

[6.3] J.C. Dainty and J.R. Fienup, "Phase Retrieval and Image Reconstruction for Astronomy," in Image Recovery: Theory and Application, H. Stark, ed. (Academic Press, New York, 1987).

[6.4] R.G. Paxman, "Superresolution with an Opacity Constraint," *Topical Meeting on Signal Recovery and Synthesis III*, Technical Digest Series 15, (Optical Society of America, Washington DC, 1989), PD1, North Falmouth, Cape Cod, MA, June 1989.

[6.5] W.J. Smith, *Modern Optical Engineering* (McGraw-Hill, New York, 1966).

[6.6] E. Hecht and A. Zajac, *Optics* (Addison-Wesley, Reading, MA, 1976).

7 LABORATORY DEMONSTRATION OF QUASI-HETERODYNE IMAGING

We conducted a laboratory experiment to demonstrate quasi-heterodyne imaging and correction of phase errors. The general approach was to record pupil plane complex optical field data by using a detector array. We also introduced quadratic phase errors by imparting defocus to the reference beam. We obtained multiple realizations of the pupil plane field by rotating the target slightly.

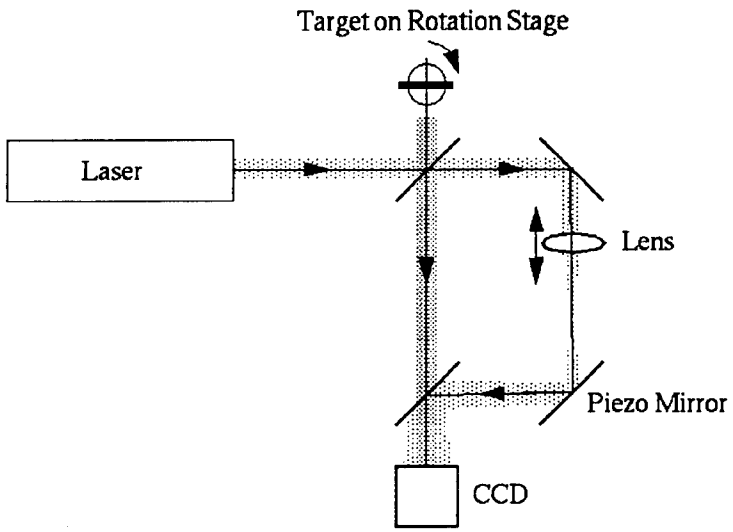

Figure 7-1. Experimental Setup Used for Laboratory Data Collection.

7.1 LABORATORY DATA COLLECTION

The diagram for the experimental setup is shown in Fig. 7-1. Light from an argon laser is collimated and separated into object and reference beams. The object beam illuminates a target which consists of cutout pieces of retro-reflective tape mounted on glass. The target occupies an area that is roughly 2 cm x 2 cm. Light reflected by the

target passes back through a beamsplitter and then, without imaging optics, to a CCD detector array. The reference beam of light travels through the beam splitter and to a lens that creates a point source that is initially at the same distance from the CCD array as the object, and is located to coincide with the center of the target. Light from this reference beam then propagates to a mirror that is mounted on a piezo-electric transducer. Longitudinal motion of the transducer is used to change the phase of the reference beam. The reference beam then propagates through a beamsplitter to the detector array that records the interference pattern of the object and reference beams.

The data recording procedure consists of recording four interferograms for each realization of the pupil plane field. These four interferograms are separated in phase by 90°, which we accomplish by motion of the piezo mirror. In this manner we can record the complex values of the optical field [7.1]. To obtain independent realizations of the pupil-plane field, we rotate the object is rotated so that new speckles occupy the CCD array.

For the initial set of data, we recorded a series of 64 independent realizations of the pupil-plane field. These frames of data are initially stored on a personal computer and are then passed to a network of workstation computers for processing.

7.2 IMAGE RECONSTRUCTION

From a set of four interferograms we compute the complex values of the optical field in the aperture (CCD) plane. Then by Fourier transformation we compute a complex-valued image. Figure 7-2 shows a noncoherent average of ten of the image realizations when no phase error was introduced.

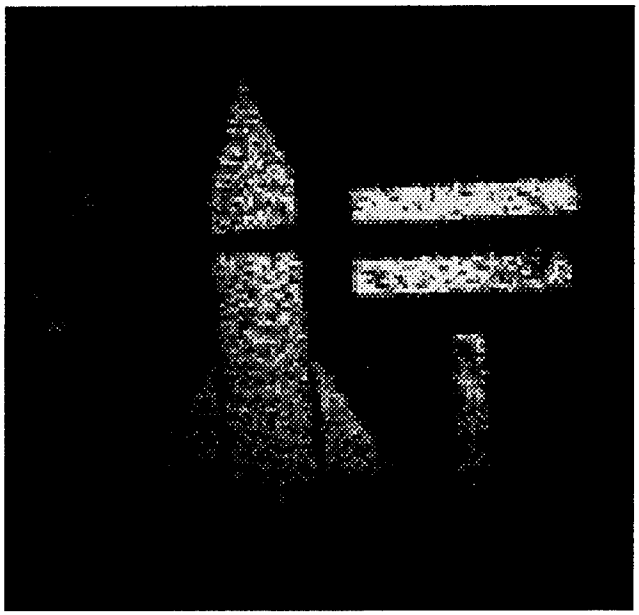

Figure 7-2. Image from Quasi-Heterodyne Laboratory Experiment. The average of the intensities of ten reconstructed images is show.

7.3 SECTION 7 REFERENCES

[7.1] J. C. Marron and K.S. Schroeder "Three-Dimensional Lensless Imaging using Laser Frequency Diversity," Appl. Opt. 31, 255-262 (1992).

(blank page)

8 DETERMINISTIC SPARSE ARRAY DESIGN

As discussed in Section 3, given a large enough number of speckle realizations, we can reconstruct a diffraction-limited incoherent (speckle-free) image of a laser-illuminated target. But to do so from a sparse aperture, we must design the pattern of subapertures so that the autocorrelation function of the aperture fills optical transfer function (OTF) space. If there are gaps in OTF space, then we cannot recover those missing spatial frequencies by Wiener filtering. At the same time, to minimize cost we may wish to use the least number of subapertures possible. Hence we have the problem of finding a pattern with the minimum number of subapertures whose autocorrelation forms a filled pattern. In this section we describe two such patterns, one of which, the "arrow," fills a square OTF and the second of which, the "box + 2," fills a square OTF with two-fold redundancy. Unlike other subaperture pattern designs, they are completely deterministic and are immediately scalable to any array size. We wish to define the patterns on square array because that matches the format of the image formation/reconstruction processing we perform in the computer.

Before showing the more efficient arrow pattern, we consider the pattern shown in Figure 8-1, which has the shape of the letter "U" turned on its side. (Rotating the pattern by 90° gives another pattern that also fills OTF space, so the pattern that looks like an upright "U" has the same properties.) For a subaperture pattern defined on a square grid with L positions on a side, it produces a filled autocorrelation of size $(2L - 1) \times (2L - 1)$ using $(3L - 2)$ subapertures. For the example shown in Figure 8-1, for a subaperture pattern with $L = 8$, it forms a square autocorrelation having $(2L - 1) = 15$ points on a side from $(3L - 2) = 22$ subapertures.

Figure 8-2 shows an example of the arrow array, which is the most efficient array we have found to date. The arrow array is defined on a square grid, which has the first row filled, the first column filled, and the diagonal between them filled, except for the (2, 2) point, which is missing. (The array can also be rotated by 90°.) It yields a filled autocorrelation of size $(2L - 1) \times (2L - 1)$ using only $(3L - 3)$ subapertures, one less than the U array. For the example shown in Figure 8-2, it forms a square autocorrelation of $(2L - 1) = 15$ points on a side from only $(3L - 3) = 21$ subapertures.

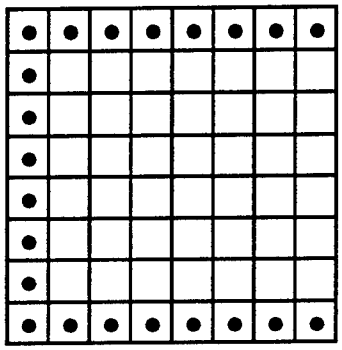

Figure 8-1. U Array Pattern.

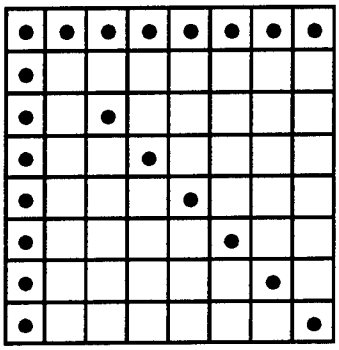

Figure 8-2. Arrow Array Pattern.

Table 8-1 compares the number of subapertures in the U and arrow patterns with those designed by a genetic algorithm [8.1]. Of the five cases given in Figure 4 of [8.1], the U array ties the genetic algorithm in two cases and beats it in one. The arrow array ties the genetic algorithm in two cases and beats it in three.

Table 8-1. Number of Subapertures to Fill (2L–1)x(2L–1) Autocorrelation Space.

Array Size (L)	Autocorr. Size (2L–1)	Genetic	U	Arrow
4	7	9	10	9
6	11	16	16	**15**
7	13	19	19	**18**
8	15	21	22	21
16	31	54	**46**	**45**

Figure 8-3, taken from Reference [8.1] shows graphically that the Arrow array significantly outperforms the computer-designed arrays for large array sizes.

Depending on the desired effect, other pattern design problems can be defined. For example, what pattern with the minimum number of subapertures yields an OTF with two-fold redundancy? This would give twice the signal-to-noise ratio as a pattern simply filling OTF space. We designed the "box + 2" pattern, an example of which is shown in Figure 8-4. It yields a filled, doubly redundant autocorrelation of size $(2L - 1) \times (2L - 1)$ using only $(4L - 2)$ subapertures. For the example shown, $L = 9$,

(2L – 1) = 17, from only (4L – 2) = 34 subapertures, compared with 36 for a pattern designed with the genetic algorithm.

8.1 SECTION 8 REFERENCES

[8.1] P.D. Henshaw and N.R. Guivens, Jr., "Genetic Algorithms for Unconventional Imaging," in Inverse Optics III, Proc. SPIE 2241, 257-265 (April 1994).

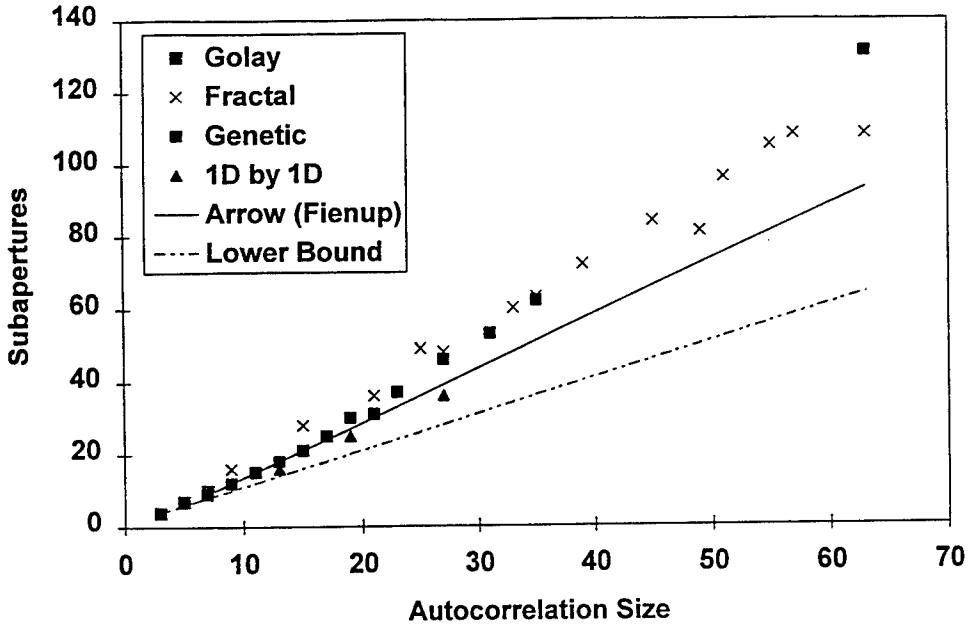

Figure 8-3. Comparison of Number of Subapertures Needed to Synthesize a Filled OTF as a Function of OTF (Autocorrelation) Size.(From [8.1].)

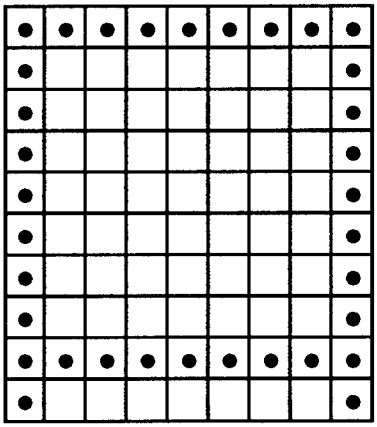

Figure 8-4. Box+2 Array Pattern.

9 INTERMEDIATE-PLANE DETECTION

Usually conventional imaging sensors make measurements in a focal plane of an optical system, whereas many unconventional imaging sensors, including the ones considered in this report, make measurements in the pupil plane. An exception is the case in which each subaperture of the receiver is small compared with the diameter of a pupil-plane laser speckle. If we put an array of detectors in such a focal plane, then the intensity measured by any one CCD element (or any collection of them) is equivalent to the intensity in the pupil plane. However, each CCD element then "sees" laser light from only a small portion of the sky. Consequently, a CCD array in the focal plane of a small subaperture can (1) rapidly steer the field-of-view, (2) have a large instantaneous field-of-regard, (3) gather data on multiple well-separated target complexes in parallel, and (4) suppress background light. These advantages of a CCD array in the focal plane of each subaperture must be weighed against some disadvantages, including the relatively slow read-out time associated with most CCD arrays as opposed to an array of, say, avalanche photo-diodes.

For those situations in which a CCD array in the back focal plane is desirable, we can obtain additional design options by a new approach that entails putting the CCD array in a plane that is not the focal plane of the subarray optics. Specifically, it allows the use of subapertures that are larger in diameter than the speckle size in the pupil plane; that is, the target can be partially resolved by the subaperture. This would allow a system that can image targets at a wider range of distances.

This situation is illustrated in Figure 9-1. In the figure, the first plane behind the lens represents the focal plane of the subaperture. Parallel rays from the target come to focus in that plane. The second plane behind the lens represents the new proposed position for the array of detectors. Rays striking a point in that plane come from the same general direction as the rays striking the corresponding (demagnified) position in the focal plane. However, the rays coming to the second plane arrive from a wider range of angles than rays hitting the corresponding point in the focal plane. Hence there is less field-of-view selectivity in the second plane. However, notice that the rays hitting that point all pass through a single point in front of the pupil, in a plane indicated in the

figure by the second, longer line a distance in front of the lens. In effect, the optical system is forming an image of the speckle pattern that is in that plane in front of the lens. Hence, if the lens has a diameter of more than one speckle, the detector can record multiple speckles. As seen from the lower part of the figure, rays hitting different pixels come from different parts of the lens, i.e., from different speckles.

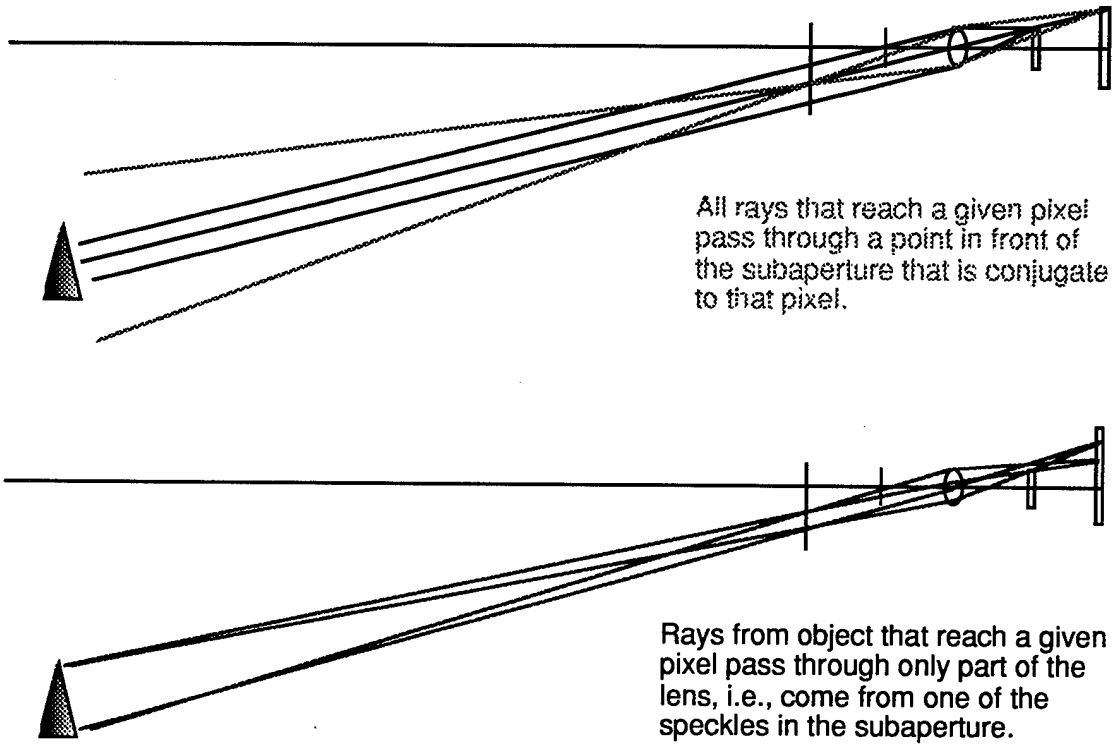

Figure 9-1. Detector Array in a Plane Behind the Focal Plane of the Lens. (a—upper) Rays arriving at a pixel pass through a single point in a plane in front of the lens; (b—lower) rays hitting different pixels come from different parts of the lens, i.e., from different speckles.

In summary, for a detector array in focal plane, each pixel sees a different IFOV, thereby maximizing spatial background suppression, and each pixel integrates over the entire entrance aperture. Then we must have subaperture diameter less than a speckle size. At the other extreme, for a detector array in a plane that re-images the aperture plane, each pixel sees the FOV of the telescope, yielding minimum background suppression, and each pixel sees a small portion of the entrance aperture, and so we can measure many speckles over a subaperture. Both of these extremes are poor for the

case of a small number of speckles per subaperture. The new method of putting the detector array in an intermediate plane, behind the focal plane, then each pixel sees a somewhat larger IFOV than for the focal plane, yielding partial background suppression, and each area of the detector sees a different aperture-plane speckle, allowing multiple speckles to be measured simultaneously. Hence it allows a trade-off of IFOV (background suppression) against the ability to measure multiple aperture-plane speckles simultaneously.

APPENDIX A

This appendix describes the theory behind most of the imaging modalities analyzed in this report. It is from J.R. Fienup, "Unconventional Imaging Systems: Image Formation from Non-imaged Laser Speckle Patterns," in Emerging Systems and Technologies, S.R. Robinson, Ed., Vol. 8 of The Infrared & Electro-optical Systems Handbook, (ERIM, Ann Arbor, 1993), Chapter 1.5, pp. 92-109.

A reader unfamiliar with pupil-plane laser imaging modalities would benefit from reading this appendix first.

1.5 IMAGE FORMATION FROM NONIMAGED LASER SPECKLE PATTERNS

Written by James R. Fienup

In most conventional imaging systems, an image is formed by an optical system and the electromagnetic radiation (light, when at optical wavelengths) is detected in the image plane directly. However, if the scene or object being imaged is illuminated by coherent radiation, as from a laser, then several alternative approaches can be used to form an image without the use of image-forming optics. Images can be formed from data collected in a plane where the aperture of an imaging system would ordinarily be located. This is possible because the electromagnetic field in the plane of the receiver is related to the field reflected by the scene by an invertible transform. The transform is the Fresnel transform if the scene is in the near field of the receiver, and the Fourier transform if in the far field.[393] If field measurements are made at an array of points in an aperture plane (i.e., without a focusing system) by heterodyne or holographic methods, then the image formation can be accomplished by an inverse Fourier (or Fresnel) transform in a digital computer. This is commonly done for microwave synthetic aperture radar (SAR) systems.

The symbols used in this section are defined in Table 1.2.

The resolution limit imposed by diffraction is

$$\rho = \lambda R/D_a \ , \tag{1.144}$$

where ρ = resolution at the object, λ = wavelength, R = range to target, and D_a = diameter of the aperture or collecting array.

The familiar $1.22\lambda R/D_a$ is replaced by $\lambda R/D_a$ because we are considering a square aperture of length D_a. To image distant objects with very fine resolution, this limit on resolution forces the use of short wavelengths in order to allow for apertures of practical size. However, for shorter wavelengths, particularly in the ultraviolet through the midinfrared, heterodyne measurements of the field are very difficult. Furthermore, at these wavelengths the turbulence of

Table 1.2 Symbols, Nomenclature, and Units

Symbol	Nomenclature	Units
c	Speed of light	m/s
C	Autocovariance of aperture-plane intensity	W^2/m^2
d_a	Detector spacing	m
$d_a^2\eta_d$	Area of one detector	m^2
D_a	Diameter of receiver aperture	m
D_o	Object diameter	m
f	Optical field in object plane	$\sqrt{W/m^2}$
f_I	Incoherent object brightness	W/m^2
F	Optical field in aperture plane	$\sqrt{W/m^2}$
F_I	Fourier transform of incoherent object	W/m^2
g	Optical field in image plane	$\sqrt{W/m^2}$
h	Planck's constant	J s
i	$\sqrt{-1}$	
L_c	Coherence length of laser	m
L_p	Length of laser pulse	m
M	Number of detectors per aperture-plane speckle	
n_{bp}	Number of resolved bright image points at a given resolution	
n_d	Average number of photons per detector	
n_s	Number of speckles in the aperture	
N	Number of independent realizations of the speckle pattern	
N_m	Maximum number of independent realizations available	
p	Coherent impulse response	
P	Pupil function	
r	Autocorrelation of coherent object	W/m
r_I	Autocorrelation of incoherent object	W^2/m^2
r_o	Object average reflectivity	
R	Range to object	m
s	Point spread function, $\lvert p\rvert^2$	
S	(Normalized) optical transfer function	
S_o	(Unnormalized) optical transfer function	
SBP_{max}	Maximum 1-D space-bandwidth product	
SNR	Signal-to-noise ratio	
(u,v)	Spatial-frequency coordinates	m
u_r	$(u^2 + v^2)^{1/2}$	m
v_a	Speckle velocity in aperture plane	m/s
v_o	Object velocity	m/s
(x,y)	Image-plane coordinates	m
(x_a,y_a)	Aperture-plane coordinates	m
(x_o,y_o)	Object-plane coordinates	m
Greek:		
Δt_1	Time for pattern to move across one-quarter of the speckle width	s

(continued)

Table 1.2 *(continued)*

Symbol	Nomenclature	Units
Δt_a	Time for pattern to move across aperture	s
Δt_m	Time before object rotates too much	s
Δz	Object depth along line of sight	m
η_d	Detector duty cycle	
η_q	Quantum efficiency of the detector	
λ	Wavelength	m
μ	Complex coherence factor	
ρ_a	Speckle width at aperture	m
ρ_o	Potential resolution at object	m
τ_{atm}	One-way atmospheric transmittance	
τ_{opt}	Transmittance of receiver optics (if any)	
τ_{pol}	Fraction of light reflected in desired polarity	
ϕ	Estimate of aperture-plane phase	rad
ψ	Aperture-plane phase	rad
ω	Object rotation rate (axis perpendicular to line of sight)	rad/s
Operators:		
$\mathcal{F}$	Fourier transformation	
$*$	Convolution	
$\otimes$	Autocorrelation	

the atmosphere causes phase errors in the field propagated through it, which can severely limit the resolution of a heterodyne system. If it is possible to reconstruct an image from the intensity of the field in the aperture plane, then these limits to resolution caused by aberrations can be overcome. Figure 1.40 shows examples of configurations that can be used to gather the aperture-plane intensity. These laser intensity patterns are speckled if the scene is rough in comparison to the wavelength of illumination. In this section, some methods for forming images from nonimaged, aperture-plane speckle patterns are discussed. First some terms are defined and a few methods are briefly described. Then one particular method, imaging laser correlography, is described in more detail, to serve as an example of a nonconventional imaging method using aperture-plane speckled intensity patterns.

These techniques generally require that the scene be of limited extent—that it be a bright object on a dark background. They have been developed primarily for the applications of fine-resolution imaging of space objects by ground-based systems and of discriminating decoys from reentry vehicles for the Space Defense Initiative (SDI) midcourse phase. Another application could be the imaging of a ground scene from an overhead platform if only a well-defined portion of the ground were illuminated by a coherent source. Relying on powerful sources of short-wavelength, coherent radiation, these techniques have been in development only since the 1960s. The first concerted effort[394–396] to develop these ideas began at the Woods Hole Summer Study in 1966.

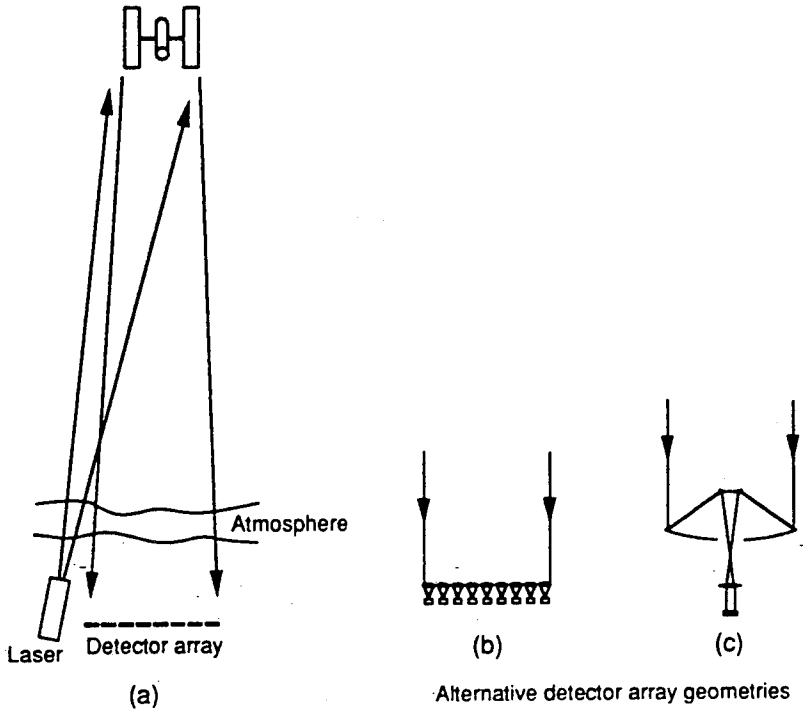

Fig. 1.40 Imaging geometries: (a) The intensity of coherent radiation scattered from an object is measured by an array of detectors without intervening optics. (b) Alternatively, a collection lens can be used to gather the light onto each of the individual detectors, which can have smaller areas. (c) Another alternative is to reimage the pupil plane of a telescope onto a detector array of small dimensions, such as a CCD array.

1.5.1 Basic Imaging Equations

Because of the mixture of coherent and incoherent imaging concepts inherent in imaging correlography, it is necessary to define here the basic imaging equations that will be needed later in this section.

The object is assumed to be illuminated by radiation that is both spatially and temporally coherent over the volume of the object. Here we refer to the illuminated scene as the object. Let the complex field reflected by the object be $f'(x_o,y_o)$ in a plane perpendicular to the line of sight (LOS). Then the field in the aperture plane at the detector array, also for simplicity assumed to be perpendicular to the LOS, is given by the Fresnel transform[393]:

$$F'(x_a,y_a) = \frac{1}{i\lambda R}\exp\left(\frac{i2\pi}{\lambda R}\right)\exp\left[\frac{i\pi}{\lambda R}(x_a^2 + y_a^2)\right] \times \iint f'(x_o,y_o)\exp\left[\frac{i\pi}{\lambda R}(x_o^2 + y_o^2)\right] \times \exp\left[\frac{-i2\pi}{\lambda R}(x_a x_o + y_a y_o)\right] dx_o\, dy_o \ . \tag{1.145}$$

In this section, all integrals are over $(-\infty,\infty)$. For the case of a diffusely scattering object, the intensity of this aperture-plane optical field is a speckle pattern. We are assuming that in front of the detector array is a polarizer that selects a single polarization, which is necessary for the methods described here to work. Hence, throughout this section we are considering radiation of a single polarization, enabling us to employ scalar diffraction theory.

If we absorb the constant phase term $-2\pi/\lambda R$, the quadratic phase term $(-\pi/\lambda R)(x_a^2 + y_a^2)$, and the factor i into the phase of $F'(x_a,y_a)$ to form $F(x_a,y_a)$, and absorb the quadratic phase term $(\pi/\lambda R)(x_o^2 + y_o^2)$ into the phase of $f'(x_o,y_o)$ to form $f(x_o,y_o)$, then we have the simpler Fourier transform relationship

$$F(x_a,y_a) = |F(x_a,y_a)| \exp[i\psi(x_a,y_a)] = \mathcal{F}[f(x_o,y_o)]$$
$$= \frac{1}{\lambda R}\int\int f(x_o,y_o) \exp\left[\frac{-i2\pi}{\lambda R}(x_a x_o + y_a y_o)\right] dx_o\, dy_o \qquad (1.146)$$

between the field $f(x_o,y_o)$ at the object plane and the field $F(x_a,y_a)$ at the receiver plane. This Fourier relationship is valid for the near-field conditions[393] normally allowed only for the Fresnel transform. If the complex-valued aperture-plane field, $F(x_a,y_a)$, could be measured without any phase errors, then an inverse Fourier transform performed in a computer would yield a diffraction-limited complex-valued, coherent image. This image would be given by the convolution (with appropriate scaling of the coordinates to account for the image magnification)

$$g(x,y) = f*p(x,y) = \frac{1}{\lambda R}\int\int f(x_o,y_o)p(x - x_o, y - y_o)\, dx_o\, dy_o \ , \qquad (1.147)$$

where $*$ denotes convolution, $p(x,y) = \mathcal{F}^{-1}[P(x_a,y_a)]$ is the system (coherent) impulse response, and $P(x_a,y_a)$ is the pupil function (unity over the extent of the aperture and zero outside). The corresponding point spread function for incoherent imaging through the same aperture would be

$$s(x,y) = |p(x,y)|^2 = \mathcal{F}^{-1}[S_o(u,v)] \ , \qquad (1.148)$$

where $S_o(u,v)$ is the unnormalized optical transfer function, given by the autocorrelation of the pupil function:

$$S_o(u,v) = P\otimes P(u,v) = \frac{1}{\lambda R}\int\int P(x_a,y_a)P^*(x_a - u, y_a - v)\, dx_a\, dy_a \ , \qquad (1.149)$$

and P^* is the complex conjugate of P, and (u,v) is a spatial-frequency coordinate. The (normalized) optical transfer function is given by

$$S(u,v) = \frac{S_o(u,v)}{|S_o(0,0)|} \ . \qquad (1.150)$$

Like any coherent image, $g(x,y)$ would be speckled, assuming that the surface of the object is rough compared to the wavelength of the radiation.[397] As the object translates or rotates, a new part of the back-scattered field falls on the receiver; effectively, the object takes on a different realization of the phase in the object plane. When we wish to distinguish these different fields coming from the object, we denote the n'th realization of the object field as $f_n(x_o,y_o)$ and the corresponding field at the aperture plane as $F_n(x_a,y_a)$. The image of each $f_n(x_o,y_o)$ would have a different realization of the speckle pattern across it. If the field in the aperture plane translates by the width of the aperture between the time the two images are collected, then, for the case of a diffusely scattering object, the two field distributions are independent and the complex images are uncorrelated. Conditions for achieving this are discussed in Sec. 1.5.4.1. An average over many such object realizations would give

$$f_I(x_o,y_o) = \langle |f_n(x_o,y_o)|^2 \rangle_n = \lim_{N\to\infty} \frac{1}{N} \sum_{n=1}^{N} |f_n(x_o,y_o)|^2 , \tag{1.151}$$

where $\langle \cdot \rangle_n$ denotes the ensemble average over the speckle realizations or aspect angles and N is the number of independent realizations. This noncoherent average of many coherent objects yields the ordinary incoherent reflectivity (or brightness distribution) of the object, which is a real-valued, non-negative distribution. We denote the Fourier transform of the incoherent object, $f_I(x_o,y_o)$, as $F_I(u,v)$. The coherent images $p*f_n(x,y)$ are speckled versions of $s*f_I(x,y)$, the image of the incoherent object. The normalized Fourier transform,

$$\mu(u,v) = \frac{F_I(u,v)}{F_I(0,0)} , \tag{1.152}$$

is the complex coherence factor (or the complex visibility function),[398] and $|\mu(u,v)|^2$ is the normalized spatial power spectrum (i.e., the normalized squared modulus of the Fourier transform) of the incoherent object.

1.5.2 Imaging Methods

The quantity that we assume to be measured, and from which we wish to reconstruct an image, is the aperture-plane intensity, $|F(x_a,y_a)|^2 = |F'(x_a,y_a)|^2$. The square root of the intensity, $|F(x_a,y_a)|$, is the magnitude (commonly called the *modulus* or *amplitude*) of the field and $\psi(x_a,y_a)$ is the phase. Without the phase of $F(x_a,y_a)$, the image cannot be computed simply by inverse Fourier transformation. Since $|\mathcal{F}[f^*(-x,-y)]| = |\mathcal{F}[f(x,y)]| = |F(x_a,y_a)|$, from the aperture-plane intensity it is impossible to distinguish between the object $f(x,y)$ and its twin $f^*(-x,-y)$. This twofold ambiguity is usually acceptable since the twin looks just like the object, but rotated by 180 deg, and it usually suffices for identifying the object. In addition, $|\mathcal{F}[f(x-x_1,y-y_1)]| = |\mathcal{F}[f(x,y)]|$, and so the absolute position of the object cannot be determined from the intensity $|F(x_a,y_a)|^2$ alone.

We next briefly describe some of the methods that can be used to form images from this seemingly insufficient aperture-plane intensity data.

1.5.2.1 Holography. By inverse Fourier transforming $|F(x_a,y_a)|^2$, we arrive at the autocorrelation of the object:

$$r(x,y) = f \otimes f(x,y) = \frac{1}{\lambda R}\int\int f(x',y')f^*(x - x', y - y')\, dx\, dy$$
$$= \mathcal{F}^{-1}[|F(x_a,y_a)|^2] \; . \tag{1.153}$$

If the object consists of an extended part of the object plus a glint, separated from the extended part by at least the width of the extended part, then $|F(x_a,y_a)|^2$ is the equivalent of a hologram[399] of the extended part. When this holographic condition is met, the autocorrelation consists of four terms, one of which is an image of the extended part of the object. Since $|F(x_a,y_a)|^2$ is measured only over the aperture $P(x_a,y_a)$ of width D_a, the autocorrelation and the reconstructed image are limited in resolution (in object space) to $\rho = \lambda R/D_a$. This imaging modality was analyzed for the case of imaging space objects from the earth by Refs. 394 and 395.

1.5.2.2 Object Support from Autocorrelation Support. The diameter of the object $f(x,y)$ along any direction is just half the diameter of the autocorrelation $r(x,y)$ along the same direction. The support of the object is defined as a set of points (or an area) outside of which the object has a value of zero, consistent with the assumption that we are considering bright objects on a dark background. The support of the autocorrelation allows us to determine bounds on the support of the object. For the sake of brevity these methods are not detailed here, except to say that they involve taking the intersection of two or more translated versions of the support of the autocorrelation. The reader is referred to Refs. 401 and 402 for the details. For favorable cases, such as a highly nonconvex object or an object consisting of two or more separated parts, the upper bound on the support of the object can serve as an approximate outline of the object. This outline may be sufficient information about the object for some applications. For less favorable cases, such as for a convex object, the upper bound only gives the general size of the support of the object. In all cases, the upper bound on the support can be used as a support constraint for phase retrieval, as is described in the next section.

1.5.2.3 Phase Retrieval. An approach to image formation from coherent aperture-plane intensity is *phase retrieval*. The approach is to use a computer algorithm to determine a phase $\phi(x_a,y_a)$, which, when combined with $|F(x_a,y_a)|$ from the measured intensity and Fourier transformed, yields an image

$$\hat{g}(x,y) = \mathcal{F}^{-1}\{|F(x_a,y_a)| \exp[i\phi(x_a,y_a)]\} \tag{1.154}$$

that is consistent with the support constraint (i.e., has a value close to zero in the region outside the upper bound on the support of the object). Dozens of phase retrieval algorithms have been proposed—see, for example, Ref. 403. Phase retrieval algorithms have been particularly successful for real-valued,

non-negative images such as those one would have for incoherent illumination. However, from $|F(x_a,y_a)|$ the quantity being reconstructed is the field, which is complex valued. Then the only constraint available is the support constraint. In this case it is possible to reconstruct an image, particularly for objects consisting of two or more separated parts; but it is difficult and is not yet reliable for general objects.[404,405]

1.5.2.4 Additional Measurements. If additional measurements are made, then the problem of reconstructing a complex-valued image becomes much easier. One example for a space-based system is to have a diffraction-limited aperture of moderate size embedded within a larger array of detectors. By use of a beamsplitter, the intensity passing through the moderate-sized aperture is measured simultaneously in two different planes: in the focal plane, which contains a diffraction-limited but moderate-resolution image, and in the plane of the aperture.[406] Then the reconstruction of the phase over the diffraction-limited aperture can be accomplished by an iterative algorithm that is robust.[407,408] This phase can then be used to help to reconstruct the phase over the larger array, where only intensity measurements were made, in a bootstrapping version of a phase retrieval algorithm.[406]

A second approach using additional measurements is to combine aperture-plane intensity methods with wavefront sensor data. The imaging wavefront (Hartmann-Idell) sensor[409] combines wavefront slope data from a Hartmann array with the aperture-plane intensity data to reconstruct the optical field, from which an image is reconstructed by Fourier transformation. By temporally averaging the wavefront slopes over many speckle realizations during a time interval less than the atmospheric correlation time, it is also possible to estimate the aberrations due to the turbulent atmosphere, which could then be subtracted to form a diffraction-limited image.

Other schemes using additional measurements are also possible.

1.5.3 Imaging Correlography

The diffraction-limited autocorrelation, $p*r_n(x,y)$, which can be computed from the aperture-plane intensity $P(x_a,y_a)|F_n(x_a,y_a)|^2$, is a complex-valued, speckled autocorrelation. As the object translates or rotates, the aperture-plane intensity pattern moves. After sufficient motion at the receiver a new realization of the speckled intensity pattern appears, which yields a new realization of the speckled autocorrelation. The diffraction-limited autocorrelation of the incoherent image, $|p|^2*r_I(x,y)$, can be determined by averaging the squared magnitudes of the speckled autocorrelations over many realizations of the speckle pattern[410–412]:

$$\lim_{N\to\infty} \frac{1}{N} \sum_{n=1}^{N} |p*r_n(x,y)|^2 = b_1|p(x,y)|^2 + b_2|p|^2*r_I(x,y) \ , \tag{1.155}$$

where

$$b_1 = b_2\left[\int\int |f_I(x',y')|^2 \, dx' \, dy'\right]^2 \tag{1.156}$$

is the square of the total measured intensity, b_2 is a constant, and N is the number of independent realizations. This result assumes a rough object whose coherent autocorrelation function is of the form of a delta function. The first term on the right-hand side of Eq. (1.155) is a point-spread function of known shape located at the origin (the dc term) that can be subtracted, leaving $|p|^2 * r_I(x,y)$, the diffraction-limited autocorrelation of the incoherent object. That is, the noncoherent average of the autocorrelations of the *coherent* images yields the autocorrelation of the *incoherent* image. Alternatively, processing the same intensity measurements $P(x_a,y_a)|F_n(x_a,y_a)|^2$ in a different way,[413] we compute the autocovariance of the intensity, which is given by

$$C(u,v) = \lim_{N\to\infty} \frac{1}{N} \sum_{n=1}^{N} \iint P(x_a + u, y_a + v)P(x_a,y_a) \times [|F_n(x_a + u, y_a + v)|^2 |F_n(x_a,y_a)|^2 - \bar{I}^2]\, dx_a\, dy_a \ , \tag{1.157}$$

where $\bar{I}$ is the average intensity over the aperture plane. Using the moment factoring theorem for circular-complex Gaussian fields (Ref. 414, p. 44), it can be shown that

$$\lim_{N\to\infty} \frac{1}{N} \sum_{n=1}^{N} [|F_n(x_a + u, y_a + v)|^2 |F_n(x_a,y_a)|^2 - \bar{I}^2] = |F_I(u,v)|^2 \ , \tag{1.158}$$

and so

$$C(u,v) = S(u,v)|F_I(u,v)|^2 \ , \tag{1.159}$$

where $S(u,v)$ is the optical transfer function for the aperture. That is, the autocovariance of the intensity of the *coherent* aperture-plane field is proportional to the squared magnitude of the Fourier transform of the *incoherent* object. This is related to the incoherent autocorrelation $r_I(x,y)$ by a Fourier transform. Computation of the autocovariance of the aperture-plane intensity is completely equivalent to intensity interferometry,[415] but using realizations of reflected laser speckle patterns rather than incoherent light emitted by the object.

Each pair of detectors over the aperture contributes to a measure of $C(u,v)$ and therefore to $|F_I(u,v)|^2$. If the pair of detectors is at locations (x_{a1},y_{a1}) and (x_{a2},y_{a2}) in the aperture plane, then they contribute to a measurement of $|F_I(u,v)|^2$ at spatial frequency $(u,v) = \pm(x_{a1} - x_{a2}, y_{a1} - y_{a2})$. [The $\pm$ is due to the fact that $|F_I(-u,-v)|^2 = |F_I(u,v)|^2$, and both are measured simultaneously.] In radio interferometry, the separations (u,v) are referred to as *baseline separations*. Redundant measurements—different pairs of detectors with the same baseline separations—contribute to increasing $S(u,v)$ and increasing the SNR of the estimate of $|F_I(u,v)|^2$.

Having computed $|F_I(u,v)|$ as described, an incoherent image can be fairly reliably reconstructed using a phase retrieval algorithm, even though the reconstruction of the individual coherent images from the intensities $|F_n(x_a,y_a)|^2$ is difficult. The reconstruction is easier for incoherent images because, in addition to the support constraint, we have the additional constraint that the image is a real-valued, non-negative function.

Prior to image reconstruction, it is usually advantageous to perform a filtering or a weighting of $|F_I(u,v)|$. This is needed because the SNR for the higher spatial frequencies is much poorer than that at lower spatial frequencies. For the highest spatial frequencies, the noise usually dominates. The spatial frequencies at which SNR $\leq$ 1 should be discarded or at least greatly deemphasized. This can be accomplished, for example, by multiplying $|F_I(u,v)|$ by a filter function

$$W(u,v) = \frac{S(u,v)|\hat{F}_I(u,v)|^4}{|S(u,v)|^2|\hat{F}_I(u,v)|^4 + \Phi(u,v)}, \tag{1.160}$$

where $|\hat{F}_I(u,v)|^2$ is an estimate of $|F_I(u,v)|^2$ (which could be an average power spectrum for objects of an appropriate class) and $\Phi(u,v)$ is the variance of the noise in the estimate of the autocovariance function. This filter function is related to the Wiener-Helstrom filter.[416] Other variations on the filter function have also been used—anything that suppresses the highest spatial frequencies, where SNR $\leq$ 1, can be beneficial.

Figures 1.41 and 1.42 show an example of a computer simulation of imaging laser correlography.[412] In Fig. 1.41 we see that as more realizations of the

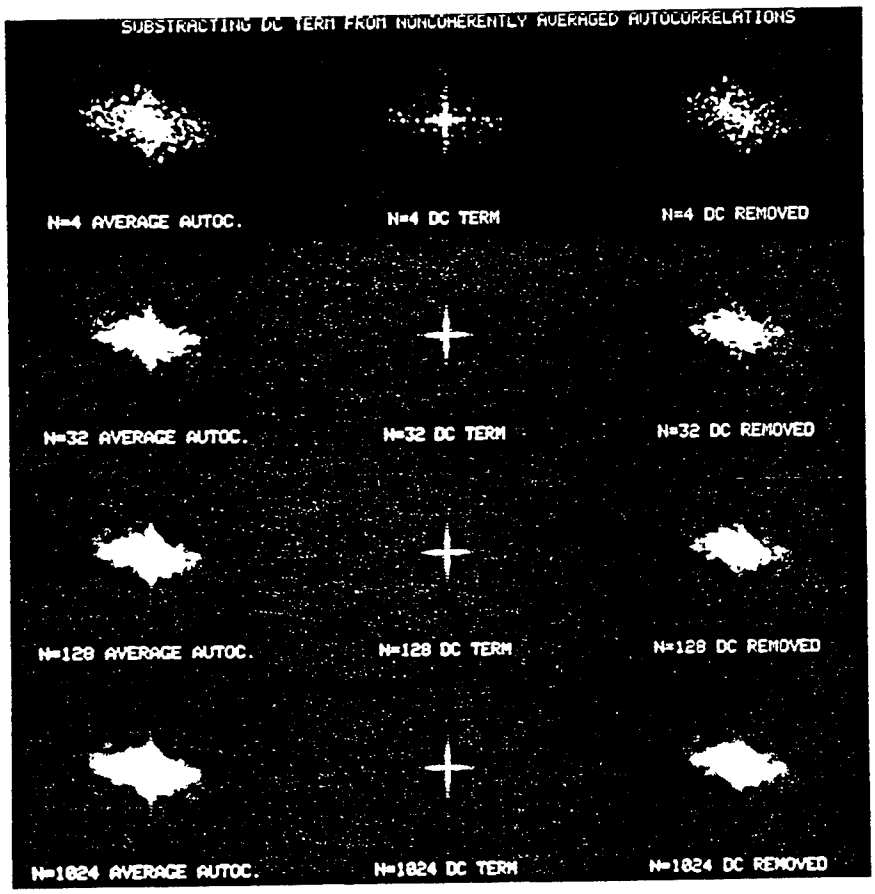

Fig. 1.41 Noncoherent averages of coherent image autocorrelations.[412] First row, left to right: noncoherent average of $N = 4$ coherent image autocorrelations, dc term, and averaged autocorrelation with dc term subtracted; second row: $N = 32$; third row: $N = 128$; and fourth row: $N = 1024$.

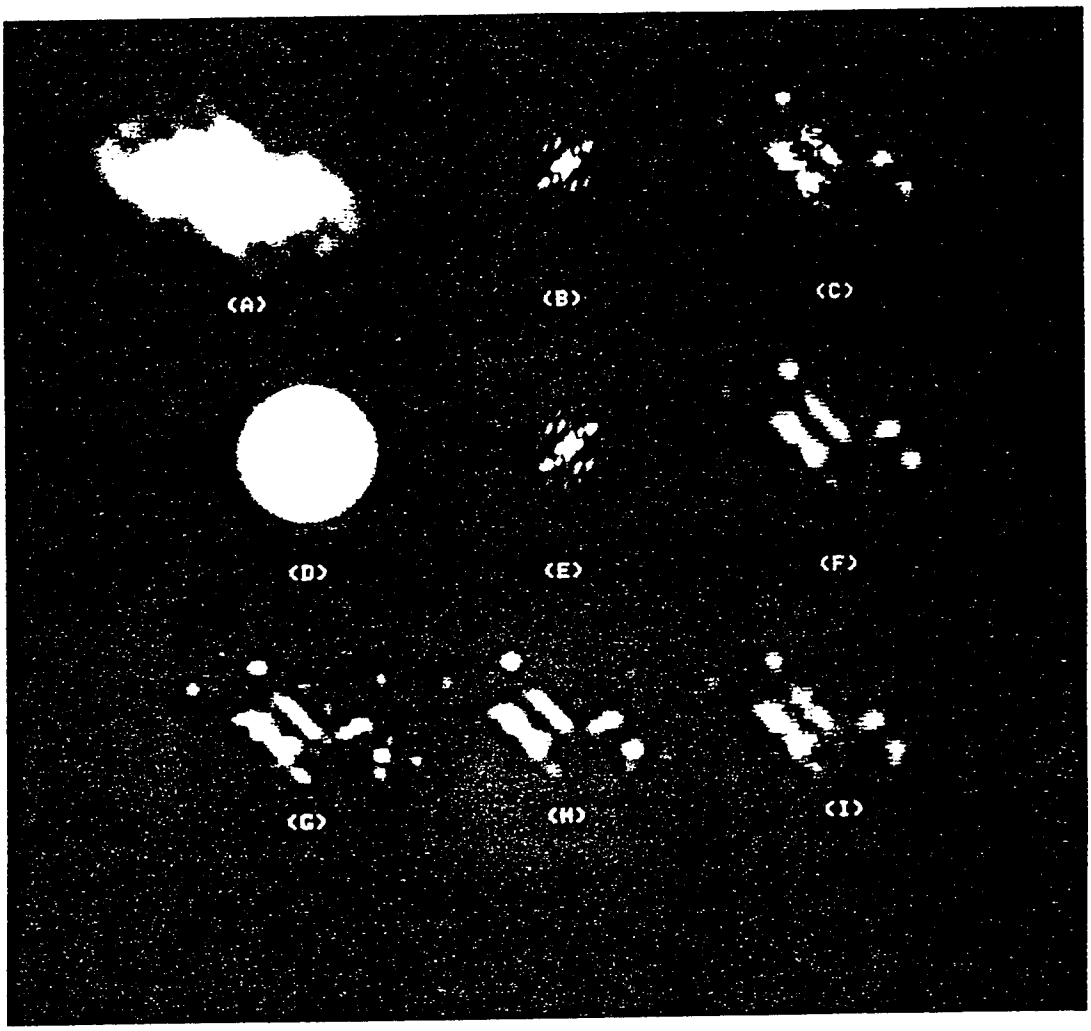

Fig. 1.42 Image recovery from simulated correlography data.[412] (A) Estimate of the autocorrelation of the incoherent image from $N = 10{,}000$ coherent image autocorrelations; (B) estimate of the Fourier modulus of the incoherent object; (C) image reconstructed from (B) by means of the iterative-transform phase retrieval algorithm; (D) Wiener filter; (E) filtered Fourier modulus; (F) image reconstructed from (E); (G) original incoherent object; (H) Wiener-filtered incoherent object; and (I) result of Wiener filtering of (C).

speckled autocorrelations are averaged together, it approaches the autocorrelation of the incoherent object. Figure 1.42 shows an example of image reconstruction from simulated correlography data using the iterative transform phase retrieval algorithm.[408] Filtering the data is necessary to suppress noise at the higher spatial frequencies. Figure 1.42(F), which shows the image reconstructed from the filtered data, compares favorably with Fig. 1.42(H), which shows the ideal image passed through the same filter. Figure 1.43 shows an example of imaging laser correlography in a laboratory experiment.[400,417]

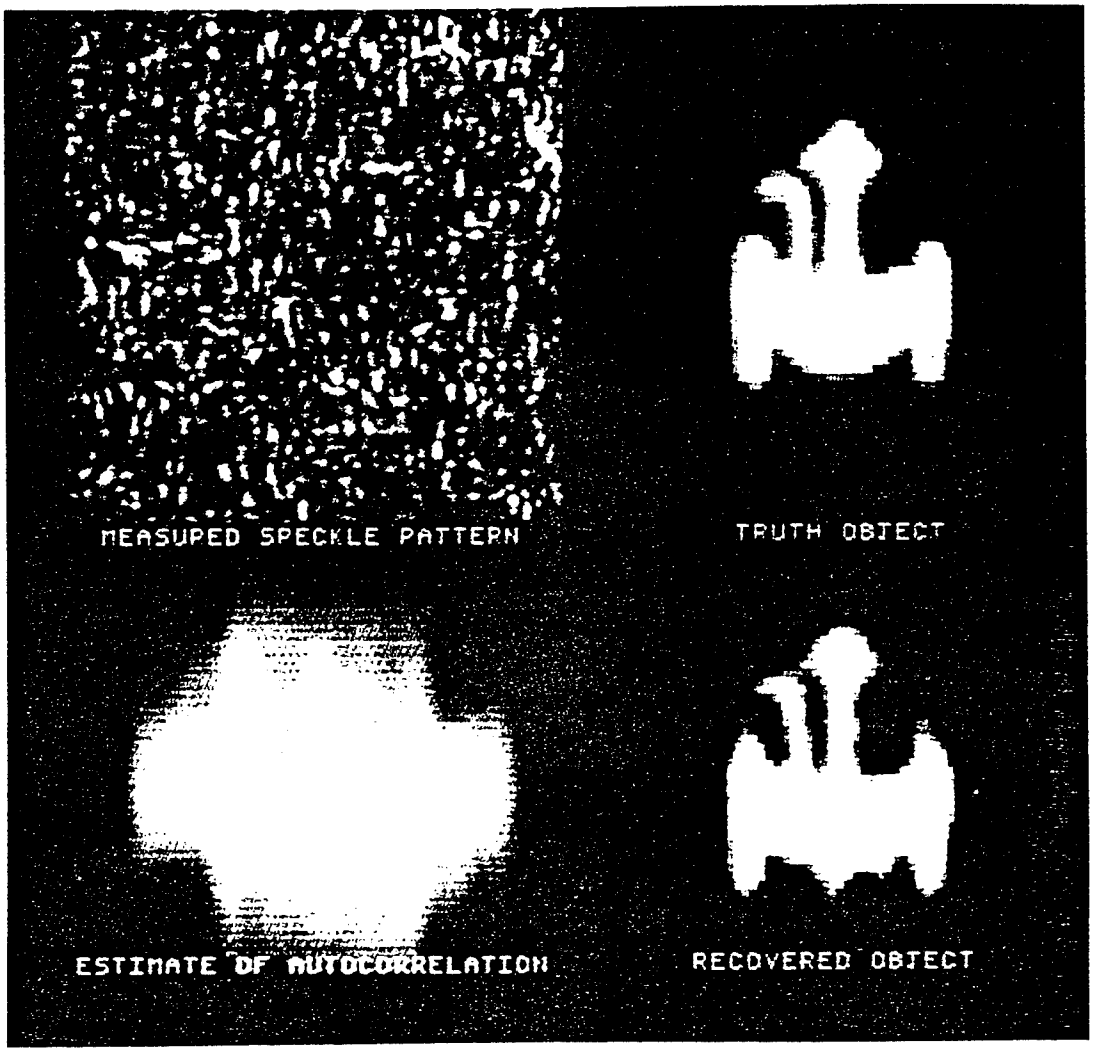

Fig. 1.43 Example of reconstruction from data gathered in the laboratory. *Top left:* one realization of the measured speckle intensity patterns; *top right:* incoherent image of the object; *bottom left:* autocorrelation estimate computed using 100 realizations of the speckle pattern; and *bottom right:* the reconstructed image. (Image courtesy of J. D. Gonglewski, P. S. Idell, and D. G. Voelz, Phillips Laboratory)

1.5.4 System Parameters

With the basic method of imaging laser correlography in hand, we now describe the requirements on the system—the transmitter (laser) and the receiver (detector array). For the sake of an example calculation, we use the parameters given in Table 1.3.

1.5.4.1 Receiver Requirements. To obtain a resolution at the object of ρ_o ($=0.2$ m for the example), an aperture with a diameter of at least

$$D_a = \frac{\lambda R}{\rho_o} \tag{1.161}$$

Table 1.3 Example of Parameters for an Imaging Scenario

Symbol	Example Value	Description
D_o	5 m	Object diameter
Δz	5 m	Object depth along LOS
ω	1 rad/s	Object rotation rate (axis perpendicular to LOS)
v_o	5 km/s	Object velocity perpendicular to LOS
λ	1 μm	Wavelength
R	1000 km	Range to object
D_a	5 m	Receiver aperture diameter
ρ_o	0.2 m	Resolution at object = $\lambda R/D_a$
ρ_a	0.2 m	Speckle size in aperture = $\lambda R/D_o$

(= 5 m for the example) is required. Limits on resolution that have to do with the SNR will be discussed later.

A fundamental quantity needed to explain the system requirements is the characteristic diameter ρ_a of the speckles in the detected intensity pattern, $|F_n(x_a,y_a)|^2$. It is given by

$$\rho_a = \frac{\lambda R}{D_o} \tag{1.162}$$

(= 0.2 m for the example). The maximum possible space-bandwidth product of the image in each dimension is

$$\text{SBP}_{\max} = \frac{D_o}{\rho_o} = \frac{D_o D_a}{\lambda R} = \frac{D_a}{\rho_a} \tag{1.163}$$

(= 25 for the example). This is the maximum number of resolution elements across the object, which is equal to the number of speckles across the aperture. The actual number of resolution elements across the object may be fewer because the resolution can be limited by noise, as is described later. In order for $|F_n(x_a,y_a)|^2$ to be measured in the aperture plane without aliasing (to avoid undersampling), the center-to-center spacing of the detectors must satisfy

$$d_a \leq \frac{\rho_a}{2} = \frac{\lambda R}{2D_o} \tag{1.164}$$

(= 0.1 m for the example), which gives two samples per speckle in each dimension. For a filled array, D_a/d_a (= 50 for the example) detectors are needed in each dimension. However, since the data used for reconstruction, $|F_I(u,v)|^2$, are given by the autocorrelation of the measured data, $|F_n(x_a,y_a)|^2$, sampling of the measured data on a regular filled grid is not necessary. In fact, sparse arrays of detectors may be used.[413] The effective transfer function of the system is the autocorrelation of the aperture function, which is equivalent to the

optical transfer function. Issues regarding filling of the (u,v) plane (Fourier aperture) are similar to those encountered in radio interferometry.[418]

The intensity pattern moves across the aperture plane, due to the object's rotation, at a velocity $2\omega R$ (= 2000 km/s for the example), and so it moves by a speckle diameter in time $\rho_a/(2\omega R) = \lambda/(2\omega D_o)$ (= 100 ns for the example). Therefore the integration time for a single speckle pattern (without some form of speckle tracking) should be limited to about

$$\Delta t_1 \leq \frac{\lambda}{8\omega D_o} \tag{1.165}$$

(= 25 ns for the example). The intensity pattern also moves across the aperture plane at a velocity $2v_o$ (= 10 km/s for the example) due to the velocity of the object. Note that at long ranges the velocity of the aperture-plane speckles due to object rotation are much greater than that due to object velocity, except for very slow rotation rates. If the detectors have an integration time or a readout time that is long compared with Δt_1, then the detectors must be gated over an interval of time Δt_1 (or the speckles must be tracked). For a pulsed laser of pulse length L_p, a long-readout detector could only use the fraction $c\Delta t_1/L_p$ of the energy of the pulse, where c is the speed of light.

The time it takes the speckles to pass over the receiver aperture of diameter D_a is

$$\Delta t_a = \frac{D_a}{2\omega R} \tag{1.166}$$

(= 2.5 μs for the example). This is the time necessary to obtain an independent realization of the speckle pattern and defines the maximum rate at which independent realizations can be collected (400,000 independent realizations per second, for the example). The maximum integration time for a single speckle realization is less than Δt_a even with speckle tracking. Since there are $\mathrm{SBP}_{\max} = D_o/\rho_o$ (= 25 for the example) diffraction-limited resolution elements across the object, a rotation of the object by roughly $\lambda R/(D_o D_a)$ radians will cause the object brightness distribution to begin to change substantially. This would occur in time

$$\Delta t_m = \frac{\lambda R}{\omega D_o D_a} \tag{1.167}$$

(= 40 ms for the example). Unless multiple revolutions of the object are used, this is also the maximum amount of time available for gathering an image of the object for a single aspect angle. During time Δt_m, the maximum number of independent realizations available is

$$N_m = \frac{\Delta t_m}{\Delta t_a} = \frac{2\lambda R^2}{D_o D_a^2} \tag{1.168}$$

(= 16,000 realizations for the example).

A synthetic-aperture collection approach may also be taken. The approach described above is to gather N snapshots of the laser speckle pattern over a two-dimensional (possibly sparse) array of detectors. Using a synthetic-aperture approach, only a one-dimensional array of detectors is required. For simplicity, suppose that the 1-D array is along the y_a axis and that the speckles move in the x_a direction with velocity $v_a = 2\omega R$ (= 2000 km/s for the example). At any instant in time t, the array is collecting a 1-D cut, $|F_n(v_a t, y_a)|^2$, through the speckle pattern. As the speckle pattern sweeps across the 1-D array, additional slices of speckle pattern fall on the detector array. For the case of cw illumination, the detectors must read out each sample of the intensity in a time $\Delta t_1 \leq \lambda/(8\omega D_o)$ (= 25 ns for the example). Then the total data rate is $(D_a/d_a)/\Delta t_1$ (= 2×10^9 samples per second for the example). After time $\Delta t_a = D_a/v_a$ (= 2.5 μs for the example), a two-dimensional array of values of $|F_n(x_a,y_a)|^2$ has been read out, equivalent to a square area of length D_a. After time $N\Delta t_a$, a rectangular array of values of $|F_n(x_a,y_a)|^2$ has been read out of size $ND_a \times D_a$. This rectangular array can be subdivided into N square arrays of size $D_a \times D_a$, each equivalent to one of the snapshots (realizations) of the speckle pattern that would have been measured if we had a filled 2-D array. Even better than dividing the rectangle into squares would be to compute the covariance function $C(u,v)$ by summing over the products of all pairs of intensity measurements separated by the distance (u,v). This would increase the SNR somewhat for spatial frequencies having components in the u direction, since separations would be used that would otherwise have crossed the boundaries between the squares of data forming the snapshots. This idea of synthesizing a 2-D array from a 1-D array has the advantage of requiring many fewer detectors than a real 2-D array, but the detectors must be read out very fast and must be oriented appropriately with respect to the direction of the speckle velocity.

1.5.4.2 Transmitter Requirements. The received illumination is assumed to be quasimonochromatic, i.e., the intensity pattern $|F_n(x_a,y_a)|^2$ should be constant over the wavelength band in use. The requirements on the coherence length of the laser almost always supersede this requirement, which can thereby be ignored. The coherence length required of the laser illuminator is

$$L_c \geq 2\Delta z \tag{1.169}$$

(= 10 m for the example), where Δz is the depth of the object along the LOS.

If the laser is pulsed, then the pulse repetition frequency is required to be fast enough in order to obtain a large number of speckle realizations before the object rotates too much.

The laser power requirements are driven by several factors, including the fraction of the transmitted energy that falls on a detector and the SNR of $|F_I(u,v)|^2$ for correlography.

1.5.4.3 Signal-to-Noise Ratio. The SNR of $|F_I(u,v)|^2$ (the signal divided by the standard deviation of the noise), as limited by the number of realizations and photon noise, is given by[419]

$$\mathrm{SNR}(u,v) = \frac{[Nn_sS(u,v)]^{1/2}|\mu|^2}{\left[3 + 14|\mu|^2 + 3|\mu|^4 + \dfrac{4(1 + 2|\mu|^2)}{Mn_d} + \dfrac{1 + |\mu|^2}{Mn_d^2}\right]^{1/2}}, \quad (1.170)$$

where

n_d = the average number of photons per detector
M = the number of detectors (pixels) per aperture-plane speckle area
Mn_d = the average number of photons per speckle
n_s = the number of speckles within the area of the aperture.

In this formula, $|\mu|^2$ is a function of (u,v). Figure 1.44 shows two families of plots of $\mathrm{SNR}(u,v)$ as a function of light level for two values of $|\mu|^2$ (0.25 and 0.01); and several values of Mn_d, the number of photons per speckle. The first three terms in the denominator of the expression for $\mathrm{SNR}(u,v)$ are due to the approximation of the ensemble average for the autocovariance by a finite sum over N realizations, and the last two terms are due to photon noise. For $|\mu|^2 \ll 1$, and for $M = 4$ detectors per speckle, these two contributions to the noise are equal when $n_d = 0.5$ photon per detector or $Mn_d = 2$ photons per speckle. Consequently, photon noise can be ignored when there are much greater than 2 photons per speckle. For the case of a photon-counting detector, any laser power that yields more than about 8 photons per speckle is wasting energy, since at that point it is the number of realizations, not the photon noise, that is limiting the SNR, as can be seen from Fig. 1.44.

For the higher spatial frequencies, for which $|\mu|^2 \ll 1$, and for moderate light levels (greater than two photons per speckle), the SNR expression reduces to

$$\mathrm{SNR}(u,v) \approx [(N/3)n_sS(u,v)]^{1/2}|\mu(u,v)|^2 . \quad (1.171)$$

For a given object and resolution, this expression shows the trade-off that can be made between the number N of realizations and the number $n_sS(u,v)$ of redundant measurements of a given spatial frequency (u,v).

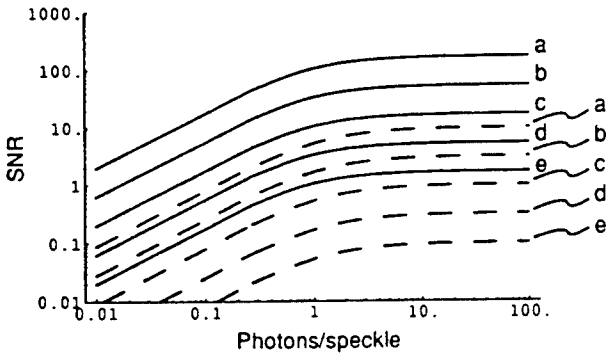

Fig. 1.44 The SNR versus number of photons per speckle. Solid lines: $|\mu|^2 = 0.25$; dashed lines: $|\mu|^2 = 0.01$. Number of realizations (top to bottom): (a) 10,000; (b) 1000; (c) 100; (d) 10; and (e) 1.

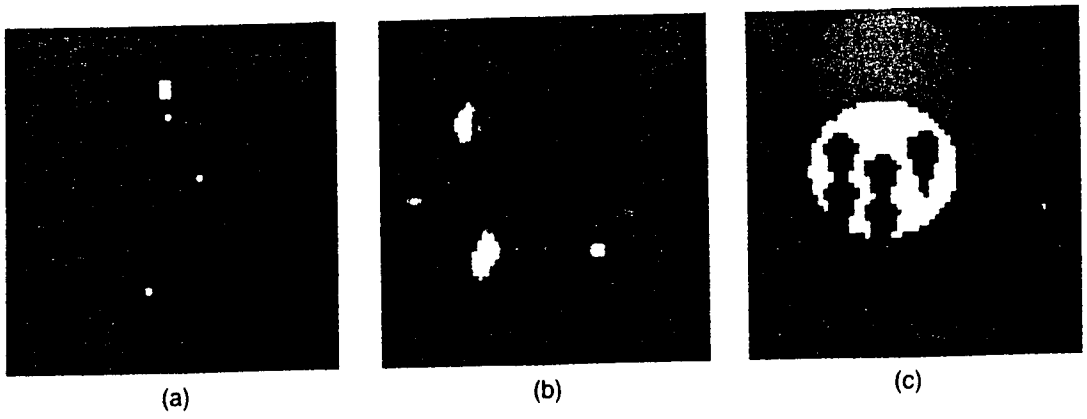

Fig. 1.45 Three types of objects: (a) four points—a 2 × 4-pixel rectangle plus three single-pixel points; (b) satellite—an object with glints; and (c) bus/RV—an extended diffuse object.

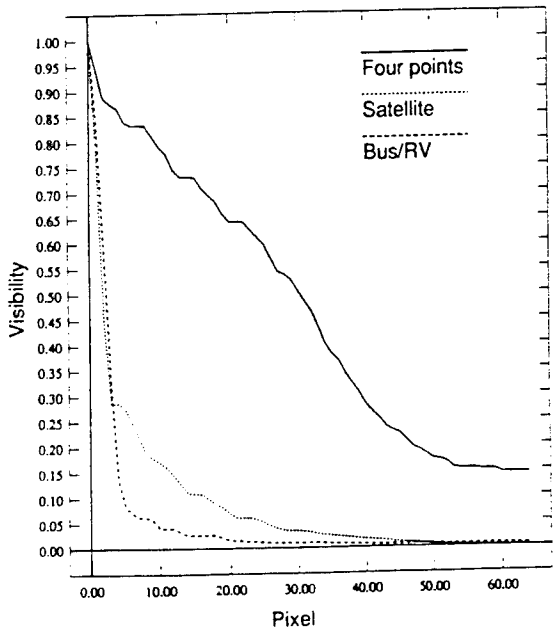

Fig. 1.46 Visibility (Fourier modulus) $|\mu|$ as a function of spatial frequency.

The SNR is approximately proportional to $|\mu(u,v)|^2$, which heavily depends both on (u,v) and on the structure of the object being imaged. At one extreme, an object consisting of a single unresolved glint (a delta function) has $|\mu(u,v)| = 1.0$ for all (u,v). At the other extreme, a diffuse, constant-value object that fills the field of view will have $|\mu(u,v)|$ that is a delta function and is negligibly small for $(u,v) \neq (0,0)$. To give you a feel for the values that $|\mu(u,v)|$ takes on for different types of objects, Fig. 1.45 shows three types of objects and Fig. 1.46 shows $|\mu(u_r)|$, the spin-averaged (azimuthally averaged) values of the visibility $|\mu(u,v)|$, where $u_r = (u^2 + v^2)^{1/2}$. A very rough rule of thumb is that

$$|\mu(u_r)|^2 \approx \frac{1}{n_{bp}} , \tag{1.172}$$

where n_{bp} is the number of resolved bright image points at resolution u_r. For an extended object n_{pb} is the number of 2-D resolution elements within the area of the object. So if, as the resolution improves with increasing u_r, more points in the diffraction-limited image of an object are resolved, then $|\mu(u_r)|^2$ decreases correspondingly.

Ideally the laser should have sufficient power so that the number of detected photons per speckle exceeds two. For a simplified object consisting of a flat plate that is a Lambertian reflector, the average number of photons per speckle is given by

$$Mn_d = E_L \tau_{\text{atm}}^2 \eta_{LA} (\cos\theta_i \cos\theta_o/\pi) r_o \tau_{\text{pol}} \tau_{\text{opt}} (\eta_d d_a^2/R^2) \eta_q (\lambda/hc) , \tag{1.173}$$

where

E_L = energy of the laser per pulse or per detector integration time
τ_{atm} = one-way atmospheric transmittance
η_{LA} = fraction of laser intensity falling on the area of the object
θ_i = angle between object surface normal and illumination
θ_o = angle between object surface normal and LOS
r_o = average reflectivity of object
τ_{pol} = fraction of light reflected in desired polarization
τ_{opt} = transmittance of receiver optics (if any)
$\eta_d d_a^2$ = area of one detector
η_q = quantum efficiency of the detector
hc/λ = energy of one photon (Planck's constant times frequency).

For example, for the parameters of Table 1.3 and for $E_L = 1$ J/pulse, $\tau_{\text{atm}}^2 \tau_{\text{pol}} \tau_{\text{opt}} = 0.2$, $\eta_{LA} = 0.1$, $\theta_i = \theta_o = 0$, $r_o = 0.5$, $\eta_d d_a^2 = 0.005$ m^2, $\eta_q = 0.1$, and $hc/\lambda = 2 \times 10^{-19}$ J/photon, we have $Mn_s = 8$ photons per speckle per pulse, which is in the high light-level regime.

If the receiver is ground based, then atmospheric scintillation could be a limiting factor, since it directly changes the measured aperture-plane intensity. However, since many speckle patterns are averaged, the effects of scintillation tend to cancel and are not expected to be a limiting factor for imaging objects directly overhead.

1.5.5 Conclusion

The use of laser illumination opens the possibility for many novel ways to image objects with resolution one to two orders of magnitude finer than conventional imaging systems that are limited by the blurring effects due to atmospheric turbulence. These imaging methods, which spring from the heritage of holography, are especially useful for obtaining fine-resolution images of earth-orbiting satellites. These same methods can also be applied to other imaging scenarios, ranging from microscopy to imaging of the ground from space. While these methods have been investigated and demonstrated to varying degrees of sophistication, they are just now on the verge of becoming operationally feasible.

380. K. Itoh, T. Inoue, T. Yoshida, and Y. Ichioka, "Interferometric supermultispectral imaging," *Appl. Opt.* **29**(11), 1625–1630 (1990).

381. K. Itoh, T. Inoue, and Y. Ichioka, "Interferometric spectral imaging and optical three-dimensional Fourier transformation," *Jap. J. Appl. Phys.* **29**(8), L1561–L1564 (1990).

382. J.-M. Mariotti and S. T. Ridgway, "Double Fourier spatio-spectral interferometry: combining high spectral and high spatial resolution in the near infrared," *Astron. Astrophys.* **195,** 350–363 (1988).

383. S. T. Ridgway, J.-M. Mariotti, "A Method for Multispectral Infrared Interferometry," *Proc. 1st ESO/NOAO Workshop High Angular Resolution Imaging from the Ground Using Interferometric Techniques,* J. Goad, Ed., NOAO, 93–96 (1987).

References for Section 1.4

384. S. A. Hovanassian, "Introduction to Synthetic Array and Imaging Radars, Artech House, Dedham, MA (1980).

385. W. M. Brown and J. L. Porcello, "An introduction to synthetic aperture radar," *IEEE Spectrum* **6,** 52 (1969).

386. J. L. Walker, "Range-Doppler imaging of rotating objects," *IEEE Trans, Aerospace Electron. Syst.* **AES-16,** 23–52 (1980).

387. M. Born and E. Wolf, "Interference and diffraction with partially coherent light," Chap. 10 in *Principles of Optics,* 5th ed., Pergamon Press, New York (1975).

388. J. B. Breckinridge, "A white light amplitude interferometer with 180° rotational shear," *Opt. Eng.* **17,** 156–159 (1978).

389. K. Itoh and Y. Ohtsuka, "Interferometric imaging of a thermally luminous two-dimensional object," *Opt. Comm.* **48,** 75–79 (1983).

390. C. Roddier, F. Roddier, and J. Demarcq, "Compact rotational shearing interferometer for astronomical applications," *Opt. Eng.* **28,** 66–70 (1989).

391. E. B. Fomalont, "Earth-rotation aperture synthesis," *Proc. IEEE* **61,** 1211–1218 (1973).

392. A. M. Tai, "Passive synthetic aperture imaging using an achromatic grating interferometer," *Appl. Opt.* **25,** 3179–3190 (1986).

References for Section 1.5

393. J. W. Goodman, *Introduction to Fourier Optics,* McGraw-Hill, San Francisco (1968).

394. J. W. Goodman, "Wavefront-reconstruction imaging of coherently illuminated objects," Chap. 4 in *Restoration of Atmospherically Degraded Images,* Woods Hole Summer Study, National Academy of Sciences/NRC, Washington, D.C. (1966).

395. J. W. Goodman, "Analysis of wavefront reconstruction imaging through random media," Appendix 29 in *Restoration of Atmospherically Degraded Images,* Vol. 2, Woods Hole Summer Study, National Academy of Sciences/NRC, Washington, D.C. (1966).

396. J. W. Goodman, "Holographic arrays," Appendix 22 in *Restoration of Atmospherically Degraded Images,* Woods Hole Summer Study, National Academy of Sciences/NRC, Washington, D.C. (1966).

397. J. W. Goodman, "Statistical properties of laser speckle patterns," Chap. 2 in *Laser Speckle and Related Phenomena,* 2nd ed., J. C. Dainty, Ed., Springer-Verlag, New York (1984).

398. M. Born and E. Wolf, *Progress in Optics,* MacMillan, New York (1964).

399. E. N. Leith and J. Upatnieks, "Reconstructed wavefronts and communication theory," *J. Opt. Soc. Am.* **52,** 1123–1130 (1962).

400. P. S. Idell, J. D. Gonglewski, D. G. Voeltz, and J. Knopp, "Image synthesis from nonimaged laser-speckle patterns: experimental verification," *Opt. Lett.* **14,** 154–156 (1989).

401. T. R. Crimmins, J. R. Fienup, and B. J. Thelen, "Improved bounds on object support from autocorrelation support and application to phase retrieval," *J. Opt. Soc. Am. A* **7,** 3–13 (1990).

402. J. R. Fienup, T. R. Crimmins, and W. Holsztynski, "Reconstruction of the support of an object from the support of its autocorrelation," *J. Opt. Soc. Am.* **72,** 610–624 (1982).

403. J. C. Dainty and J. R. Fienup, "Phase retrieval and image reconstruction for astronomy,"

Chap. 7 in *Image Recovery: Theory and Application*, H. Stark, Ed., pp. 231–275, Academic Press, New York (1987).

404. J. R. Fienup, "Reconstruction of a complex-valued object from the modulus of its Fourier transform using a support constraint," *J. Opt. Soc. Am. A* **4,** 118–123 (1987).
405. R. G. Paxman, J. R. Fienup, and J. T. Clinthorne, "Effect of tapered illumination and Fourier intensity errors on phase retrieval," in *Digital Image Recovery and Synthesis, Proc. SPIE* **828,** 184–189 (1987).
406. J. R. Fienup and A. M. Kowalczyk, "Phase retrieval for a complex-valued object by using a low-resolution image," *J. Opt. Soc. Am. A* **7,** 450–458 (1990).
407. R. W. Gerchberg and W. O. Saxton, "A practical algorithm for the determination of phase from image and diffraction plane pictures," *Optik* **35,** 237–246 (1972).
408. J. R. Fienup, "Phase retrieval algorithms: a comparison," *Appl. Opt.* **21,** 2758–2769 (1982).
409. P. S. Idell and J. D. Gonglewski, "Image synthesis from wave-front sensor measurements of a coherent diffraction field," *Opt. Lett.* **15,** 1309–1311 (1990).
410. L. I. Goldfischer, "Autocorrelation function and power spectral density of laser-produced speckle patterns," *J. Opt. Soc. Am.* **55,** 247–253 (1965).
411. M. Elbaum, et al., "Laser correlography: transmission of high-resolution object signatures through the turbulent atmosphere," Riverside Research Institute Report T-1/306-3-11 (Oct. 31, 1974). (Available from NTIS, Report AD-A013-424.)
412. P. S. Idell, J. R. Fienup, and R. S. Goodman, "Image synthesis from nonimaged laser speckle patterns," *Opt. Lett.* **12,** 858–860 (1987).
413. J. R. Fienup and P. S. Idell, "Imaging correlography with sparse arrays of detectors," *Opt. Eng.* **27,** 778–784 (1988).
414. J. W. Goodman, *Statistical Optics*, John Wiley & Sons, New York (1985).
415. R. Hanbury Brown and R. Q. Twiss, "Correlation between photons in two coherent beams of light," *Nature* **177,** 27–29 (1956).
416. C. W. Helstrom, "Image restoration by the method of least squares," *J. Opt. Soc. Am.* **57,** 297–303 (1967).
417. D. G. Voelz, J. D. Gonglewski, and P. S. Idell, "Image synthesis from nonimaged laser-speckle patterns: comparison of theory, computer simulation, and laboratory results," *Appl. Opt.* **30,** 3333–3344 (1991).
418. P. J. Napier, R. T. Thompson, and R. D. Ekers, "The very large array: design and performance of a modern synthesis radio telescope," *Proc. IEEE* **71,** 1295–1320 (1983).
419. K. O'Donnell, "Time-varying speckle phenomena in astronomical imaging and in laser scattering," PhD Thesis, University of Rochester, Rochester, NY (1983).

References for Section 1.6

420. D. A. Ausherman, A. Kozma, J. L. Walker, H. M. Jones, and E. C. Pozzio, "Developments in radar imaging," *IEEE Transactions on Aerospace and Electronic Engineering* **AES-20**(4) (July 1984).
421. J. C. Curlander and R. N. McDonough, *Synthetic Aperture Radar Systems and Signal Processing*, John Wiley & Sons, New York (1991).
422. A. W. Rihaczek, *Principles of High-Resolution Radar*, Peninsula Publishing, Los Altos, CA (1985).
423. C. E. Cook and N. Bernfield, *Radar Signals*, Academic Press, New York (1967).
424. G. W. Deley, "Waveform design," Chapter 3 in *Radar Handbook*, 1st ed., M. I. Skolnik, Ed., McGraw-Hill, New York (1970).
425. C. C. Aleksoff and C. R. Christensen, "Holographic Doppler imaging of rotating objects," *Applied Optics* **14**(1) (January 1975).
426. C. C. Aleksoff et al., "Synthetic aperture imaging with a pulsed CO_2 TEA Laser," *Proceedings SPIE Laser Radar II* **783,** 29–40 (May 1987).
427. A. L. Kackelmyer, "Range-Doppler imaging: Waveforms and receiver design," *Proceedings SPIE Laser Radar III* **999,** 138–161 (September 1988).
428. A. L. Kackelmyer, "Coherent laser radar performance in the presence of random and systematic errors," *Proceedings SPIE Laser Radar III* **999,** 176–191 (September 1988).

(blank page)

APPENDIX B

J.R. Fienup, A.M. Kowalczyk and J.E. Van Buhler, "Phasing Sparse Arrays of Heterodyne Receivers," presented in Orlando, Fla., and published in Proc. SPIE 2241-15, Inverse Optics III (April 1994), pp. 127-131.

Phasing Sparse Arrays of Heterodyne Receivers

J.R. Fienup, A.M. Kowalczyk and J.E. Van Buhler
Optical & IR Science Laboratory
Environmental Research Institute of Michigan
P.O. Box 134001, Ann Arbor, MI 48113-4001

Abstract:

We describe two new methods for phasing arrays of heterodyne receivers. Both can be used when the arrays are sparse and distributed. One is based on the iterative transform algorithm using a support constraint and the other on maximizing image sharpness. Both work well: they require a modest number of speckle realizations with the same aberrations and are relatively immune to measurement noise.

In **Inverse Optics III**, Proc. SPIE **2241**-15 (Orlando, FL, 4-8 April 1994).

Phasing sparse arrays of heterodyne receivers

J.R. Fienup, A.M. Kowalczyk and J.E. Van Buhler

Optical & IR Science Laboratory
Environmental Research Institute of Michigan
P.O. Box 134001, Ann Arbor, MI 48113-4001

ABSTRACT

We describe two new methods for phasing arrays of heterodyne receivers. Both can be used when the arrays are sparse and distributed. One is based on the iterative transform algorithm using a support constraint and the other on maximizing image sharpness. Both work well: they require a modest number of speckle realizations with the same aberrations and are relatively immune to measurement noise.

1. INTRODUCTION

If we measure an optical field, scattered from a laser-illuminated object, with an array of heterodyne receivers,[1] then we can reconstruct an image of the object by performing a suitable propagation transformation (typically a Fresnel or Fourier transform) in the computer.[2] However, if phase errors are present in the measurements, then a blurred image will result. Phase errors can be induced by many things, including atmospheric turbulence and path-length errors between the field from the object and the local oscillator within the receiver. Approaches to phasing the array without a beacon either require the array of heterodyne receivers to be on a filled regular grid,[3,4] or to have a special pattern or alternatively require a low-resolution image be available.[5]

In this paper we describe two new algorithms for phasing heterodyne arrays that work well for sparse distributed arrays (and will work for filled arrays as well), requires no low-resolution image, and is relatively insensitive to noise. One is based on the iterative transform algorithm using a support constraint[6,7] and the other on maximizing image sharpness.[8,9]

2. IMAGING MODEL

We measure the optical fields (ignoring measurement noise)

$$G_{dk}(u) = F_k(u)\ \exp[i\phi_e(u)]\ , \tag{1}$$

for k = 1, ... , K, where F_k is the ideal complex field (without phase errors) for realization k, ϕ_e is the phase error, and u is a 2-D coordinate (the pixel index) in the measurement plane. Note that we assume the phase error is the same for all K realizations. Different speckle realizations are obtained if the object rotates slightly or translates. If we estimate the phase error as $\phi(u)$, then our estimates of the optical fields are

$$G_k(u) = G_{dk}(u)\ \exp[-i\phi(u)] \tag{2}$$

our coherent images are

$$g_k(x) = \mathcal{F}^{-1}[G_k(u)] = N^{-2}\sum_u G_k(u)\exp(i2\pi u\cdot x/N) \ , \tag{3}$$

where u·x is a vector dot (inner) product, and our speckle-reduced averaged image is

$$g_I(x) = K^{-1}\sum_k |g_k(x)|^2 \ , \tag{4}$$

where summation over k is for k = 1, ..., K.

3. ITERATIVE TRANSFORM ALGORITHM

Our first method to estimate the phase error is a generalization of the iterative transform algorithm.[6] In summary, one iteration of the generalized algorithm consists of the following steps:

(1) Calculate the Fourier estimates: $G_k(u) = G_{dk}(u)\exp[-i\phi(u)]$ (for k = 1 ... K).
(2) Inverse FFT them to compute the $g_k(x)$.
(3) Apply the support constraint: $g_{sk}(x) = s(x)\ g_k(x)$.
(4) FFT to compute the $G_{sk}(u)$.
(5) Compute a new phase-error estimate: $\phi(u) = \arg\{\sum_k G_{dk}(u)\ G^*_{sk}(u)\}$.

For the initial iteration the phase error estimate is zero. The support constraint can be known *a priori*, estimated from the autocorrelation support (which can be calculated from the given data),[10,11] or estimated from $g_I(x)$. To estimate the support from $g_I(x)$, the current estimate of the averaged image, we could smooth it, giving $s(x) = w(x) * g_I(x)$, and possibly threshold it. The smoothing function, w(x) could be, for example, a uniform disk having a radius of a few pixels. The new phase-error estimate, $\phi(u)$, given in step 5 is like a weighted average of the difference in phase between $G_{dk}(u)$, the measured data, and $G_{sk}(u)$, the current estimate of optical fields constrained by the image support constraint.

Steps (2) to (4) can also be performed by a direct convolution in the measurement plane:

$$G_{sk}(u) = G_k(u) * S(u) = \sum_{u_1} S(u_1)\ G_k(u - u_1) \ , \tag{5}$$

where $S(u) = \mathcal{F}[s(x)]$, which would be faster to compute for the case of sparse arrays.

4. MAXIMIZING SHARPNESS

The second approach is to find the phase-error estimate $\phi(u)$ which maximize the sharpness,

$$S_1 = \sum_x [g_I(x)]^2 = \sum_x [\sum_k |g_k(x)|^2]^2 \ , \tag{6}$$

of the image estimate. Alternatively, we can maximize S_{1W}, a weighted version of the sharpness, based on a filtered version of the averaged image,

$$g_{IW}(x) = \mathcal{F}^{-1}\{W(u)\ \mathcal{F}[g_I(x)]\} \tag{7}$$

where W(u) is a weighting function (for example, a Wiener filter).

We maximize the sharpness using a standard nonlinear optimization technique which we make computationally efficient by using an analytic expression for the gradient of the sharpness with respect to the phase-error estimate:

$$\frac{\partial S_{1W}}{\partial \phi(u)} = 4N^{-2}\ \mathrm{Im}\{\sum_k G_k(u)\ (G_k(u) * [G_I W^2])^*\}\ , \tag{8}$$

where $G_I(u) = \mathcal{F}[g_I(x)]$.

We can show that the error-reduction[6] version of our generalized iterative transform algorithm is similar in effect to a steepest-descent gradient search to maximize sharpness with a fixed step size. However, we in practice use a more powerful gradient search algorithm, such as conjugate-gradient, and we can use a more powerful version of the iterative transform algorithm as well, such as hybrid input-output.[6]

5. IMAGE RECONSTRUCTION EXAMPLE

Figure 1 shows a computer simulation example of phasing an array of sparse, distributed heterodyne receivers. Figure 1(a) shows the object, consisting of a block of 2×3 pixels and three separated points, embedded in a 64×64 array. We created complex-valued speckled images by replacing each pixel in the object by a circular complex Gaussian random number with variance equal to the square root of the original pixel value; Fourier transforming, multiplying by the a sparse aperture, and inverse transforming to produce the image. The sparse aperture we used for this experiment has 21 pixels within a 8×8 area, which is shown in Figure 1(b), magnified by a factor of four (only the central 16×16 pixels in its 64×64 array are shown). This sub-aperture pattern was designed by a genetic-based algorithm by P. Henshaw.[12] An average of ten such diffraction-limited speckled images is shown in Figure 1(c). Figure 1(d) shows a Wiener-Helstrom[13] filtered version of the averaged image, from which one can discern the major parts of the image. Figure 1(e) shows the blurred averaged image that resulted when we added, to the Fourier transform, random phase errors that were uniformly distributed Gaussian random numbers with standard deviation π radians. Figure 1(f) shows the averaged image corrected by the image sharpening algorithm and Figure 1(g) shows a Wiener-filtered version of the corrected image. The corrected image is clearly superior to the blurred image and strongly resembles the diffraction-limited image. We obtained comparable results using the generalized iterative transform algorithm. The algorithms usually produced images with better quality as the number of realizations increases. It was unreliable when using only one to four realizations. Tests with noise showed that the algorithm is not very sensitive to noise.

6. CONCLUSIONS

We have derived two new algorithms for phasing an array of heterodyne receivers, and have demonstrated that they can work well for sparse distributed arrays, require a modest number of speckle realizations, and are robust in the presence of measurement noise.

7. ACKNOWLEDGMENTS

This research was supported by the Innovative Science and Technology office of the Ballistic Missile Defense Organization through the Office of Naval Research.

8. REFERENCES

1. G.W. Kamerman, "Laser Radar," in *Active Electro-Optical Systems*, C.S. Fox, Ed., Vol. 6 of *The Infrared & Electro-optical Systems Handbook*, (ERIM, Ann Arbor, 1993), Chapter 1.

2. J.R. Fienup, "Unconventional Imaging Systems: Image Formation from Non-imaged Laser Speckle Patterns," in *Emerging Systems and Technologies*, S.R. Robinson, Ed., Vol. 8 of *The Infrared & Electro-optical Systems Handbook*, (ERIM, Ann Arbor, 1993), Chapter 1.5, pp. 92-109.

3. J.R. Fienup, J.N. Cederquist, J.C. Marron, T.J. Schulz and J.H. Seldin, "Heterodyne Array Phasing by Digital Shearing Laser Interferometry," in *IRIS Specialty Group on Active Systems Meeting Digest*, 16-18 October 1990.

4. J.N. Cederquist, J.R. Fienup, J.C. Marron, T.J. Schulz and J.H. Seldin, "Digital Shearing Laser Interferometry for Heterodyne Array Phasing," in *Laser Radar VI*, R.J. Becherer, ed., Proc. SPIE 1416 -43 (1991).

5. S.E. Clark and L.F. Desandre, "High Resolution Image Reconstruction from Sparse Random Arrays," in *Signal Recovery and Synthesis IV*, 1992 Technical Digest Series Vol. 11 (Optical Society of America), April 14-15, 1992, New Orleans. LA, pp. 75-77.

6. J.R. Fienup, "Phase Retrieval Algorithms: A Comparison," *Appl. Opt.* 21, 2758-2769 (1982).

7. J.R. Fienup, "Reconstruction of a Complex-Valued Object from the Modulus of Its Fourier Transform Using a Support Constraint," *J. Opt. Soc. Am. A* 4, 118-123 (1987).

8. R.A. Muller and A. Buffington, "Real-Time Correction of Atmospherically Degraded Telescope Images through Image Sharpening," *J. Opt. Soc. Am.* 64, 1200-1210 (1974).

9. R.G. Paxman and J.C. Marron, "Aberration Correction of Speckled Imagery with an Image-Sharpness Criterion," in *Statistical Optics*, Proc. SPIE 976 -05, San Diego, CA, August 1988.

10. J.R. Fienup, T.R. Crimmins, and W. Holsztynski, "Reconstruction of the Support of an Object from the Support of Its Autocorrelation," *J. Opt. Soc. Am.* 72, 610-624 (1982).

11. T.R. Crimmins, J.R. Fienup and B.J. Thelen, "Improved Bounds on Object Support from Autocorrelation Support and Application to Phase Retrieval," *J. Opt. Soc. Am. A* 7, 3-13 (1990).

12. P.D. Henshaw, "Genetic Algorithms for Unconventional Imaging," in *Inverse Optics III*, M.A. Fiddy, ed., Proc. SPIE 2242-34 (April 199).

13. C.W. Helstrom, "Image Restoration by the Method of Least Squares," *J. Opt. Soc. Am.* 57, 297-303 (1967).

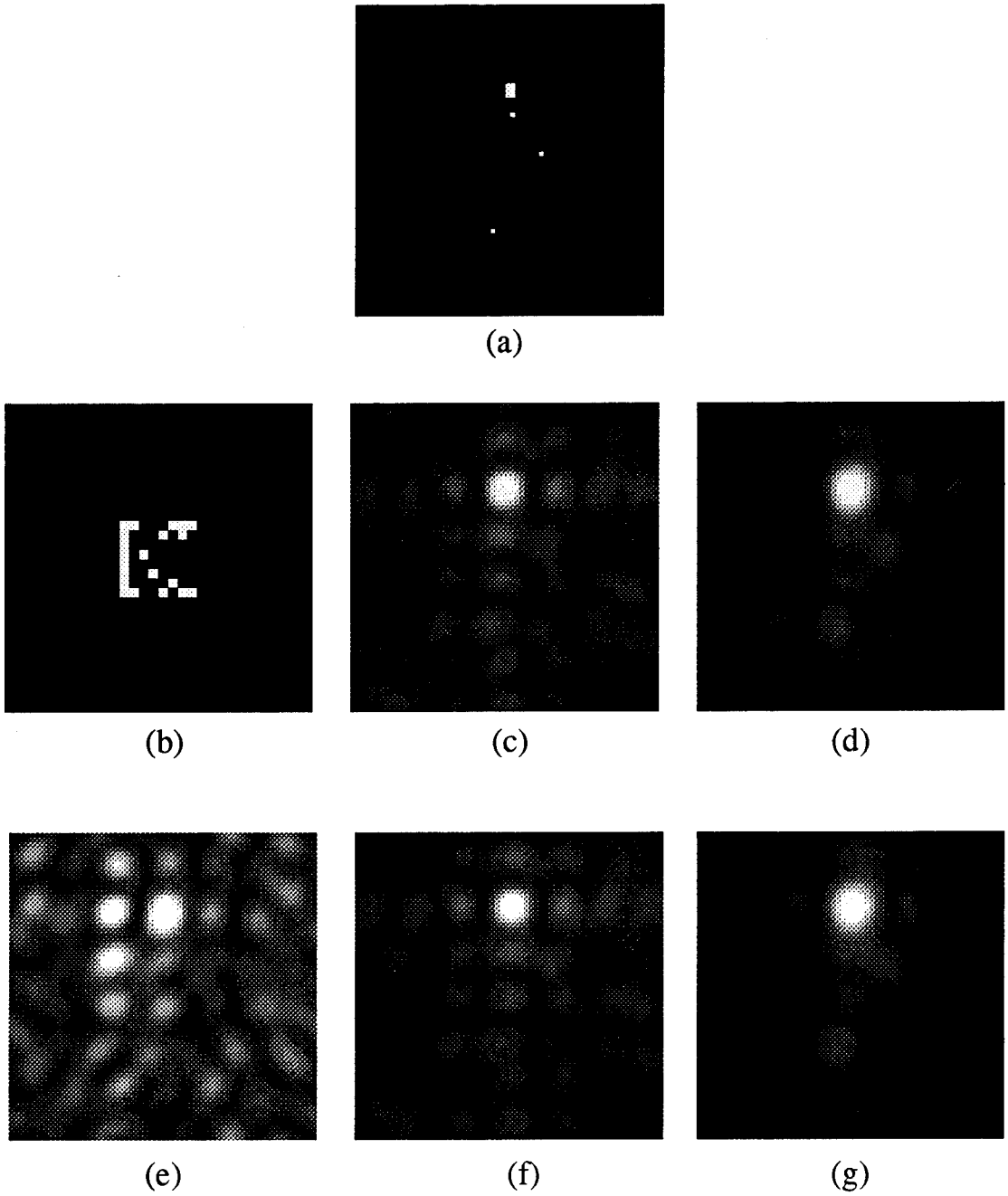

Figure 1. Computer Simulation of Sparse Heterodyne Array Phasing.
(a) Object; (b) 21-element sparse, distributed array (within an 8 x 8 -sample area); (c) average of ten diffraction-limited speckled images; (d) Wiener-filtered version of (c); (e) average of ten aberrated speckled images; (f) average of ten speckled images corrected by image-sharpening phase-up algorithm; (g) Wiener-filtered version of (f).

(blank page)

APPENDIX C

R.G. Paxman, J.H. Seldin, J.R. Fienup, and J.C. Marron, "Use of an Opacity Constraint in Three-Dimensional Imaging," presented in Orlando, FL, and published in Proc. SPIE 2241-14, Inverse Optics III (April 1994), pp. 116-126.

in *Inverse Optics III*, Proceedings of the SPIE **2241-14**, Orlando, FL (April, 1994).

Use of an opacity constraint in three-dimensional imaging

Richard G. Paxman, John H. Seldin, James R. Fienup, and Joseph C. Marron

Optical & Infrared Science Laboratory, Advanced Concepts Division
Environmental Research Institute of Michigan
P.O. Box 134001, Ann Arbor, Michigan 48113-4001
internet email: paxman@erim.org

ABSTRACT

Three-dimensional imaging provides profile information not available with conventional two-dimensional imaging. Many three-dimensional objects of interest are opaque to the illuminating radiation, meaning that the object exhibits surface, as opposed to volume, scattering. We investigate the use of an opacity constraint to perform three-dimensional phase retrieval. The use of an opacity constraint in conjunction with frequency-diverse pupil-plane speckle measurements to reconstruct a three-dimensional object constitutes a novel unconventional-imaging concept. This imaging modality avoids the difficulties associated with making phase measurements at a cost of increased computations.

1. INTRODUCTION

Marron and Schroeder [1,2] have demonstrated that three-dimensional imaging can be accomplished by sequentially illuminating an object with different laser frequencies and measuring the far-field speckle pattern for each of the illuminating frequencies [1]. In-phase and quadrature measurements provide optical-field values for the laser-speckle patterns. Properly formatted, these data form a three-dimensional Fourier-volume (or Fourier-aperture) representation of the illuminated object. A simple three-dimensional Discrete Fourier Transform (DFT) can be performed to provide a three-dimensional representation of the object. This three-dimensional lensless-imaging concept is referred to as Holographic Laser Radar (HLR).

The collection of HLR data could be considerably simplified if instead of collecting field measurements for the speckle images, intensity measurements were collected. Intensity measurements are straightforward and eliminate the need for interference with a reference beam with precision alignment, tracking, and phase stability. A multiple-frequency speckle-intensity data set would provide three-dimensional Fourier-magnitude information or, equivalently, the three-dimensional object autocorrelation. In order to recover a literal three-dimensional image, a phase-retrieval algorithm is required. Therefore, this proposed imaging concept trades complexity and cost in hardware for increased computing.

Phase retrieval requires some type of *a priori* information about the object. Two-dimensional complex-valued objects have been recovered using phase retrieval with a support constraint [3], although this is a challenging problem. It is well known that the uniqueness properties of two-dimensional phase retrieval are much better than for the one-dimensional problem [4]. We conjecture

that three-dimensional phase retrieval with a support constraint is better conditioned than its two-dimensional counterpart.

An additional constraint that has great promise in the three-dimensional imaging case is an *opacity* constraint. An opaque object is one that exhibits only surface scattering and no volume scattering (over volumes that extend beyond the desired range resolution). The reflectivity function for an opaque object is confined to a two-dimensional curved (possibly discontinuous) surface, embedded in a three-dimensional space. In this paper we explore the use of an opacity constraint to perform phase retrieval. We have previously used an opacity constraint to perform superresolution [5].

The opacity constraint is a special type of support constraint. It is a "quality of support" constraint – the actual location of the support is not given, although the object is known to be confined to a two-dimensional curved surface. This constraint promises to be very powerful since it greatly reduces the class of feasible objects from which to choose an estimate. Moreover, there are many imaging applications in which the objects will be known with confidence to be opaque. For example, space objects, balistic missiles, aircraft, and a multitude of industrial-inspection parts qualify as opaque objects. Most objects in our everyday experience satisfy the opaque condition. The constraint is invalid for objects with distributed volume scatterers such as translucent or fog-like objects.

The use of an opacity constraint in conjunction with frequency-diverse pupil-plane speckle measurements to reconstruct a three-dimensional object constitutes a novel unconventional-imaging concept.

2. REPRESENTATION OF OPAQUE OBJECTS

Consider a three-dimensional opaque object, $f(x,y,z)$, defined on an object-centered coordinate system. Let x and y be the cross-range (angle-angle) coordinates and let z be the range coordinate that is co-aligned with the illumination direction. Since the collected data will be sampled and since object reconstructions must be performed with a digital computer, we will adopt a discrete representation for the object. Accordingly, we require the coordinates (x,y,z) to take on integer values. Because of the opaque nature of the object, only radiation from reflecting sources in the illuminated surface will contribute to the received signal. Hidden surfaces do not contribute. Let $h(x,y)$ denote the height of the object in the z-dimension. Because the object is confined to a two-dimensional curved surface embedded in three-dimensional space, it can be represented with delta-function notation [5,6],

$$f(x,y,z) \;=\; r(x,y)\delta[z-h(x,y)]\;, \qquad x,y,z \in \{0,1,2,\ldots N-1\}\;, \tag{1}$$

where $r(x,y)$ is the complex surface reflectivity, N is the total number of samples in each dimension, and $\delta(\cdot)$ is used to represent the Kronecker delta,

$$\delta(z-z_o) \;\equiv\; \begin{cases} 1, & z=z_o \\ 0, & z\neq z_o \end{cases}\;. \tag{2}$$

Recall that the collected Fourier intensity data can be transformed to compute a three-dimensional object autocorrelation. In order to avoid aliasing, we require the object to have finite support with sufficient zero padding,

$$f(x,y,z) \;=\; 0\,, \qquad x,y,z \in \left\{\frac{N}{2}, \frac{N}{2}+1, \ldots, N-1\right\}\,. \tag{3}$$

The rectilinear object-support bound given in Eq. (3) is not likely to be a "tight" bound. More restrictive or tighter bounds on object support can be determined from the known object autocorrelation by using a generalization of methods developed for two-dimensional phase retrieval [7]. Any three-dimensional support bound can be expressed in terms of a two-dimensional angle-angle support bound and a one-dimensional range support bound that depends upon angle-angle position.

3. STATEMENT OF PROBLEM

The Fourier representation of the object is found with the DFT,

$$F(u,v,w) \;=\; \sum_{x=0}^{N-1}\sum_{y=0}^{N-1}\sum_{z=0}^{N-1} f(x,y,z)\exp\{-i2\pi(ux+vy+wz)/N\} \tag{4}$$

$$\;=\; \sum_{x=0}^{N-1}\sum_{y=0}^{N-1}\sum_{z=0}^{N-1} r(x,y)\delta[z-h(x,y)]\exp\{-i2\pi(ux+vy+wz)/N\} \tag{5}$$

$$\;=\; \sum_{x=0}^{N-1}\sum_{y=0}^{N-1} r(x,y)\exp\{-i2\pi[ux+vy+wh(x,y)]/N\}\,, \tag{6}$$

where we have used the Kronecker delta to eliminate the summation over z. Since we detect intensities in the Fourier domain, a noiseless measurement would be given by the squared modulus of the DFT of the object, $|F(u,v,w)|^2$. The actual detected data will be corrupted by noise. The detected data are represented by

$$D(u,v,w) \;=\; \mathcal{N}\{|F(u,v,w)|^2\}\,, \tag{7}$$

where the noise operator $\mathcal{N}\{\cdot\}$ corrupts the argument according to an appropriate noise model. Additive Gaussian or Poisson noise models are appropriate when detector readout noise or photon noise, respectively, are the dominant noise sources.

The problem that we wish to address can now be stated. Given the data, $D(u,v,w)$, estimate the object height function, $h(x,y)$, and the object surface reflectivity function, $r(x,y)$, over the angle-angle object-support bound. Performing such an estimate implicitly provides an estimate for the object's Fourier phase. Therefore this problem may be properly viewed as a phase-retrieval problem.

4. MAXIMUM-LIKELIHOOD ESTIMATION

When detector readout noise dominates, the noise operator has the effect of adding a realization of a Gaussian noise process,

$$D(u,v,w) \;=\; |F(u,v,w)|^2 + n(u,v,w)\,. \tag{8}$$

Assuming a common noise variance and statistical independence between differing samples of the noise process, it is straightforward to express the probability density function for the recorded data [8] . The associated log-likelihood function is readily found to be [8]

$$L[\hat{r}(x,y),\hat{h}(x,y)] = -\sum_{u=0}^{N-1}\sum_{v=0}^{N-1}\sum_{w=0}^{N-1}\left[D(u,v,w) - |\hat{F}(u,v,w)|^2\right]^2 \tag{9}$$

$$= -\sum_{u=0}^{N-1}\sum_{v=0}^{N-1}\sum_{w=0}^{N-1}\left[D(u,v,w) - \left|\sum_{x=0}^{N-1}\sum_{y=0}^{N-1}\hat{r}(x,y)\exp\{-i2\pi[ux+vy+w\hat{h}(x,y)]/N\}\right|^2\right]^2 , \tag{10}$$

where the caret symbol indicates an estimated quantity. Recall that the object surface reflectivity is complex valued. It is convenient to explicitly denote the real and imaginary parts of the reflectivity,

$$r(x,y) \;=\; r_r(x,y) + ir_i(x,y) \; . \tag{11}$$

We can use standard nonlinear optimization methods to search for $\hat{r}_r(x,y)$, $\hat{r}_i(x,y)$, and $\hat{h}(x,y)$ ($(x,y) \in$ the angle-angle object-support bound) that maximize the objective function, L, to yield a maximum-likelihood estimate. If the angle-angle object support bound is comprised of $N/2$ by $N/2$ samples, then L is defined on a parameter space of dimension $3N^2/4$. The range support bound that derives from the three-dimensional support bound could be used to constrain the search over $\hat{h}(x,y)$.

There are a variety of nonlinear optimization algorithms that could be used to maximize the log-likelihood function. One choice is the well-known conjugate-gradients algorithm [9]. As its name suggests, this algorithm makes use of the gradient of the objective function. We have derived closed-form expressions for the partial derivatives that constitute the gradient. These expressions afford a gradient computation that is more accurate and computationally much more efficient than would be rendered using the method of finite differences. The partial derivatives of the log-likelihood function with respect to the real and imaginary parts of the surface reflectivity and with respect to the height function, at the angle-angle location (x_o, y_o), are given by

$$\frac{\partial L}{\partial \hat{r}_r(x_o,y_o)} =$$

$$4\mathrm{Re}\left\{\sum_{u=0}^{N-1}\sum_{v=0}^{N-1}\sum_{w=0}^{N-1}\left[D(u,v,w) - |\hat{F}(u,v,w)|^2\right]\hat{F}^*(u,v,w)\exp\{-i2\pi[ux_o+vy_o+w\hat{h}(x_o,y_o)]/N\}\right\}, \tag{12}$$

$$\frac{\partial L}{\partial \hat{r}_i(x_o,y_o)} =$$

$$-4\mathrm{Im}\left\{\sum_{u=0}^{N-1}\sum_{v=0}^{N-1}\sum_{w=0}^{N-1}\left[D(u,v,w) - |\hat{F}(u,v,w)|^2\right]\hat{F}^*(u,v,w)\exp\{-i2\pi[ux_o+vy_o+w\hat{h}(x_o,y_o)]/N\}\right\}, \tag{13}$$

$$\frac{\partial L}{\partial \hat{h}(x_o, y_o)} = \frac{8\pi}{N} \mathrm{Im} \left\{ \hat{r}(x_o, y_o) \sum_{u=0}^{N-1} \sum_{v=0}^{N-1} \sum_{w=0}^{N-1} \left[D(u,v,w) - |\hat{F}(u,v,w)|^2 \right] \right.$$
$$\left. \hat{F}^*(u,v,w)\, w \exp\{-i2\pi[ux_o + vy_o + w\hat{h}(x_o, y_o)]/N\} \right\}, \quad (14)$$

where the operators $\mathrm{Re}\{\cdot\}$ and $\mathrm{Im}\{\cdot\}$ take the real and imaginary parts of the argument, respectively. Notice that these partial-derivative expressions each have the form of a two-dimensional DFT (over u and v) followed by a summation over w for each (x_o, y_o). This affords efficient evaluation the entire gradient using the Fast Fourier Transform (FFT). The three-dimensional function $\hat{F}(u,v,w)$ must be computed to evaluate the objective function and the gradient. We find that N two-dimensional FFTs are needed to compute $\hat{F}(u,v,w)$. Careful examination of Eqs. (12)−(14) reveals that the entire gradient can be computed with an additional N two-dimensional FFTs followed by $2SN^2$ summations over w, where S is the proportion of pixels in the angle-angle object support relative to the number of samples in the total angular field of view. In the case of the rectilinear support expressed in Eq. (3), $S = 1/4$. Of course additional computational overhead is required to perform complex multiplies and sums. Closed-form expressions for the log-likelihood and its gradient can also be derived for the case of photon noise.

5. SIMULATIONS

We have performed two simulations that demonstrate three-dimensional phase retrieval using an opacity constraint. For both of the simulations we chose $N = 32$ and a maximum object extent of 16 samples in each dimension, as required by Eq. (3). This guarantees that the Fourier-intensity data are adequately sampled. In addition, for this initial demonstration we used noiseless Fourier-intensity data, giving $n(u,v,w) = 0$ in Eq. (8).

The first simulation utilized a simple object consisting of 6 separated points of equal reflecting strength. The angle-angle (x-y) view of the magnitude of the surface reflectivity is shown in Figure 1(A). The phases of these points are independent, identically-distributed samples from a probability distribution function (PDF) that is uniformly distributed on the interval $[0, 2\pi]$. The height distribution and reflectivity of these points are summarized in Table 1. Coordinates are referenced from $(0,0)$ in the upper left corner. Despite the discrete representation of the object in the x and y dimensions, the z-dimension heights, $h(x,y)$, are not restricted to integer values.

The phase-retrieval problem consists of estimating a set of real-valued quantities, $r_r(x,y)$, $r_i(x,y)$, and $h(x,y)$, defined on a discrete (x,y) coordinate system. The conjugate-gradients algorithm, used to estimate the object parameters, is initiated with a first guess of the unknown parameters. We began with an initial estimate of $h(x,y) = 0$ and independent, identically distributed samples from a PDF that is uniform on the interval $[0,1]$ for $r_r(x,y)$ and $r_i(x,y)$. The magnitude and phase of the initial reflectivity guess are shown in Figures 1(B) and 1(C), respectively. The magnitude of the initial reflectivity guess ranges between 0.083 and 1.34, and the phase varies from 0.001 to 1.567 radians. By restricting the initial guess of $r_r(x,y)$ and $r_i(x,y)$ to positive

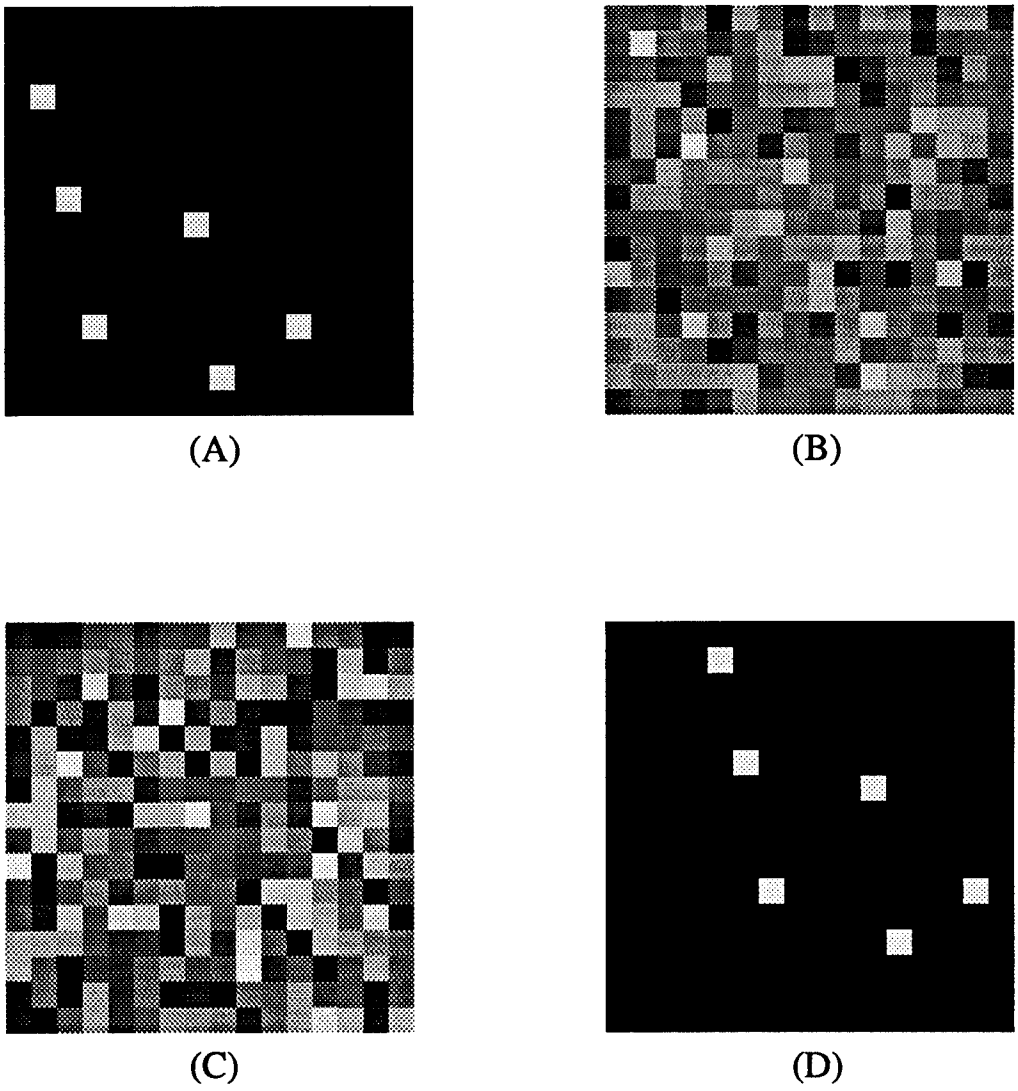

Figure 1. 6-point object simulation. (A) Angle-angle (x-y) view of the magnitude of the reflectivity of a 6-point, complex-valued object; (B) Magnitude of the initial reflectivity estimate; (C) Phase of the initial reflectivity estimate; (D) Reconstructed object.

(x,y)	$r_r(x,y)$	$r_i(x,y)$	$h(x,y)$
(1,3)	-0.976	0.216	0.0
(2,7)	0.411	0.911	0.3
(7,8)	0.994	0.111	0.9
(3,12)	-0.988	0.153	1.5
(8,14)	0.745	-0.666	2.1
(11,12)	0.089	0.996	3.0

Table 1: 6-Point Object Description.

values, we have reduced the chance of biasing the simulation by starting too close to the true solution. No *a priori* knowledge of the support of the unknown object was used during the estimation of its reflectivity and height distribution, so a total of $16 \times 16 \times 3 = 768$ parameters were estimated simultaneously.

The angle-angle view of the estimated reflectivity magnitude after about 400 iterations of the conjugate-gradients algorithm is shown in Figure 1(D). The reconstruction is virtually perfect, and is limited only by computational precision. There are several features of the reconstruction to note. First, the reconstructed object is shifted from its true location. A feature of all phase retrieval algorithms is a translation ambiguity among the set of valid object solutions. A translation of the object adds a linear phase term to the complex-valued Fourier transform, but does not affect the Fourier intensity. There is also a 180-degree object-rotation ambiguity. Such a rotation gives rise to a Fourier transform that is the complex-conjugate of the original Fourier transform, but which leaves the Fourier intensity unchanged.

The height estimates were also virtually perfect. It is of interest that the non-integer height values were estimated very accurately, indicating that in addition to phase retrieval, we were accomplishing superresolution in range. Not only is the object estimate translated in (x,y), but it is also translated in the z direction by a constant value of -1.2. Also, whereas the magnitude of the estimated reflectivity matches the true reflectivity, the phase of the estimate differs by the constant value of 0.64 radians at each point. This is yet another ambiguity associated with the phase retrieval of complex-valued objects. A constant phase bias across the object, however, is typically irrelevant.

For the case of noiseless Fourier-intensity measurements we have shown that an array of points with a modest height distribution can be reconstructed perfectly with no *a priori* knowledge about the support or height distribution of the points, except for the use of an opacity constraint. We have, however, found that the conjugate-gradients algorithm is subject to stagnation in what we believe to be local extrema in the log-likelihood function, and a successful reconstruction was obtained only after several random initial guesses for the reflectivity. Also, we have observed that the relative distribution of the points in the z-dimension has a bearing on the success of the reconstruction. We chose a distribution over a range of 3 samples, and we have noted that as this range is expanded, stagnation becomes more likely when using a naive initial guess of $h(x,y) = 0$. Thus, we believe

that the development of methods that yield improved initial estimates and support bounds that will constrain the range of height parameters will be important for successful reconstructions for surfaces that have large variation in depth. Our second simulation provides an example of how such a height constraint could be derived and utilized.

The second simulation example involves an object that is a curved surface with an angle-angle (x-y) support that is a 5×5-pixel right triangle. To simplify the height distribution, we made the height of the object a function of the x-dimension alone. The support of the object projected in each of the 3 directions is shown in Figure 2. When the object is projected in the y-direction, we obtain a single pixel of z-direction support for each position in the x dimension, as illustrated in Figure 2(A). We conclude from this that the height is constant in y for each x and is symmetric about the $x = 8$ plane. The height of the object varies over a 5-pixel interval, with a 2-pixel height gap between the x-dimension edges and their neighbors.

If no support constraint is used along with a naive initial guess of $h(x, y) = 0$, the parameter estimation stagnates and the object cannot be reconstructed. Thus, the reconstruction of this more complicated object might benefit from a support constraint. Techniques for bounding the object support using the autocorrelation support have been developed for two-dimensional phase-retrieval problems [7]. We can apply these same techniques to the support of the three-dimensional autocorrelation projected into 2 dimensions in each of the 3 directions. Unfortunately, in doing so we lose registration information between the 3 resulting 2-D support constraints and, thus, cannot merge these results into a tight 3-D support constraint. However, for this particular object for which the height is constant along the y-direction, the triple-intersection rule [7] applied to the support of the y-projected autocorrelation yields the exact z-support shown in Figure 2(A). This somewhat surprising result suggests that opacity could be extremely useful in finding support bounds. The derived height support in turn yields the true solution for the height and indicates that the x-dimension support is 5-pixels wide. Merging this information with the support of the autocorrelation projected along the z-direction into the x-y plane yields the x-y object support bound shown in Figure 3(A). This bound could further be reduced using a two-point intersection rule, but we found that this was not necessary.

The magnitude of the reflectivity of the true object is shown in Figure 3(B). The initial guess for the reflectivity is found in Figure 3(C), and the initial guess for the height was set to the values yielded from the x-z support derived from the triple-intersection of the projected autocorrelation. The initial guess of the height was set constant in the y-direction over the support defined in Figure 3(A). The x-y support constraint reduces the number of parameters to be estimated to 114. After approximately 800 iterations of the conjugate-gradients algorithm, the estimates were perfect to within the limits of computational precision. Despite our knowledge of the height from the support estimate, we still allowed the height estimates to vary during minimization. The final estimates actually moved a fixed distance from their initial settings, but remained constant in the y-direction. The final estimate of the reflectivity is shown in Figure 3(D), and is essentially identical to the true reflectivity in Figure 3(B).

Although it is unlikely that the height of the object can be estimated directly from the projected

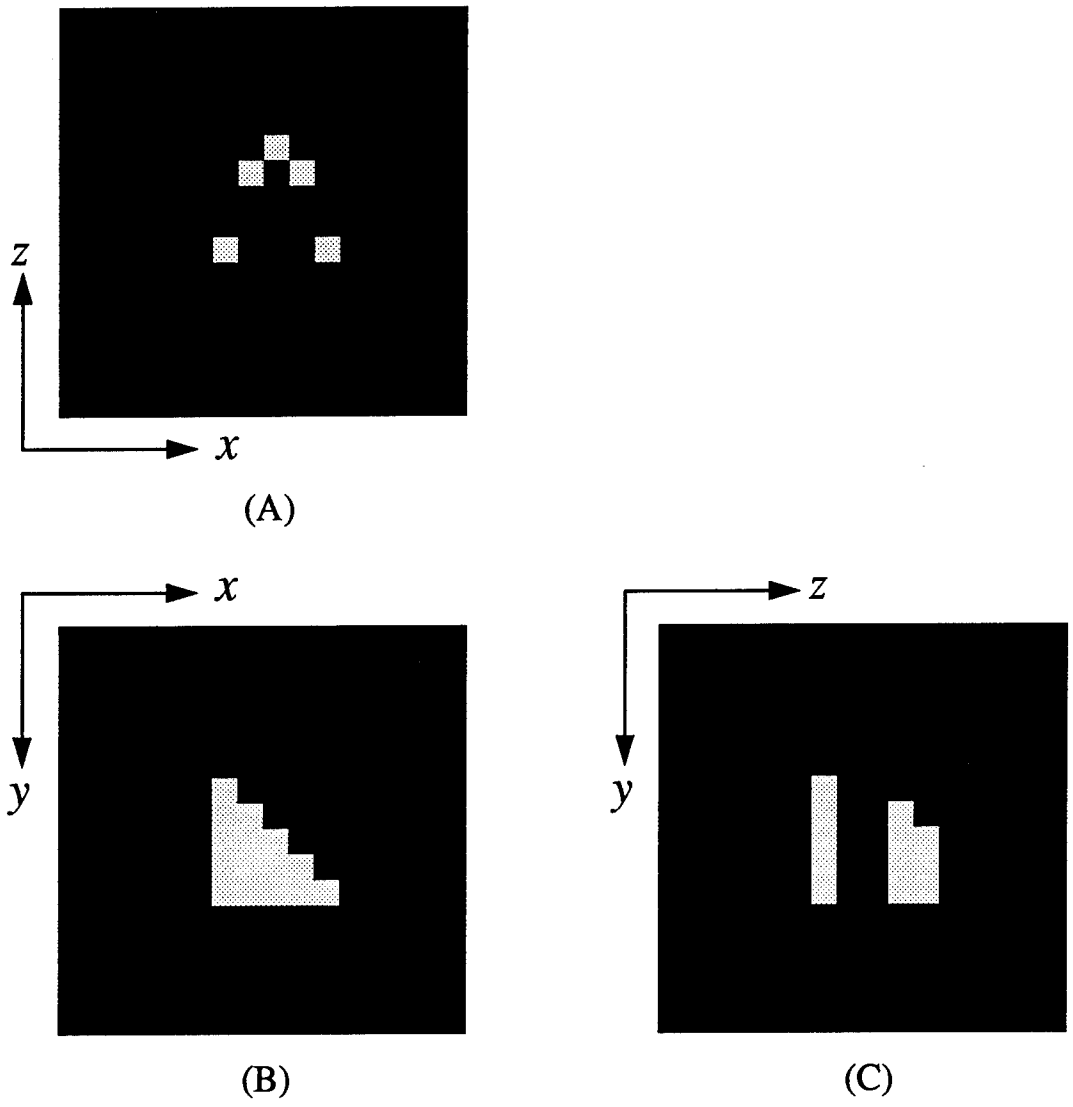

Figure 2. Three views of the support of a triangular curved surface. (A) x-z view of the surface. From this view we see that the height distribution is the same for every value of y and is symmetric about the x=8 plane; (B) x-y view of the surface; (C) y-z view of the surface.

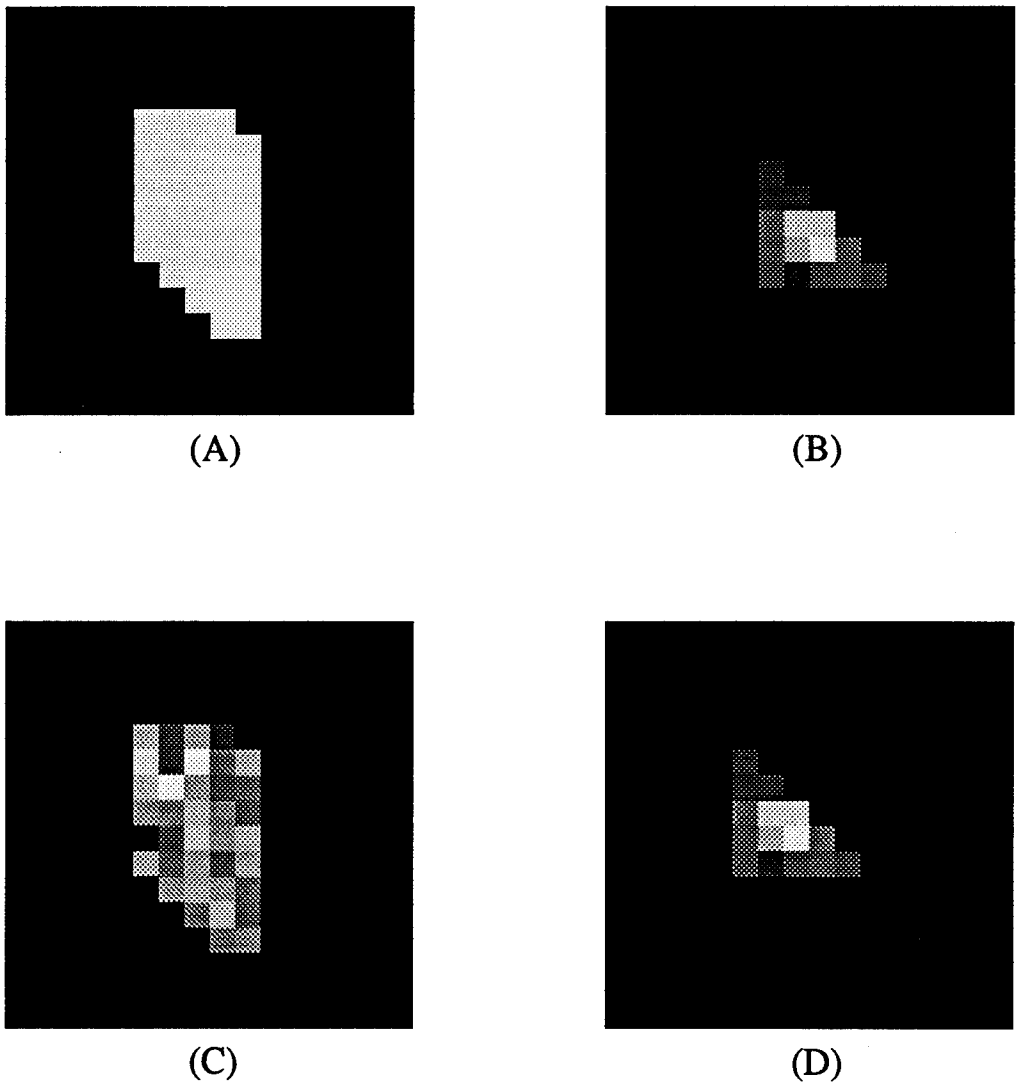

Figure 3. Reconstruction of triangular curved surface. (A) x-y support bound. The bound was obtained by intersecting the estimated x-z support bound [same as shown in Figure 2(A)] with the x-y autocorrelation support; (B) Magnitude of the true reflectivity; (C) Magnitude of the initial guess on the support of (A); (D) Magnitude of reconstructed reflectivity.

autocorrelation in practical scenarios involving measurement noise and 2-D height variation (instead of the 1-D variation of this example), this example demonstrates that a filled surface reflectivity can be estimated with a loose angle-angle support.

6. CONCLUSIONS

We have reported the first demonstration of three-dimensional phase retrieval with an opacity constraint. These results make feasible the possibility of an entirely new three-dimensional imaging modality. Further experimentation is required to determine how loose the height constraint can be made and the importance of the role of the initial height estimate. We believe that the theory of two-dimensional support bounds [7] can be generalized to the three-dimensional case to give good support bounds. We also conjecture that opacity will play a role to help tighten range-dimension support bounds. Historically modes of stagnation have been studied in the two-dimensional phase-retrieval problem and appropriate algorithms to avoid such modes have been developed. A similar process needs to be undertaken in the three-dimensional case. Finally, the sensitivity of three-dimensional phase retrieval to noise needs to be investigated.

7. ACKNOWLEDGEMENTS

We wish to recognize Stanley R. Robinson who originally suggested that the opacity constraint be considered for use in phase-retrieval. We are also grateful for useful discussions with Brian J. Thelen. This research was supported by the Innovative Science and Technology office of the Ballistic Missile Defense Organization of the Office of Naval Research.

REFERENCES

1. J.C. Marron and K.S. Schroeder, "Three-dimensional lensless imaging using laser frequency diversity," Appl. Opt. **31**, 255-262 (1992).
2. J.C. Marron and K.S. Schroeder, "Holographic Laser Radar," Opt. Lett. **18**, 385-387 (1993)
3. J.N. Cederquist, J.R. Fienup, J.C. Marron, and R.G. Paxman, "Phase retrieval from experimental far-field speckle data," Opt. Lett. **13**, 619-621 (1988).
4. J.C. Dainty and J.R. Fienup, "Phase Retrieval and Image Reconstruction for Astronomy," in Image Recovery: Theory and Application, H. Stark, ed. (Academic Press, New York, 1987).
5. R.G. Paxman, "Superresolution with an opacity constraint," *Topical Meeting on Signal Recovery and Synthesis III*, Technical Digest Series **15**, (Optical Society of America, Washington DC, 1989), PD1, North Falmouth, Cape Cod, MA, June 1989.
6. N. Bleistein, *Mathematical Methods for Wave Phenomena* (Academic Press, New York, 1984).
7. T.R. Crimmins, J.R. Fienup, and B.J. Thelen, "Improved bounds on object support from autocorrelation support and application to phase retrieval," J. Opt. Soc. Am. A **7**, 3-13 (1990).
8. R.G. Paxman, T.J. Schulz, and J.R. Fienup, "Joint estimation of object and aberrations by using phase diversity," J. Opt. Soc. Am. A **9**, 1072-1085 (1992).
9. D.C. Luenberger, *Linear and Nonlinear Programming* (Addison-Wesley, Reading, MA, 1984).

APPENDIX D

J.C. Marron and R.G. Paxman, "Pulsed Heterodyne-Array Imaging," presented in Orlando, FL, and published in Proc. SPIE 2241-13, Inverse Optics III (April 1994), pp. 111-115.

Presented at the SPIE Inverse Optics Meeting, Orlando Florida, April 4-5, 1994.

Pulsed Heterodyne-Array Imaging

Joseph C. Marron and Richard G. Paxman

Environmental Research Institute of Michigan
P. O. Box 134001
Ann Arbor MI, 48113-4001

Abstract

We discuss a 3-D imaging modality called Pulsed Heterodyne-array Imaging (PHI). The relationship between PHI and stepped-frequency methods for 3-D coherent image formation is derived. For both cases, we consider flood-illumination of the object and detection with a 2-D array of coherent receivers located in the pupil plane. It is shown that PHI can recover the same coherent 3-D image as with a stepped-frequency method such as holographic laser radar [1].

1.0 Introduction

In previous research, we have demonstrated the ability to form 3-D coherent images by flood-illuminating an object with a tunable laser and detecting the scattered light with a 2-D array of coherent (field-recording) receivers. As the source frequency is tuned, the optical field is recorded and a 3-D image is formed by 3-D Fourier transformation of the data. We refer to this method as Holographic Laser Radar (HLR).

The basis for HLR imaging is the 3-D Fourier Transform relationship between the optical field, U, and the object's 3-D complex reflectivity function, $\sigma(r)$. This relationship can be written as [2-4]

$$U(r_d, \omega) = \alpha \, exp(ikR) \int \sigma(r) \, exp[-i\omega(\rho \cdot r)] \, d^3r \quad , \tag{1}$$

where r_d is the unit vector corresponding to the location of a detector element with respect to the object domain origin ($r = 0$), ω is the source angular frequency, α is an inessential complex constant, R is the distance from the source to the object domain origin to the detector, and $\rho = (r_s + r_d)/c$, where c is the speed of light and r_s is the unit vector corresponding to the source location with respect to $r = 0$. For HLR, data is recorded for a series of r_d values as the source frequency is tuned. For this reason Eq. (1) is written as a function of these two variables, r_d and ω.

By using Eq. (1), we have been able to demonstrate fine-resolution 3-D coherent imaging [5]. For these experiments we used a tunable dye laser and a 256 X 256 coherent detector array. A 3-D DFT was used for image formation and range resolution on the order of 10μm was reported.

2.0 Pulsed Heterodyne-Array Imaging

Now consider 3-D image formation with pulsed illumination. This imaging modality has been discussed previously [6]; however, in this paper we present the underlying theory for image formation and analyze it in the context of stepped-frequency imaging. To begin this analysis consider the output of a mode-locked laser. A mode-locked laser coherently phases longitudinal cavity modes of the laser to produce a series of short pulses. In frequency space the output can be written as

$$A(\omega) = [comb(a\omega) \cdot rect(b\omega)] \otimes \delta(\omega - \omega_0), \tag{2}$$

where $\otimes$ represents a convolution and δ represents the Dirac delta function. To simplify the expression we have assumed that the modes all have the same phase, however, this treatment extends readily to the more general case of linear mode phasing. An illustration of the laser output in frequency space is shown in Fig. 1; the pulse consists of several laser cavity modes that are equally spaced in frequency.

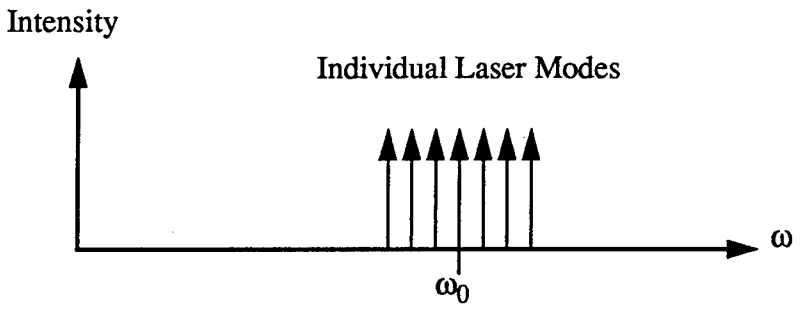

Figure 1. Frequency Representation of a Mode-Locked Laser Pulse.

The temporal form of this laser output, found by taking the Fourier transform of Eq. (1), is

$$\tilde{A}(t) = \left[\frac{1}{4\pi^2|a||b|} comb\left(\frac{t}{a}\right) \otimes sinc\left(\frac{t}{b}\right)\right] \cdot exp(-i\omega_0 t), \tag{3}$$

which is a time series of sinc pulses of light at base angular frequency ω_0.

Now consider the return obtained by illuminating an object with such a mode-locked pulse. It follows that each frequency is multiplied by a complex constant that is equivalent to the detected optical field that results when the object is illuminated with the particular laser frequency at unit amplitude. Using Eq. (1), we can write the return pulse as a superposition of the output frequencies with each multiplied by a complex constant corresponding to the return field

$$A_{ret}(r_d, \omega) = U(r_d, \omega) \{ [comb(a\omega) \cdot rect(b\omega)] \otimes \delta(\omega - \omega_0) \}, \tag{4}$$

where $U(r_d,\omega)$ is the optical field from the object for the particular detector location and source frequency given in Eq. (1). As shown by this equation and illustrated in Fig. 2, frequency analysis of the return pulse yields a sampled version of the objects complex reflectivity.

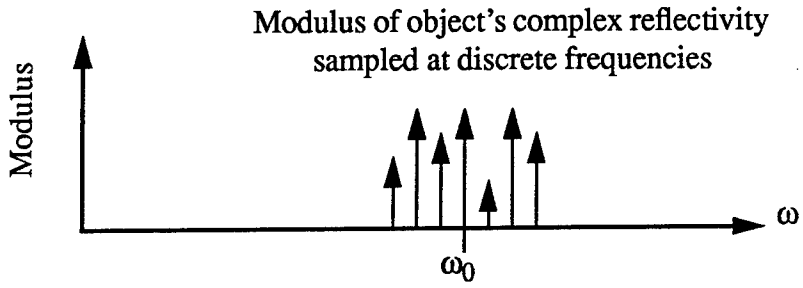

Figure 2. Frequency Representation of a Returned Mode-Locked Laser Pulse.

The detection scheme for PHI is to detect the return given in Eq. (4) using a heterodyne receiver. The resulting output is the optical field as a function of time. This temporal signal is found by taking the Fourier transform of Eq. (4) with respect to the time variable which gives

$$\tilde{A}_{ret}(r_d, t) = \tilde{U}(r_d, t)\left(\left[\frac{1}{4\pi^2|a||b|} comb\left(\frac{t}{a}\right) \otimes \sin c\left(\frac{t}{b}\right)\right] \cdot exp\,(-i\omega_0 t)\right) \quad . \tag{5}$$

As shown in Eq. (4), PHI provides a convenient means for sampling the object field at a series of equally spaced samples. Also, 2-D Fourier transformation of the received signal for each time-bin with respect to the variable r_d will yield an estimate of the 3-D object.

A block diagram for a PHI system is shown in Fig. 3. Essential elements include a pulsed laser source and a 2-D array of pupil-plane heterodyne receiver elements. 3-D image recovery is achieved by 2-D Fourier transformation of the received data in the dimensions of the receiver array for each time bin. Note that only the return from a single pulse is needed for image recovery.

Further insight into PHI can be gained by considering the temporal Fourier transform of the received field. This is equivalent to the received field when the object is illiminated by an impulse. From Eq. (1) we have

$$\tilde{U}(r_d, t) = \alpha \int \sigma(r)\, \delta\left(t - \frac{R}{c} + \left(\frac{r_s + r_d}{c}\right) \cdot r\right) d^3r \quad . \tag{6}$$

For the monostatic case with r_s and r_d pointing in the z direction, we have

$$\tilde{U}(r_d, t) = \alpha \int \sigma(x, y, z)\, \delta\left(t - \frac{R}{c} + 2\frac{z}{c}\right) dx dy dz \quad , \tag{7}$$

where we have switched to Cartesian coordinates. Further evaluation of this equation yields

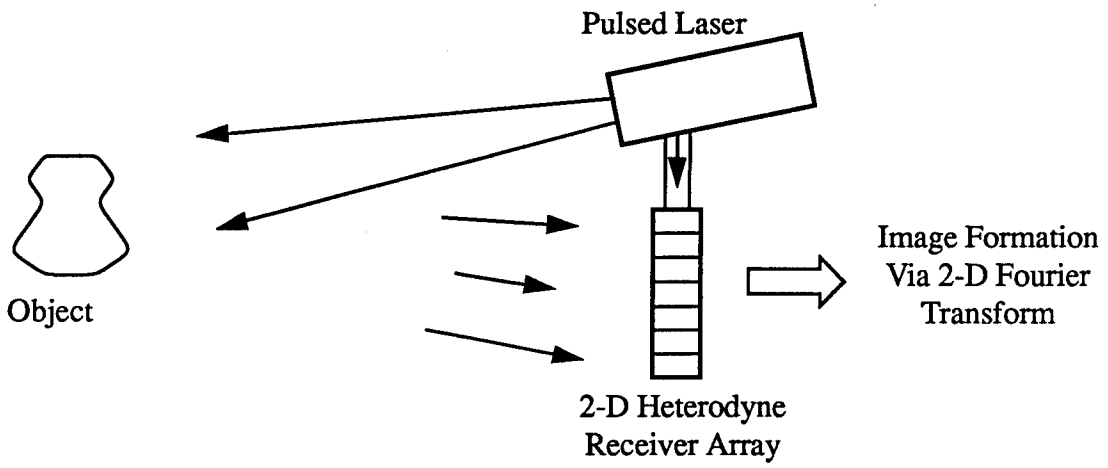

Figure 3. Block diagram for Pulsed Heterodyne-array Imaging (PHI).

$$\tilde{U}(r_d, t) = \alpha \int \sigma_p(z)\, \delta\left(t - \frac{R}{c} + 2\frac{z}{c}\right) dz \ , \tag{8}$$

where $\sigma_p(z)$ is the object's complex reflectivity projected onto the z-axis. Evaluation of this integral yields

$$\tilde{U}(r_d, t) = \alpha' \sigma_p\left(\frac{R}{2} - \frac{ct}{2}\right), \tag{9}$$

where α' is an innessential constant. Now consider the received field in the time domain. From Eqs. (5) and (9) we have in the case of monostatic operation along the z-axis

$$\tilde{A}_{ret}(r_d, t) = \alpha' \sigma_p\left(\frac{R}{2} - \frac{ct}{2}\right) \otimes \left[\frac{1}{4\pi^2 |a||b|} comb\left(\frac{t}{a}\right) \otimes \mathrm{sinc}\left(\frac{t}{b}\right)\right] \cdot exp\,(-i\omega_0 t) \ . \tag{10}$$

This result shows, in agreement with intuition, that the return consists of a time series of sinc pulses convolved with the projected cross-section of the object's complex reflectivity.

3.0 Summary

In summary, we have shown that PHI provides a way to generate coherent 3-D images of targets. It uses a pulsed laser with pulse-length equal to the desired range resolution. The use of a pulsed laser eliminates the need for performing a Fourier transform in the source frequency dimension as required with HLR. It is anticipated that PHI will be useful for 3-D imaging distant objects where pulsed illumination and high-speed detection are advantageous.

Acknowledgment

This research was supported by BMDO/IS&T through ONR.

4.0 References

1. J. C. Marron and K. S. Schroeder, "Holographic Laser Radar," Optics Letters, 18, 385-387 (1993).

2. J. W. Walker, "Range-Doppler Imaging of Rotating Objects," IEEE Trans. Aerosp. Electron. Syst. AES-16, 23-52 (1980).

3. N. H. Farhat, "Holography, Wavelength Diversity and Inverse Scattering," in Optics in Four Dimensions-1980, M. A. Machado and L. M. Narducci, eds. (American Institute of Physics, New York, 1981)

4. J. C. Marron and K. S. Schroeder, "Three-Dimensional Lensless Imaging Using Laser Frequency Diversity," Applied Optics, 31, 255-262 (1992).

5. J. C. Marron and K. S. Schroeder, "Holographic Laser Radar." In "Optics in 1993," B. D. Guenther ed., Optics and Photonics News, Vol. 4, No. 12, 17-18 (1993).

6. G. McAllister, et al., "Excimer UV Laser Radar for Image, Range and Doppler Measurements," in Laser Radar II, R. J. Becherer and R. C. Harney, eds., Proc. SPIE 783, 17-20 (1987).